

DESIGN, MODELING AND CONTROL OF A SATCOM ON-THE-MOVE
ANTENNA TERMINAL

A THESIS SUBMITTED TO
THE GRADUATE SCHOOL OF NATURAL AND APPLIED SCIENCES
OF
MIDDLE EAST TECHNICAL UNIVERSITY

BY

İLİM KARAÇAL

IN PARTIAL FULFILLMENT OF THE REQUIREMENTS
FOR
THE DEGREE OF MASTER OF SCIENCE
IN
MECHANICAL ENGINEERING

DECEMBER 2019

Approval of the thesis:

**DESIGN, MODELING AND CONTROL OF A SATCOM ON-THE-MOVE
ANTENNA TERMINAL**

submitted by **İLİM KARAÇAL** in partial fulfillment of the requirements for the degree of **Master of Science in Mechanical Engineering Department, Middle East Technical University** by,

Prof. Dr. Halil Kalıpçılar
Dean, Graduate School of **Natural and Applied Sciences**

Prof. Dr. M. A. Sahir Arıkan
Head of Department, **Mechanical Engineering**

Prof. Dr. Tuna Balkan
Supervisor, **Mechanical Engineering, METU**

Examining Committee Members:

Assist. Prof. Dr. A. Buğra Koku
Mechanical Engineering, METU

Prof. Dr. Tuna Balkan
Mechanical Engineering, METU

Prof. Dr. Y. Samim Ünlüsoy
Mechanical Engineering, METU

Assist. Prof. Dr. Ali Emre Turgut
Mechanical Engineering, METU

Assist. Prof. Dr. Melih Çakmakcı
Mechanical Engineering, Bilkent University

Date: 05.12.2019

I hereby declare that all information in this document has been obtained and presented in accordance with academic rules and ethical conduct. I also declare that, as required by these rules and conduct, I have fully cited and referenced all material and results that are not original to this work.

Name, Surname: İlim Karaçal

Signature :

ABSTRACT

DESIGN, MODELING AND CONTROL OF A SATCOM ON-THE-MOVE ANTENNA TERMINAL

Karaçal, İlim

M.S., Department of Mechanical Engineering

Supervisor: Prof. Dr. Tuna Balkan

DECEMBER 2019, 126 pages

The world becomes more connected with the help of increasing two-way communication day by day. High bandwidth data downlink demand independent of the range has increased excessively over the years. Also, communication need in all types of terrain conditions introduced a new communication method. Therefore, SATCOM on the move terminals become an important way of communication. These terminals provide to access communication in any environment and even at host vehicles. High disturbance rejection demand, compact design requirements and cost-effective solutions make the antenna system design challenges. Because to reach high data transmission rates antenna should be pointed with high precision. There exists tracking algorithms to increase the pointing performance of an antenna without the need for complex and costly hardware solutions. These dedicated tracking algorithms use the received signals from the target source as feedback to track the target all the time.

This thesis focuses on design, modeling and control of a SATCOM on the move antenna gimbal system for maritime application. ASEL SAN antenna gimbal terminal

is used. This system is used in ship platforms for data communication. In this study, firstly antenna system architecture, components, gimbal design criteria and principles of operations are defined. System identification tests are performed to obtain system behavior under different conditions. Then, the mathematical model of the gimbal is obtained and the gyro-stabilized control-loop is designed to perform required performance metrics. Open and closed-loop pointing strategies are explained, implemented and simulated. Two closed-loop pointing methods are studied and their performances are analyzed. These are conical scanning and step tracking methods. The results of the studies are showed that inertial stabilization is crucial in LOS pointing performance. However, stabilization is not enough alone to provide required pointing accuracy and tracking methods should be used. Communication is lost in simulations with only LOS stabilization. However, tracking methods are provided to continue communication with oscillation in performance but it is still good enough even for the harsh simulation scenarios. It is obtained that conical scanning is more reliable and robust than step tracking technique. It is shown that uninterrupted high-bandwidth communication performance is possible with tracking methods.

Keywords: SATCOM On-The-Move, Inertially Stabilized Platform, Antenna Control Systems, Gimbal Systems, Satellite Tracking and Communication

ÖZ

MOBİL RF UYDU HABERLEŞME ANTEN TERMİNALİNİN TASARIMI, MODELLENMESİ VE KONTROLÜ

Karaçal, İlim

Yüksek Lisans, Makina Mühendisliği Bölümü

Tez Yöneticisi: Prof. Dr. Tuna Balkan

Aralık 2019 , 126 sayfa

İki yönlü haberleşmenin gün geçtikçe artmasıyla dünya daha da bağlı hale geldi. Mesafeden bağımsız olarak yüksek bant genişliğinde data indirme talebi yıllar içerisinde aşırı artmıştır. Ayrıca, her türlü arazi koşullarında iletişim ihtiyacı yeni bir iletişim yöntemi getirdi. Bu nedenle mobil RF uydu haberleşme terminalleri önemli bir iletişim yolu haline geldi. Bu terminaller herhangi bir ortamda ve hatta bulunan araçlardan bile iletişime erişmeyi sağlıyor. Yüksek bozucu etki giderim talebi, kompakt tasarım gereklilikleri ve uygun maliyetli çözümler anten sistem tasarımını zorlaştırıyor. Çünkü yüksek veri iletim hızlarına ulaşmak için anten birimi yüksek hassasiyette yönlendirilebilmelidir. Bir antenin yönelim performansını arttırmak için karmaşık ve yüksek maliyetli donanım çözümlerine ihtiyaç duymayan takip algoritmaları bulunmaktadır. Bu özelleşmiş takip algoritmaları hedefi sürekli takip etmek için hedef kaynaktan alınan sinyali geri besleme olarak kullanır.

Bu tez çalışması denizcilik uygulamaları için mobil RF uydu haberleşme terminalinin tasarımı, inşası ve simülasyonuna odaklanmaktadır. ASELSAN anten gimbal termi-

nali kullanılmıştır. Bu sistem gemi platformlarında data iletişimi için kullanılır. Bu çalışmada öncelikle anten sisteminin mimarisi, bileşenleri, tasarım kriterleri ve çalışma prensipleri tanımlanmıştır. Sistem davranışını elde etmek için farklı koşullar altında sistem tanımlama testleri yapılmıştır. Gimbal sisteminin matematiksel modeli elde edilmiş ve gyro-stabilize kontrol döngüsü gerekli performans ölçümlerini gerçekleştirmek için tasarlanmıştır. Açık ve kapalı döngü yönelim stratejileri açıklanmış, uygulanmış ve simüle edilmiştir. İki kapalı döngü yönelim yöntemi çalışılmıştır ve performansları analiz edilmiştir. Bu yöntemler konik tarama ve adım takiptir. Çalışmaların sonucu ataletsel stabilizasyonun bakış hattı yönelim performansında kritik olduğunu göstermiştir. Bununla birlikte istenen yönelim hassasiyetini sağlamak için stabilizasyon tek başına yeterli değildir ve takip yöntemleri kullanılmalıdır. Simülasyonlarda sadece bakış hattı stabilizasyonu kullanıldığında haberleşme kesilmiştir. Bununla birlikte takip yöntemleri sayesinde haberleşmeye performans dalgalanmaları ile devam edilebilir ve bu performans zorlayıcı simülasyon senaryolarında bile yeterlidir. Konik taramanın adım takip yönteminden daha güvenilir ve daha gürbüz olduğuna ulaşılmıştır. Takip metodları ile yüksek bant genişliğinde ve kesintisiz iletişimin mümkün olduğu gösterilmiştir.

Anahtar Kelimeler: Mobil RF Uydu Haberleşmesi, Ataletsel Stabilize Platform, Anten Kontrol Sistemleri, Gimbal Sistemleri, Uydu Takip ve Haberleşme

To my lovely family
and
To my love Duygu

ACKNOWLEDGMENTS

First of all, I would like to thank my supervisor Prof. Dr. Tuna Balkan for his guidance, advice, encouragement and supports throughout the thesis work.

I would like to express my appreciation to my director Serdar Terzi and my manager Dr. Akif Türker Gürer for their support during this study.

I sincerely like to thank my superior Onur Albayrak for his invaluable support. I would like to express my appreciation to my colleague Ahmet Mavuş for his endless support, suggestions and friendship. I would also like to thank Ömer Çakmak for his support and suggestions about my study.

I would like to thank ASELSAN A.Ş. for supporting the study.

I would like to express my deepest gratitude to my family for their support and endless understanding during my life. I would also appreciate my love Duygu for her encouragement and support in my life all the time.

TABLE OF CONTENTS

ABSTRACT	v
ÖZ	vii
ACKNOWLEDGMENTS	x
TABLE OF CONTENTS	xi
LIST OF TABLES	xv
LIST OF FIGURES	xvii
LIST OF SYMBOLS AND ABBREVIATIONS	xxii
CHAPTERS	
1 INTRODUCTION	1
1.1 Motivation	1
1.2 Problem Definition	2
1.3 Proposed Methods and Models	3
1.4 Literature Review	4
1.4.1 Inertially Stabilized Platforms	5
1.4.2 Antenna Gimbal System	5
1.4.3 RF Signal Source Tracking	7
1.4.3.1 Conical Scanning	7
1.4.3.2 Step Tracking	11

1.5	The Outline of the Thesis	17
2	SYSTEM ARCHITECTURE	19
2.1	Introduction	19
2.2	Antenna and RF Signal	19
2.3	Mechanical Parts and Electronic Components	19
2.4	Radome	21
2.5	Satellite Communication	22
2.6	Pedestal Design Criteria	24
2.7	Controller Structure	24
2.7.1	Open-Loop Pointing	25
2.7.2	Closed-Loop Pointing	25
3	EQUATIONS OF MOTION	29
3.1	Kinematic Equations	29
3.2	Dynamic Equations	37
3.3	State Equations	38
3.4	Measurement Equations	38
4	SYSTEM IDENTIFICATION	41
4.1	Nonlinear Effect	42
4.1.1	Friction	42
4.1.1.1	Azimuth Axis	42
4.1.1.2	Elevation Axis	44
4.1.2	Cross Coupling	45
4.2	Identification Test	47

4.2.1	Azimuth Axis	48
4.2.2	Elevation Axis	51
4.3	Estimation of Transfer Function from Test Data	52
4.3.1	Azimuth Axis	53
4.3.2	Elevation Axis	53
5	MODAL REPRESENTATION OF TRANSFER FUNCTIONS	57
5.1	Transformation to Modal Space	57
5.1.1	Azimuth Axis	62
5.1.2	Elevation Axis	62
6	CONTROLLER DESIGN AND SIMULATION	63
6.1	Controller Structure	63
6.1.1	PI Controller	64
6.1.2	PI Controller Tuning Procedure	64
6.1.3	Filter Design	65
6.2	Tuning of Controllers	66
6.2.1	Azimuth Axis	66
6.2.2	Elevation Axis	67
6.3	LOS Stabilization Simulation	70
7	POINTING SCHEME	73
7.1	Antenna Gain Pattern	73
7.2	Open-Loop Pointing	76
7.3	Closed-Loop Pointing	79
7.3.1	Cost Function	79

7.3.2	Tracking Controller	83
7.3.3	Conical Scanning	83
7.3.3.1	Effects of Scanning Parameters to Performance	87
7.3.3.2	Conical Scanning, After One Period (CSAP)	90
7.3.3.3	Conical Scanning, Continuously (CSC)	95
7.3.3.4	Predicted Gradient Conical Scanning (PGCS)	99
7.3.3.5	Comparision of Conical Scanning Techniques	103
7.3.4	Step Tracking	104
7.3.4.1	Constant Step Size Tracking (CSST)	108
7.3.4.2	Variable Step Size Tracking (VSST)	112
7.3.4.3	Comparision of Step Tracking Techniques	118
8	SUMMARY, CONCLUSIONS AND FUTURE WORK	119
8.1	Summary and Conclusions	119
8.2	Future Work	121
	REFERENCES	123

LIST OF TABLES

TABLES

Table 4.1	Test Parameter Table for Azimuth Axis System Identification	50
Table 6.1	Azimuth Axis Controller	67
Table 6.2	Azimuth Axis Controller Performance Parameter	67
Table 6.3	Elevation Axis Controller	69
Table 6.4	Elevation Axis Controller Performance Parameter	70
Table 6.5	LOS Stabilization Disturbance Details	72
Table 7.1	Simulation Parameter Table for Different R	88
Table 7.2	Simulation Parameter Table for Different ω	88
Table 7.3	CSAP Method Controller Gains	90
Table 7.4	Simulation-1 Cases Table for Different Offsets	91
Table 7.5	CSAP Method Performance Parameter for Simulation-1	92
Table 7.6	Simulation-2 Cases Table for Gyro Drift	93
Table 7.7	CSAP Method Performance Parameter for Simulation-2	94
Table 7.8	Simulation-3 Cases Table for Target Drift	94
Table 7.9	CSAP Method Performance Parameter for Simulation-3	94
Table 7.10	CSC Method Controller Gains	96

Table 7.11 CSC Method Performance Parameter for Simulation-1	97
Table 7.12 CSC Method Performance Parameter for Simulation-2	98
Table 7.13 CSC Method Performance Parameter for Simulation-3	99
Table 7.14 PGCS Method Controller Gains	100
Table 7.15 PGCS Method Performance Parameter for Simulation-1	101
Table 7.16 PGCS Method Performance Parameter for Simulation-2	102
Table 7.17 PGCS Method Performance Parameter for Simulation-3	103
Table 7.18 Step Size Table	106
Table 7.19 Performance Parameters of Simulation for Different Step Sizes . . .	106
Table 7.20 CSST Method Controller Gains	108
Table 7.21 CSST Method Performance Parameter for Simulation-1	109
Table 7.22 CSST Method Performance Parameter for Simulation-2	110
Table 7.23 CSST Method Performance Parameter for Simulation-3	111
Table 7.24 Step Tracking Parameter Table for Different κ	112
Table 7.25 Step Tracking Parameter Table for Different γ	114
Table 7.26 VSST Method Controller Gains	114
Table 7.27 VSST Method Performance Parameter for Simulation-1	116
Table 7.28 VSST Method Performance Parameter for Simulation-2	116
Table 7.29 VSST Method Simulation-3, Case-1 and Case-2	118

LIST OF FIGURES

FIGURES

Figure 1.1	Mobile RF Satellite Communication System [3].	2
Figure 1.2	Boresight of Antenna Gimbal System [5].	3
Figure 1.3	Drift of a Geostationary Satellite [6].	4
Figure 1.4	Fleet F77 Antenna [9].	7
Figure 1.5	Calculation of Offset [12].	8
Figure 1.6	Calculation of Offset [5].	10
Figure 1.7	Comparison of Performances [5].	10
Figure 1.8	Results Obtained from Simulation [17].	12
Figure 1.9	Boresighting Methods [23].	14
Figure 1.10	Comparison of Boresighting Schemes [23].	15
Figure 1.11	Comparison Table of Tracking Systems [24].	16
Figure 2.1	Representation of a Radome with an Antenna Gimbal [26].	21
Figure 2.2	Satellite to Ground Terminal Communication Representation [27].	22
Figure 2.3	Block Diagram of Antenna Ground Terminal System	23
Figure 2.4	Block Diagram of Open-Loop General Control System	26
Figure 2.5	Block Diagram of Closed-Loop Gimbal Control System	27

Figure 3.1	Rerefence Frames	30
Figure 3.2	Antenna Gimbal	31
Figure 3.3	Base Body Frame [28].	31
Figure 3.4	Axis of Gyro [4].	34
Figure 3.5	Diagram of the Azimuth Axis	35
Figure 3.6	Diagram of the Elevation Axis	36
Figure 4.1	Relation of Friction Torque with Velocity	43
Figure 4.2	Diagram of Torque vs Position for Azimuth Axis, @0.5deg/sec	43
Figure 4.3	Diagram of Torque vs Position for Azimuth Axis, @1deg/sec	44
Figure 4.4	Diagram of Torque vs Position of Elevation Axis,, @0.5deg/sec	45
Figure 4.5	Diagram of Torque vs Position of Elevation Axis, @1deg/sec	46
Figure 4.6	Estimation of Azimuth Axis Inertia with Respect to Elevation Position	47
Figure 4.7	Diagram of System Identification Test Model	48
Figure 4.8	Frequency Response Test Representation	48
Figure 4.9	Bode Diagram of Azimuth Axis for Different Elevation Position	49
Figure 4.10	Bode Diagram of Elevation Axis	51
Figure 4.11	Transfer Function Estimate of Azimuth Axis	54
Figure 4.12	Transfer Function Estimate of Elevation Axis	56
Figure 5.1	Representation of Pyhsical Domain [32].	58
Figure 5.2	Representation of Modal Domain [32].	59
Figure 5.3	Representation of Structural Transfer Function [29].	61

Figure 6.1	Azimuth Axis Open-Loop Bode Diagram	68
Figure 6.2	Azimuth Axis Closed-Loop Bode Diagram	68
Figure 6.3	Azimuth Axis Step Response	69
Figure 6.4	Elevation Axis Open-Loop Bode Diagram	70
Figure 6.5	Elevation Axis Closed-Loop Bode Diagram	71
Figure 6.6	Elevation Axis Step Response	71
Figure 6.7	LOS Simulation Case-1, Yaw Angular Velocity	72
Figure 7.1	Operation Sequence of Antenna System	74
Figure 7.2	Antenna Gain Pattern for 0.5m Aperture Working at 14.5 GHz [1].	75
Figure 7.3	HPBW with Respect to Service Frequency and Antenna Size [1].	75
Figure 7.4	Antenna Gain Pattern [10].	76
Figure 7.5	Coordinates Frame Representation [37].	78
Figure 7.6	Satellite Look Angle Representation.	79
Figure 7.7	AGS Cascaded Tracker-Loop and Rate-Loop Representation . .	80
Figure 7.8	Power Change with Respect to Elevation Axis Position	81
Figure 7.9	Cost Function with Respect to Elevation Axis Position and 3dB Beamwidth	82
Figure 7.10	Beacon Signal Noise	83
Figure 7.11	Closed-Loop System Detailed Block Diagram	84
Figure 7.12	Conical Scan Pattern [38].	86
Figure 7.13	Amplitude Variation of the Received Signal [39].	86
Figure 7.14	LOS Representation with Azimuth and Elevation Axes [11]. . . .	87

Figure 7.15	Simulation for Different R with $\omega = \frac{\pi}{4}$ (rad/s)	89
Figure 7.16	Simulation for Different ω with $R = 0.4$ (deg)	89
Figure 7.17	CSAP Method Simulation-1, Case-1 and Case-2	91
Figure 7.18	CSAP Method Simulation-1, Case-3 and Case-4	92
Figure 7.19	CSAP Method Simulation-2, Case-1 and Case-2	93
Figure 7.20	CSAP Method Simulation-3, Case-1 and Case-2	95
Figure 7.21	CSC Method Simulation-1, Case-1 and Case-2	96
Figure 7.22	CSC Method Simulation-1, Case-3 and Case-4	97
Figure 7.23	CSC Method Simulation-2, Case-1 and Case-2	98
Figure 7.24	CSC Method Simulation-3, Case-1 and Case-2	99
Figure 7.25	PGCS Method Simulation-1, Case-1 and Case-2	100
Figure 7.26	PGCS Method Simulation-1, Case-3 and Case-4	101
Figure 7.27	PGCS Method Simulation-2, Case-1 and Case-2	102
Figure 7.28	PGCS Method Simulation-3, Case-1 and Case-2	103
Figure 7.29	Operation Sequence of Step Tracking	105
Figure 7.30	Simulation for Different Step Sizes, Case-1,Case-2,Case-3,Case- 4	107
Figure 7.31	Simulation for Different Step Sizes, Case-5 and Case-6	107
Figure 7.32	CSST Method Simulation-1, Case-1 and Case-2	108
Figure 7.33	CSST Method Simulation-1, Case-3 and Case-4	109
Figure 7.34	CSST Method Simulation-2, Case-1 and Case-2	110
Figure 7.35	CSST Method Simulation-3, Case-1 and Case-2	111

Figure 7.36	Power Change for Same γ and Different κ	113
Figure 7.37	Power Change for Same κ and Different γ	113
Figure 7.38	VSST Method Simulation-1, Case-1 and Case-2	115
Figure 7.39	VSST Method Simulation-1, Case-3 and Case-4	115
Figure 7.40	VSST Method Simulation-2, Case-1 and Case-2	117
Figure 7.41	VSST Method Simulation-3, Case-1 and Case-2	117

LIST OF SYMBOLS AND ABBREVIATIONS

SYMBOLS

a	Semi-major earth axis (ellipsoid equatorial radius)
b	Semi-major earth axis (ellipsoid polar radius)
T	Period
e^2	Square of the ellipsoid eccentricity in closed form
f	Flattening parameter
N	Principle radius of curvature in the prime vertical
$\vec{\omega}_V^{(b)}$	Vehicle angular velocity in terms of b frames
$\vec{\omega}_{Az}^{(a)}$	Azimuth gimbal angular velocity in terms of a frame
$\vec{\omega}_{El}^{(e)}$	Elevation gimbal angular velocity in terms of e frame
P	Vehicle inertial roll velocity about x_b -axis
Q	Vehicle inertial pitch velocity about y_b - axis
R	Vehicle inertial yaw velocity about x_b - axis
ψ	Azimuth axis relative angle
$\dot{\psi}$	Azimuth axis relative rate angle
θ	Elevation axis relative angle
$\dot{\theta}$	Elevation axis relative rate angle
J_{Az}	Azimuth gimbal inertia
J_{El}	Elevation gimbal inertia
p_r	Pole location of the r^{th} mode
ω_r	Modal frequency of the r^{th} mode
σ_r	Half power point damping of the r^{th} mode
R_r	Residues
M	Damping matrice

K	Stiffness matrice
f	Applied external force vector
\ddot{x}, \dot{x}, x	Acceleration, elocity and displacement vectors
R_I	Lower residuals
R_F	Upper residuals
w_N	Notch filter frequency
ζ_1, ζ_2	Notch filter damping ratios
ϕ	Geodetic latitude
λ	Geodetic longitude
h	Geodetic height
X, Y, Z	Earth Centered Earth Fixed Cartesian Coordinates
ε_i	LOS RMS error
Δaz	Azimuth axis error from the target satellite
Δel	Elevation axis error from the target satellite
ω	Frequency of the conical scanning motion
R	Radius of the conical scanning motion
p	RSS, power
G	Parametric gain to adjust the calculation
\bar{x}	Calculated Az-axis compensation
\bar{y}	Calculated El-axis compensation
$x_{PosPerturbation}$	Az-axis position perturbation
$y_{PosPerturbation}$	El-axis position perturbation
$x_{VelPerturbation}$	Az-axis velocity perturbation
$y_{VelPerturbation}$	El-axis velocity perturbation
k_p, k_i	Controller proportional and integral gain
K_p	Tracking controller proportional gain

ABBREVIATIONS

AGS	Antenna Gimbal System
DOF	Degree of Freedom
ECEF	Earth Centered Earth Fixed
FFT	Fast Fourier Transform
HPBW	Half-Power Beamwidth
IMU	Inertial Measurement unit
ISPs	Inertially Stabilized Platforms
LOS	Line of Sight
NED	North East Down
SATCOM	Mobile RF Satellite Communication
RSS	Received Signal Strength
SNR	Signal to Noise Ratio
RF	Radio Frequency
SNR	Signal to Noise Ratio
TS	Target Satellite

CHAPTER 1

INTRODUCTION

1.1 Motivation

Traditional radios have been used for communication over the years. On the other hand, their importance is lessened within years because they are only capable of limited data rates and connection with line-of-sight (LOS) range. Furthermore, the change in market demand plays a critical role in the use of radios. Communication has become the most important tool in civil and military areas within years. The world becomes more connected and demand for broadband data rates has increased excessively day by day. Also, the market needs more data than voice services such as real-time high-quality video streaming and image transferring. People want to reach the internet, watch movies, video talk, send and receive files while they are moving on a train, bus and even plane. In the military, there exists also a similar situation. It is very crucial to communicate with each troop on the battlefield and even also between different forces such as from land forces to naval or aviation. These requirements introduced new communication ways. Mobile RF Satellite Communication (SATCOM) is a miracle solution to these problems. It enables high bandwidth and capacity independent of range and mobility with lower operating costs [1]. The more connected the world becomes the more important SATCOM terminals are. Satellite communication is basically explained as a man-made satellite works like a relay station to communicate with an earth radio source [2] which can be seen in Figure 1.1. SATCOM terminals have high-gain directional reflectors to perform high-bandwidth data rates. Therefore, LOS of the terminal must be directed with high precision. The communication performance of a SATCOM on-the-move terminal depends on the pointing precision.

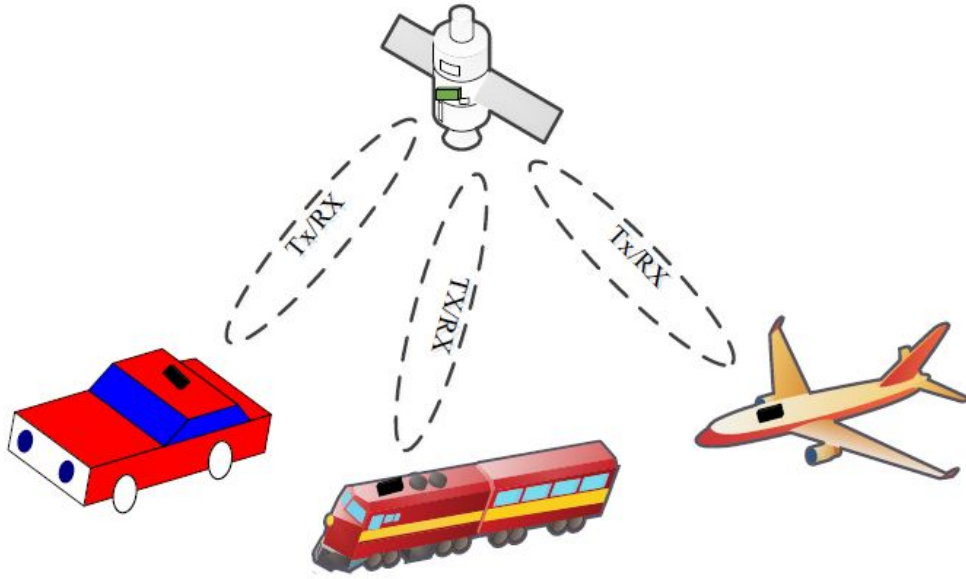


Figure 1.1: Mobile RF Satellite Communication System [3].

1.2 Problem Definition

Boresight (LOS) which is depicted in Figure 1.2 of an antenna should look directly to the satellite to perform communication. In addition to that, the antenna gimbal system (AGS) pointing accuracy should be very high and should be pointed over an extended period to a far target. If the AGS can point to the exact location of the target for a long time, the system data transmission rate would be as high as possible. This leads us to the point that the performance of a high-gain directional antenna is directly proportional to the pointing accuracy. The AGS can be inertially stabilized and can be locked to the target but this lasts only for short periods. Inertially stabilized gimbals have been used to track targets and attenuate disturbance over the years [4]. On the other hand, LOS stabilization can not provide enough performance for communication platforms for an extended period. Gyro sensors have the drift error issue due to several reasons. This drift error can cause mispointing of the LOS within time. Also, after the AGS is pointed to the maximum likelihood of the target there can be small boresight errors. The main reason for this error can be gyro and encoder sensor accuracy, random error caused by noise or temperature gradient and

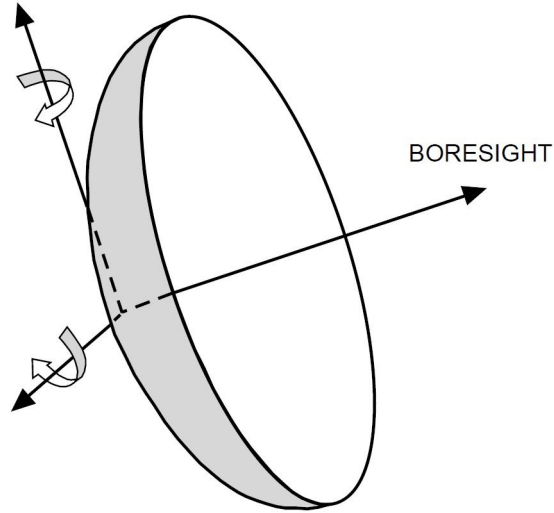


Figure 1.2: Boresight of Antenna Gimbal System [5].

mechanical misalignment or manufacturing imperfections. Therefore, there exists even small errors in the pointing of the LOS. In addition to this, the target position is not exact. Although geosynchronous satellites are immobile relative to the earth, their position can drift due to gravities of the moon and the sun. This is called an elongated "figure-8" pattern in the space which is given in Figure 1.3. Also, solar radiation pressure can cause this effect even for a geostationary satellite. As a result, communication performance can not be good enough and robust over long periods with only utilizing LOS stabilization.

1.3 Proposed Methods and Models

In order to increase the AGS transmission performance, there should be a closed-loop tracking control. There exists different tracking methods. Some of them is done by hardware means some of them is done by software. Hardware means results in more complex and more costly systems. Therefore, the development of a good tracking algorithm can solve this issue. The working principle of these algorithms relies on the maximization of the received signal strength (RSS). These algorithms provide active control of the antenna boresight by measuring the RSS and trying to compensate for small-angle errors. There are mainly two tracking techniques. In these methods, the

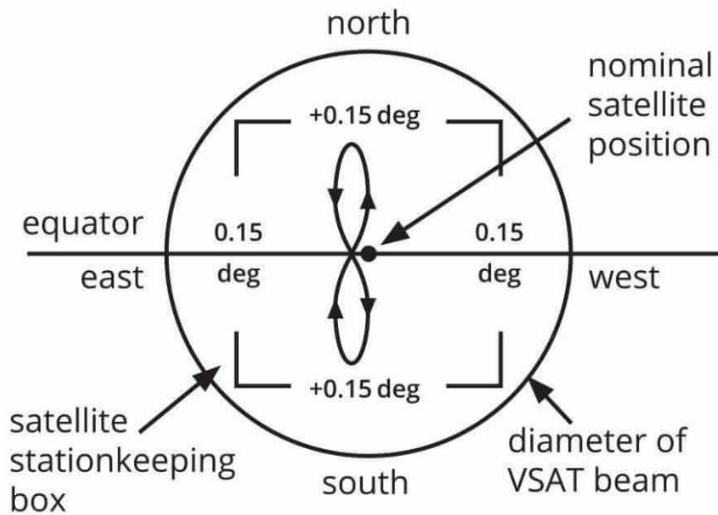


Figure 1.3: Drift of a Geostationary Satellite [6].

LOS is moved by different patterns around the target most likelihood position. During this motion, the RSS can change and this can be used to estimate the target location. Thus the antenna tracking system is a key component for the development of a SAT-COM terminal system. As a result, communication performance can be increased by tracking algorithms and robust antenna systems can be designed. In this study, we aimed to model, simulate and control of a SATCOM on-the-move antenna system with different tracking algorithms to achieve the tracking accuracy requirements by using ASELSAN antenna.

1.4 Literature Review

In this part of the thesis, the inertially stabilized platforms are reviewed as first, then antenna gimbal systems and applications are explained. Finally, target tracking algorithms that are specified in the field of RF signal source tracking are evaluated.

1.4.1 Inertially Stabilized Platforms

Inertially stabilized platforms (ISPs) mainly consist of electronic and mechanic parts. Electronic parts are comprised of electric motors and drivers, electronic components and sensors. The mechanic parts are bearings, connection links and mechanical components. Assembly of these items which have rotational degrees of freedom is called gimbal or pedestal. Degrees of freedom of the system can change depending on the host vehicle or configuration. ISPs generally are used to control payload's inertial orientation in terms of inertial space or another platform. ISPs are used over a long time for different applications such as astronomical telescopes, target tracking, weapon and communication systems [4].

One of the most important studies about ISPs was done by Hilkert in 2008 [4]. In this work, he explained the technology behind the system, working principles and application fields of ISPs. In addition to that, implementation details, performance characteristics and examples from the different areas were emphasized. He also analyzed how performance characteristics were affected by the system components.

In another study, Masten studied operating principles, applications and architecture of ISPs for optical imaging systems in a detailed manner in 2008 [7]. Design methodology of ISPs and guidelines of implementation details were explained. Furthermore, different types of stabilization techniques were studied with examples.

1.4.2 Antenna Gimbal System

Antenna gimbal systems are one of the applications of ISPs in which antenna reflector is used as a payload. Depending on RF characteristics, host vehicle and mechanical dimensional limitations, there are different examples of these systems.

Gimbal system in terms of kinematics was studied by Ekstrand in 2001 [8]. Two-axes gimbal system which had yaw-pitch gimbal configuration was analyzed, reference frames and notations of gimbals were defined. Equations of motion for this system were derived with details. Also, the reason for the disturbances and how to eliminate them were discussed.

In 2005, SpaceCom A/S and a team from Aalborg University made a co-operation to possible improvement of maritime used Fleet F77 Antenna that is shown in Figure 1.4 [9]. According to this work, the team tried to find improvements in antenna satellite tracking performance for new antenna projects of the firm. Their main aim was to give suggestions and studies about new antenna design and construction. Firstly, they analyzed the controller structure, actuators and placement and properties of the sensors. They were obtained analytical models of the sensors, motors and antenna gimbal by using system identification tools. Moreover, they modeled and verified these models. Accordingly, to increase sensor performances they suggested new sensors, designed a Kalman filter to increase sensor performances and changed the sensor placement. All of this work was done by using MATLAB Simulink. As a result of this study, the system performance was improved according to simulations successfully.

Control systems for mobile SATCOM antennas were studied by Debruin in 2008 [1]. In this study, the importance of these systems and application areas on the market were explained. Also, he studied the components of the SATCOM system and the working principle of these components. Mainly, he emphasized on the controller structure of the terminal and effect of the system units on this structure.

There is another work on a similar topic which was done by Marsh in 2008 [10]. In this study, the two-axis antenna system which was used in Boeing 707 aircraft was analyzed. System architecture and development steps were defined to be used in airborne applications. The gimbal system was constructed using kinematic and dynamic equations. The open-loop controller which was used in directing to the satellite for a nominal two-axis gimbal system was developed using optimal control techniques. Problems and issues related to open-loop pointing schemes were also explained. In addition to that, a closed-loop tracking controller which was using RF signal as feedback was implemented to increase the performance of open-loop pointing. Different tracking algorithms were compared to see their effect. The performance of the system under disturbance and different environmental conditions were also simulated. Also, a hybrid open and closed-loop feedback controlling technique was developed.

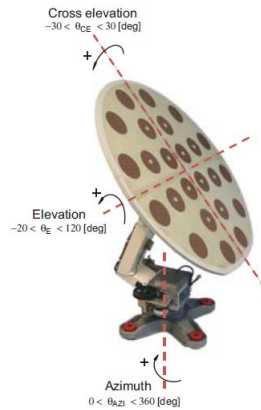


Figure 1.4: Fleet F77 Antenna [9].

1.4.3 RF Signal Source Tracking

In literature, there are different tracking algorithms and methods which maximize the quality of RF signal strength. Conical scanning and step tracking methods are the most popular ones.

1.4.3.1 Conical Scanning

In the conical scanning method, the antenna is rotated in a circular pattern with an off-set angle about the antenna's boresight axis. RSS is averaged during scanning period and then algorithm decides depending upon the RSS to correct boresight. When the radio source or spacecraft is on boresight, the RSS will be constant over the scanning cycle. If the antenna is off-boresight, there will be sinusoidal variation in the RSS. As a result, the offset movement will be calculated to correct boresight. No RF hardware change is required to the application of this algorithm.

The oldest and most important work about conical scan was done by NASA/JPL as a technical report in 1976 [11]. In this report, theoretical and experimental works about the feasibility of the conical scan tracking of the 64 m diameter parabolic antenna were documented. It was analyzed that the perturbation of an antenna, the effects of scanning frequency and radius on the antenna performance in a detailed manner.

$$E_C = G \sum_{SCAN} V(k) \sin(\omega k \Delta + Z)$$

$$X_C = G \sum_{SCAN} V(k) \cos(\omega k \Delta + Z)$$

where $V(k)$ is the k th edited signal sample,
 G = gain
 Z = phase shift

Figure 1.5: Calculation of Offset [12].

The position perturbation convolved with the RSS over a full cycle to obtain position offset for each axis. On the other hand, the algorithm was implemented for a fixed ground station.

Another similar application of the conical scan technique was done by JOhlnson and Abichandani in 1982 [12]. In this work, some improvements were done on the implementation of the algorithm. These were received signal cleanup and system protection in case of anomalies that can affect RSS. There was also a change in antenna boresight error compensation calculation. Instead of integrating RSS with position perturbation over a scan cycle, offset was calculated using the following relation as in Figure 1.5. Usage of the fast Fourier transform (FFT) was provided insight into the existence of noise in the input signal. However, it was realized that the FFT calculation took more effort than other methods.

In 1994, Kalman filter and its implementation details were proposed for the estimation of source position in detail by Eldred [13]. In this study, this technique was also compared with FFT based algorithm and the selection of conscan radius was reviewed adaptively. As a result of this study, the calculation of the source position was examined accurately which was a nearly continues update of antenna boresight error and also a more reliable calculation of offset data even with missing data were performed.

W. Gawronski and E. M. Craparo were reported that the analysis and comparison of three different scanning techniques which were conical scan, Lissajous scan and rosette scan and these techniques were used for estimation of spacecraft position [5]. Besides that, they mentioned how to evaluate and solve the estimation errors caused by a random change of antenna position and power variation. Moreover, the optimum conical scan radius and the choosing criteria of frequency were examined and the conical scan radius was chosen as an angular distance when the power of the source signal was dropped by 0.1 dB. Also, conical scan frequency should be chosen as twice as the antenna bandwidth. The calculation of antenna's boresight correction was done by comparing RSS with the theoretical signal level and according to this study it was found that the spacecraft's position could be estimated by the drop of the signal level. In other studies, boresight error compensation was generally calculated after one complete scanning cycle. However, in this study, they defined and used a new way of calculation which named as sliding window scanning technique. In this new technique, they changed the update period of the spacecraft position estimation. Instead of updating the position after every scanning period T , the update was done after ΔT period. The calculation of an offset can be seen in Figure 1.6 with details. It was realized that this new method overcame the slow update rate and the decrease in performance caused by a lag in tracking. The improvement in performance resulted by using this method explained in the following Figure 1.7.

Brooker reported the implementation and analysis of the conical scanning method by using three different types of antenna in 2003 [14]. They performed these analyses according to how to make circular movements, how to generate a reference signal and how to demodulate angle-error. As a result of this study, it was found that the conical scan technique robust and simple and also its adaptation to millimeter-wave antenna types without using extra hardware was easy.

Conical scanning technique was analyzed and simulated by Karol in 2012 [15]. The work started with traditional conical scanning and continued with two new improved ones. One of them was predicted gradient conical scanning. The other one was measured gradient conical scanning. In the traditional one, position perturbation was integrated with the RSS over a scanning cycle. However, in the predicted gradient conical

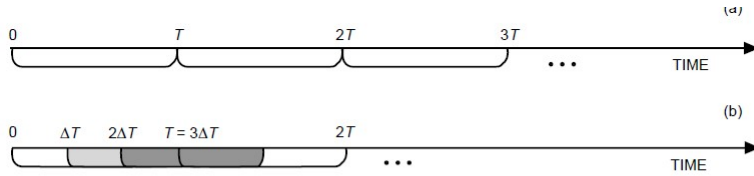


Fig. 13. Scans with the (a) non-sliding and (b) sliding-window techniques, for $\Delta T = (1/3)T$.

Table 4. Data collection time for the sliding-window scan.

Data collection time	Time span of the circle
T	$[0, T]$
$T + \Delta T$	$[\Delta T, T + \Delta T]$
$T + 2\Delta T$	$[2\Delta T, T + 2\Delta T]$
$T + i\Delta T$	$[i\Delta T, T + i\Delta T]$

Figure 1.6: Calculation of Offset [5].

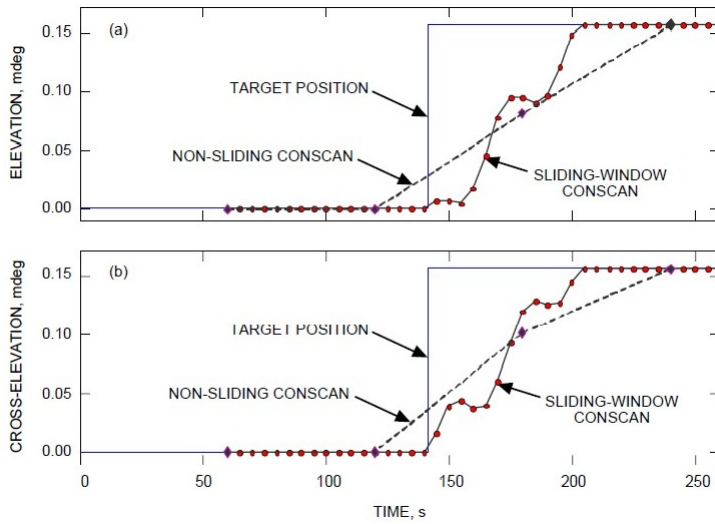


Figure 1.7: Comparison of Performances [5].

scanning instead of using position perturbation, gradient of position and gradient of the RSS was used in the integral calculation. This new method was provided the following advantages. The antenna was moved to the target position more consistently straight. Also, the system became more stable and the accumulation of error reduced. The second important advantage was that tracking capability was less dependent on the perturbation amplitude and this enables more robust under noise. Although, there exist advantages of this technique but taking derivative of the RSS resulted in more noise and less reliable RSS. The second new method was measured gradient conical scanning. In this one, position perturbation was read directly from gyro and gradient of the RSS were used in the integral calculation. Gyro reading provides less noise in perturbation signal and more reliable boresight error calculation. Also, the antenna was moved to the target position more consistently straight as in the same case before. However, RSS was still less reliable.

In another work, Kalman filter and its implementation details were proposed for the estimation of source position in a detailed manner by Souza et al. in 2013 [16]. Kalman filter was implemented in a different way that was proposed by Eldred, D. B. (1994). An improved conscan algorithm based on a Kalman filter. There were three main differences between them. The first one was that the measurement function was not linearized by the Taylor series expansion. It was used with mathematical manipulation. The second was that carrier power was related to one the state variables. Finally, the first-order time derivative of the state vector was also added. As a result, conical scan performance was improved and computational effort was less. In addition to that, it would replace the monopulse scan technique which was more accurate but needs extra hardware implementation.

1.4.3.2 Step Tracking

Step tracking is another signal maximization algorithm through iteration. The antenna rotates step-like with a small angle in each axis. The RSS is tried to be maximized during this movement and point to the satellite. This method provides no hardware change in the RF system and the application of the algorithm is simple. Therefore, it results in a cost-effective solution.

Algorithm	σ_{hp} at 50 dB			SNR at 0-1 dB Standard deviation			Minimum SNR for reliable operation			Minimum iterations in one axis		
	$\psi_{s1} \approx \psi_{hp}/23$	$\psi_{s2} \approx \psi_{hp}/11.5$	$\psi_{s3} \approx \psi_{hp}/5.7$	ψ_{s1}	ψ_{s2}	ψ_{s3}	ψ_{s1}	ψ_{s2}	ψ_{s3}	ψ_{s1}	ψ_{s2}	ψ_{s3}
Step-track	$\psi_{hp}/16$	$\psi_{hp}/10$	$\psi_{hp}/5.3$	≥ 40	≥ 48	not possible	~ 40	~ 35	~ 25	12	6	3
Gradient	$\psi_{hp}/16$	$\psi_{hp}/32$	$\psi_{hp}/63$	≥ 46.5	≥ 40.5	≥ 34.5	~ 40	~ 35	~ 25	2	2	2
Curve-fitting	Fails	Fails	$\psi_{hp}/4.9$	—	—	≥ 60	—	—	~ 50	4	4	4

Figure 1.8: Results Obtained from Simulation [17].

Three different algorithms were analyzed and compared by Richaria in 1986 [17]. The first one was Hill-climbing. The antenna was moved to the maximum signal point by changing movement direction depending on signal strength. The second one was curve fitting algorithm. Using the maximum signal strength point and three points in the neighborhood of the maximum the parabola of signal strength could be specified. The third one was gradient algorithm. This method used the fact that there was a linear relationship between the maximum of a parabola and gradient at a point on that parabola. Therefore, max RSS's position would be obtained by taking the gradient of RSS at any point. The followings were obtained as a result of this work, Figure 1.8. The performance of the classic step tracking method was directly related to step sizes and signal to noise ratio (SNR). Finer step sizes and higher SNR resulted in better performance. However, by making step size smaller increased iteration number. the curve fitting method was extremely sensitive to the noise and the sample point number was very critical. Therefore, it was not appropriate for robust satellite tracking. On the other hand, the gradient algorithm performed better with larger step sizes and for higher SNR accuracy was almost zero. In addition to that, the optimum step size should have been chosen. Finally, the best performance could be obtained with the gradient algorithm.

A new method which was “2D Model-Based Step Track” was presented based on the gradient algorithm by Laine in 2000 [18]. Also, this new one was compared with the hill-climbing and gradient methods. In this method, the satellite direction estimate was obtained using the paraboloid beam model of the signal. After getting enough 2D displacement vs the RSS pattern samples estimation of the satellite could be done. As a result, tracking performance was improved over Hill-climbing and gradient.

In a different study, simulations of step tracking was performed using MATLAB toolboxes by Pirhadi et al. in 2005 [19]. MATLAB models of the simulation were presented and explained. Hill-climbing and gradient methods were used. The performance of these two techniques was compared.

A new method was introduced by Han et al. in 2010 to overcome the main problems of step tracking which were slow tracking speed and low accuracy [20]. In this study, a solution to this problem was proposed. This was a new step tracking algorithm based on the steepest descent method. It was used for calculation of variable step size and direction of movement. As a result, accuracy was improved and the number of iteration was reduced.

Finite difference stochastic approximation was used for gradient calculation by Jia et al. in 2011 [21]. This technique was improved the traditional gradient calculation because there was need a lot of experimental data to get a parabolic signal model for the traditional one. However, this was not an applicable case for an antenna on the move. Also, the received signal had noise due to environmental conditions. Therefore, this new algorithm enabled more precision, faster tracking performance and reduced mechanical wear.

It was proposed that using fixed step size result in low accuracy or slower tracking speed and to find an optimum value was not straightforward by Chen and Wang in 2013 [22]. Therefore, a variable step size technique was stated instead of a fixed one. The error between maximum signal level and the current signal was used for calculation of variable step size. Smaller error meant less step size, higher error meant bigger step size. The proposed technique was simulated and compared with traditional step tracking. As a result, system performance, tracking speed and accuracy was improved.

Four different scanning techniques were compared by Abichandani and Ohison in 1981 [23]. These are stepscan, triscan, conscan, single-axis scan, Figure 1.9. Step-scan was the traditional step tracking method. Triscan had the same manner as step-scan. On the other hand, the main difference was tree points were used in signal

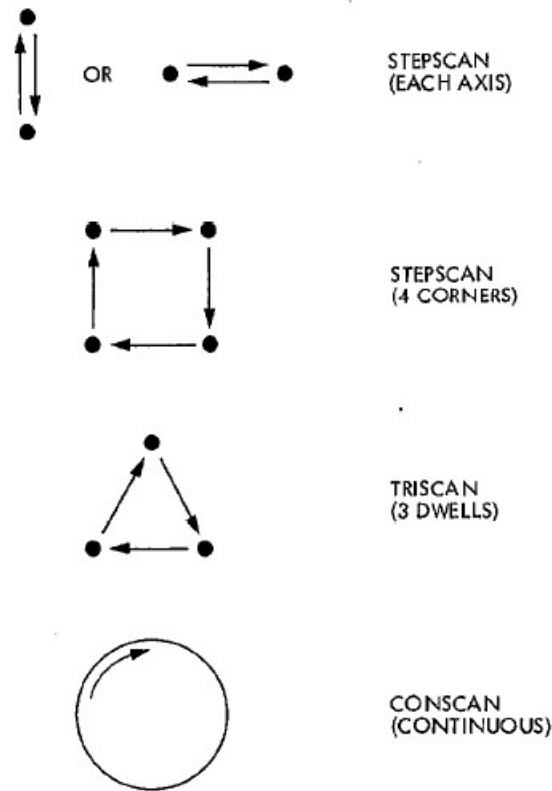


Figure 1.9: Boresighting Methods [23].

strength measurement. Conscan was a traditional conical scanning method. The last one was a single axis scan. The antenna was moved in one direction once along one axis at a constant amount and also the measurement of the signal was done during this motion. After that, measured signal power was fitted to a beam shape and using this parabola signal peak angle can be estimated. Finally, these steps were done for the other axis and the peak gain could be estimated. The following figure shows these techniques graphically. Simulation of these methods were done. The performance of each technique was summarized in Figure 1.10.

Three main different techniques were compared from hardware differences to application details by Hawkins et al. in 1988 [24]. These were manual/program tracking, monopulse or simultaneous sensing, sequential amplitude sensing and electronic beam squinting. Manual/program tracking was an open-loop tracking method. In manual tracking, an operator moved the antenna boresight to maximize the RSS.

	CONSCAN	STEPSCAN	TRISCAN	SINGLE-AXIS SCAN
High importance				
a. Overall accuracy	5	4	4	4
b. Insensitivity to signal anomalies	5	4	4	2
Moderate importance				
c. Efficiency	5	4	4	4
d. Insensitivity to beam shape	5	4	4	4
Low importance				
e. Computation for scan	Much	Little	Little	Medium
f. Computation for correction	Much	Little	Little	Medium

^aScale of 0 to 5, with 5 best.

Figure 1.10: Comparison of Boresighting Schemes [23].

In program tracking, the antenna was moved by time in a prepaid path of satellite position. These two techniques could not compensate environmental effect even these antennas were stationary types. Therefore, the performance of these two was limited and not feasible for moving platform applications. In monopulse or simultaneous sensing technique, antenna had a different hardware configuration. There was more than one signal receiving channel. By the help of this configuration, RSS could be compared in each axis continuously. Therefore antenna could act quickly to compensate RSS drop and accuracy was very high. On the other hand, this antenna hardware configuration was very complex, expensive and mechanically large. In addition to this, sequential amplitude sensing had not a good performance as monopulse. However, sequential amplitude sensing provided optimum performance with basic hardware equipment and less costly solution. This method was composed of step-tracking or hill-climbing and conical scanning. These were traditional ones. After giving the application details of the algorithms, they were compared in terms of performance and application. These could be found from the following Figure 1.11.

Tracking category	Subcategory	Remarks	Performance	Usage
Manual		non-autotracking; simple; requires operator	tracking accuracy dependent on operator — generally low	many stations can revert to manual tracking if other tracking methods fail
Programme steering		non-autotracking; simplistic with modern technology; requires operator intervention; accuracy reliant on orbit prediction	tracking accuracies approaching 0.01° possible	often employed as back-up in case primary tracking system fails
Monopulse	Simultaneous lobing [1] Multimode — TM_{01} [2] — TM_{01}/TE_{21} [3] — orthogonal — TE_{21} [4]	autotracking tracking information obtained in a single time frame; 2, 4 or 8 channel coherent receiver required; expensive	tracking accuracy very good, typically 0.005° ; operational SNR ~ 15 dB; fast dynamic response	widespread in many of the larger earth stations; also shipborne terminals, sat-to-sat comms
Conical scan	Rotation of antenna [1]; rotation of offset feed [2]; rotation of sub-reflector [3]; TM_{01} mode [4]; TM_{01}/TE_{21} mode [5]; Conopulse [6]	autotracking; sequential amplitude sensing system; sensitive to AM interference; mechanically complex; uses single channel receiver; methods 1–3 result in modulation of uplink transmission	tracking accuracy typical 0.01° ; operational SNR ~ 30 dB; medium dynamic response	widespread up until mid 70s; monopulse and step-track then preferred
Step-track	step antenna [1]; nodding sub-reflector [2]	autotracking; sequential amplitude sensing system; sensitive to AM interference; simple low cost system; single channel receiver; method [1] results in high wear of mechanical drives	tracking accuracies of 0.01° have been obtained, typically $< 0.1^\circ$; operational SNR ~ 30 – 45 dB; slow dynamic response	widespread where lower accuracy acceptable and cost important; many of the smaller earth stations, shipborne terminals
Electronic beam steering	dipole feed [1]; TM_{01}/TE_{21} mode; conversion techniques [2]	autotracking; pseudoamplitude sensing system; much reduced sensitivity to AM interference; uses single channel receiver; relatively simple	tracking accuracy approaching monopulse, 0.005° ; operational SNR 15 – 30 dB; fast dynamic response	use limited to mainly experimental tracking systems; shows good overall tracking performance; well suited to sat-to-sat comms; should be widely used in future

Figure 1.11: Comparison Table of Tracking Systems [24].

1.5 The Outline of the Thesis

In this chapter, the motivation of this study, the definition of the problem and proposed methods to solve this problem is introduced. In the literature review, inertially stabilized platforms and antenna gimbal systems are introduced with the application examples. In addition to that, RF signal and target tracking algorithm theories and implementation details are given.

In Chapter 2, the architecture of an antenna gimbal system is given. Details and functionality of each component are presented. Furthermore, controller structures and the aim of operations are presented.

In Chapter 3, the dynamics of a two-axis gimbal platform is presented. Kinematic coupling disturbance details and gimbal-lock is introduced.

In Chapter 4, nonlinear effects are presented. Different types of mathematical modeling techniques are given. Details of system identification tests and model estimation are introduced.

In Chapter 5, estimated system mathematical models are represented in modal space.

In Chapter 6, the feedback controller structures and development details of the controllers for LOS stabilization are given. the performance of the designed controllers is evaluated.

In Chapter 7, the architecture of the novel two-steps pointing strategy development and details are given. Theories and implementation details of different tracking methods are presented. Several simulation scenarios are developed to test these algorithms.

In Chapter 8, all works are done to the precise pointing of SATCOM on-the-move antenna terminal and results obtained throughout the process are summarized.

CHAPTER 2

SYSTEM ARCHITECTURE

2.1 Introduction

An antenna system consists of mainly radio frequency (RF) equipment, mechanical parts, electronic sensors and components. These can be explained in a detailed manner as follows. RF equipment is an antenna, an LNB, waveguide and connection cables. Bearings, mechanical components and connection joints compose mechanical parts or antenna pedestal. Gyroscopes, angular position sensors, inertial measurement units including GPS antennas are units of sensors. Also, motors and driver units are electronic components. In addition to these, there is a modem unit used to receive and send data.

2.2 Antenna and RF Signal

The antenna is the payload of this system and used for transmitting and receiving RF signals. Parabolic curvature, type and size of the antenna change depending on the application. There are different RF signal frequency ranges and this is also application-specific.

2.3 Mechanical Parts and Electronic Components

A pedestal is the general meaning of servo-mechanical systems. This system has degree of rotation depending on the application and can be steerable with electrical motors. Pedestal unit needs bearing to perform rotational motion and mechanical

connection parts. Also feedback sensors like gyroscopes, encoders to position and stability control. The degree of rotation of a pedestal depends on the aim of purpose. They can be one, two and multi-axis systems. There are mainly two concerns about that. One of them is the type of the RF signal. RF signal type can be categorized as circular and linear polarized. In linear polarization, electromagnetic waves propagate only vertically or horizontally. On the other hand, electromagnetic waves compose of vertical and horizontal waves in circular polarization. This propagation forms a circle around the source point when it is observed from a fixed point. Therefore, antenna feed must have a degree of rotation and this results in one more degree for the pedestal system. However, linear polarized antenna doesn't need this degree of rotation. The second main concern is the region of antenna operation. To be more specific, there exist a phenomenon known as keyhole region. This can be specified as near the equator region. In this area, the elevation angle should be close to 90° . If the pedestal is two-axis type that is elevation-azimuth, the antenna can not compensate base motion disturbances with azimuth axis. The elevation angle is near to keyhole boundary and this result in singularity known as gimbal-lock [1]. Azimuth axis motor requires infinite torque at this case. Therefore, it is not feasible and design of pedestal should be done considering this problem. One more degree of freedom is required for this type of operation. On the other hand, an additional degree of freedom means less stiff, more complex and more costly.

Sensors used in pedestal systems can be specified typically under two types. These are rate and angular position sensors. The rate sensor is placed on the axis of interest and used for stabilization loop feedback. There are different types of rate sensor which changes depending on accuracy and cost. In addition to that, Inertial Measurement Units sensor is used to measure the inertial motion of the base. Angular position sensors are used to measure the position of the pedestal axis. Resolvers and encoders are examples of these.

Performance of the antenna system affected by the degree of rotation, sensor type and performance, placement of sensor location and finally misalignments due to sensor or axis.

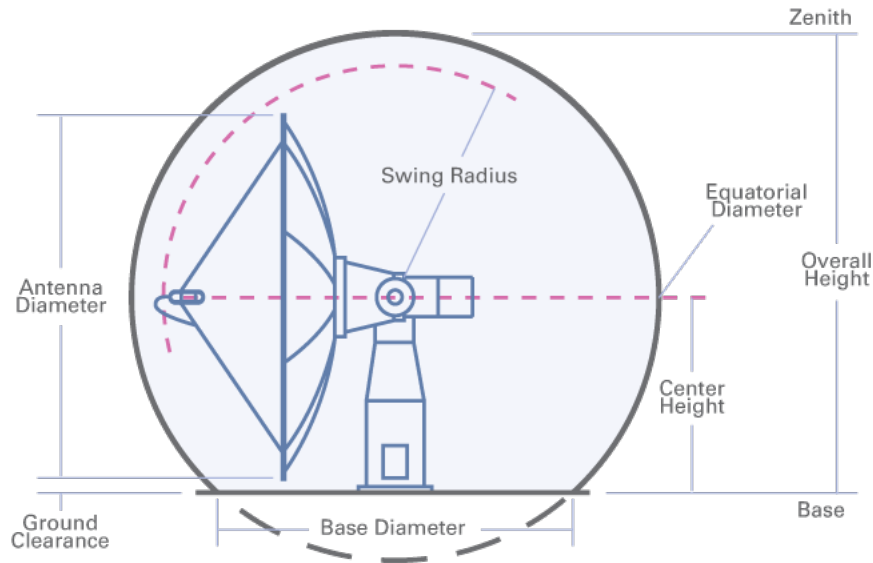


Figure 2.1: Representation of a Radome with an Antenna Gimbal [26].

2.4 Radome

Radome (radiation dome) is a protective house of microwave antenna or radar systems from external environmental disturbances [25]. These can be solid particles like salt, sand, snow and ice. Also, it is resistant to the sun, freezing temperatures and rain. Sizes, shapes and construction material change depending on antenna type, size and operating RF frequency. Structural load is an important design criterion. In addition to that, the material of radome is chosen with low signal losses and signal attenuation. There are different dimensional parameters that should be used during the design process. Representation of a radome with an antenna system inside and specified design dimensions are shown in Figure 2.1. As it can be understood, the antenna gimbal system is inside of the protective chamber. There is no need to consider environmental effects like wind load, high-temperature change during pedestal and controller design.



Figure 2.2: Satellite to Ground Terminal Communication Representation [27].

2.5 Satellite Communication

Satellite can be a man-made or natural body which moves around a larger body. In this context, only artificial satellites orbiting the Earth are mentioned. There exist different kinds of satellites depending on usage, orbit placement and lifetime.

A communication satellite operates as a relay or repeater station. It receives signals from Earth, then it processes and then send back to Earth. A basic representation of this operation can be seen in Figure 2.2. A ground antenna terminal system is used to communicate with another terminal by means of satellite. Therefore, communication from terminal to terminal can be performed within the coverage area of the satellite.

Antenna gimbal system works to receive and send data to the satellite. There is an RF modem unit at the heart of communication. RF signal is processed within the modem unit of the system. Modem packs the data before sending it to satellite and unpacks after received. This two-way process continues during communication. The complete diagram of an antenna terminal system is shown in Figure 2.3. Satellites transmit a low power signal which is called beacon. It can be represented as a call sign of the satellite and it can contain telemetry or health data. The main aim of this signal is to signify the presence of satellite and control up-link power.

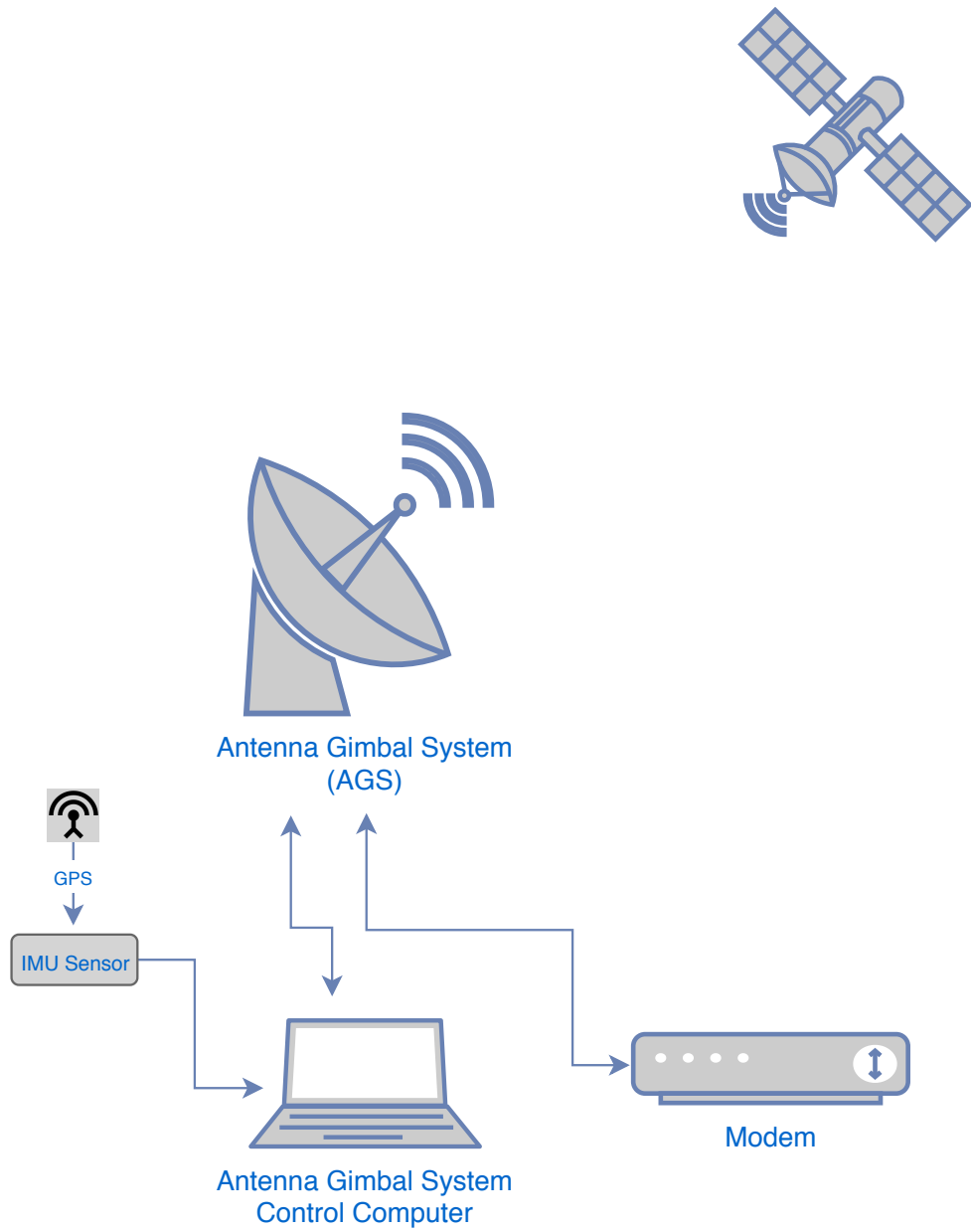


Figure 2.3: Block Diagram of Antenna Ground Terminal System

2.6 Pedestal Design Criteria

The antenna system should perform the required performance criteria of SATCOM communication. All the components of the system should be chosen for good pointing and tracking accuracy and high rate data transfer. All the sensors used in the system should have less delay, repeatable data and high resolution. Gyroscope sensor should have less bias and should be placed in an axis that is controlled. IMU sensor should not be affected by the magnetic area and environment. The controller processor should have less delay and a high sampling rate. Actuators should have higher acceleration and velocity characteristics. Bearing and other rotary joints should have less friction and weight. Mechanical parts of the system should be stiff and compact. In addition to these, the operation aim of antenna and payload size specifies the weight, inertia and size of the pedestal system. Usually, size and weight are limited and challenging environmental conditions exist. Therefore, the system should be compact and capable of required criteria. In addition to that, the pedestal should have good pointing accuracy. These results in higher system bandwidth and repeatable pointing precision and less jitter characteristics. To obtain system bandwidth higher, the first major resonance should be as high as possible. These all show that gimbal design is a critical optimization problem. These design principles are considered and all of them are tried to apply this gimbal system.

2.7 Controller Structure

Generally, electromechanical systems which have rotational degrees of freedom and capable of directing or pointing payload can be named as pedestal or gimbal systems. Main aim of these platforms is to stabilize LOS in terms of inertial space and steer payload. Inertially stabilized platforms have been used in different applications and areas over a long time [4]. Weapon platforms, cameras and telescopes are some of them. A block diagram of such a control system can be seen in Figure 2.4. Sensor data is used for controller feedback. These sensors are encoder or resolver, gyroscope, GPS and IMU. This feedback loop provides a core structure of the controller strategy. It compensates the host vehicle disturbances. It is represented in Figure 2.4 as "d".

In addition to that, there exists a tracking control loop in the antenna gimbal platform. It works as an outer feedback loop to track or direct the target. Target's signal strength is used to maximize the signal level with the special control algorithm. There are two types of pedestal control sequences. These are open-loop and closed-loop pointing.

2.7.1 Open-Loop Pointing

Open-loop pointing of an antenna system means directing the line of sight of the antenna to the satellite position. This is a simple case for fixed ground antenna because the GPS location of antenna and satellite is known and both of them are fixed. On the other hand, in the mobile antenna, it is not an easy case. There exist continuous base disturbances and the vehicle GPS location changes. Therefore, the satellite pointing vector must be calculated at every controller computer step time using the IMU data and GPS coordinate. The open-loop controller takes the pointing vector as a command to continuously direct antenna to satellite Figure 2.4. Pointing vector calculation is done considering everything is perfect. However, there can be a difference between the calculated position and the actual position of the source due to unexpected sources of error. Possible errors can be as follows; misalignment of the pedestal axis, gyroscope and IMU sensor, bias in the IMU and position sensors. Also, the satellite position has a drift as mentioned previous chapter, even if geostationary. These errors can result in mispointing of antenna line of sight and these are the Case-2 error. On the other hand, this method is simple to implement and operate for various types of systems. Therefore, it is used in low performance required systems.

2.7.2 Closed-Loop Pointing

RF performance of the SATCOM is very critical and must be high. There should be a really small amount of pointing error to achieve this level. Pointing error due to the open-loop movement can exist as mentioned previous chapter. Also, this error is time-varying and can increase with the motion of the vehicle. Therefore, there should be somehow active solution to compensate for this error. Close loop pointing is used to

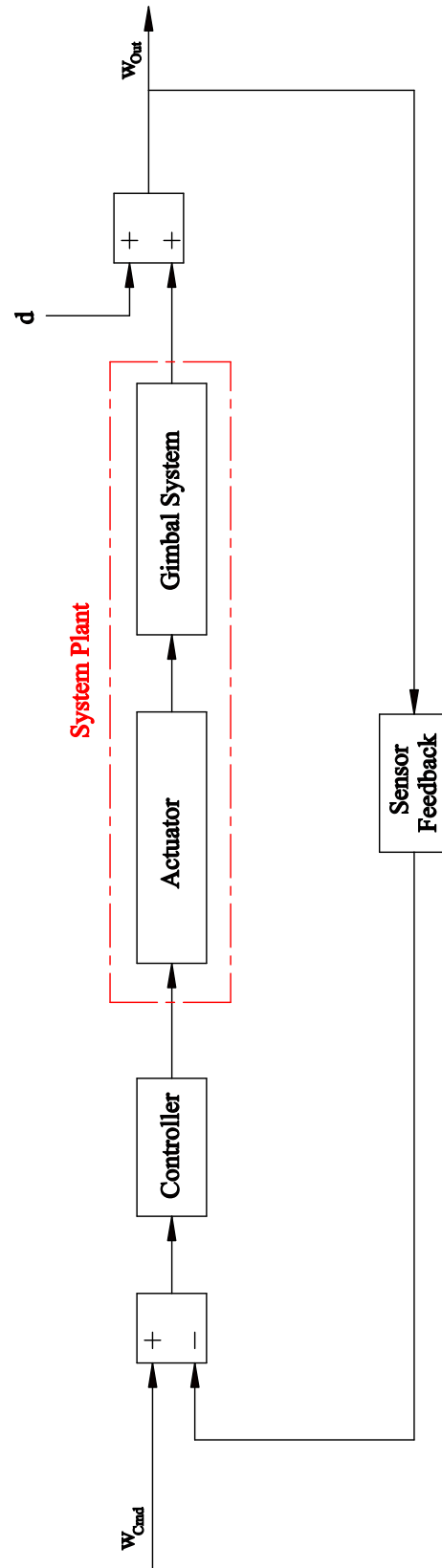


Figure 2.4: Block Diagram of Open-Loop General Control System

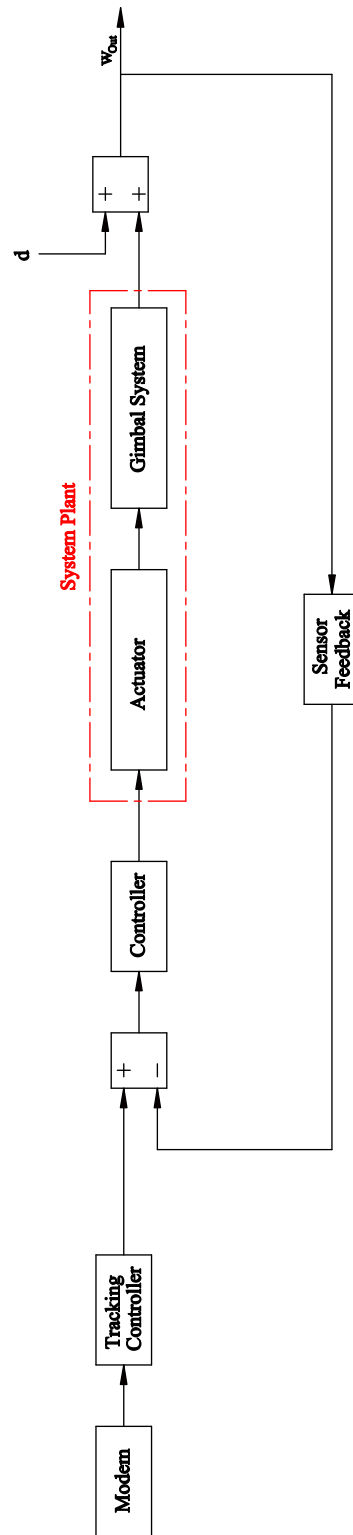


Figure 2.5: Block Diagram of Closed-Loop Gimbal Control System

overcome these problems. This is also called tracking. Block diagram representation of the closed-loop pointing is shown in Figure 2.5. The tracking loop uses the RF signal strength as feedback and tries to maximize this signal level. There are different types of tracking techniques as mentioned in the literature view chapter.

CHAPTER 3

EQUATIONS OF MOTION

Gimbal system kinematics and dynamics equations are studied in this section. Two axes "Azimuth over Elevation" type gimbal is used in this work. Antenna gimbal used in this study is given in Figure 3.2. Three reference frames are defined. Firstly, the base body frame (b) is placed on the host vehicle. Secondly, the azimuth frame (a) is fixed to the yaw gimbal body. The elevation frame (e) is placed on the pitch gimbal body. These and earth frames are presented in Figure 3.1. This system is used in maritime application. Ship represents the host vehicle for this study. It is given in Figure 3.3 with the frame-b axes.

3.1 Kinematic Equations

Angular kinematic quantities of each body are given as follows;

$\omega_V^{(b)}$: vehicle angular velocity in terms of b-frame

$\omega_{Az}^{(a)}$: azimuth gimbal angular velocity in terms of a-frame

$\omega_{El}^{(e)}$: elevation gimbal angular velocity in terms of e-frame

Gimbal relative angles and rates;

P: vehicle inertial roll velocity about x_b -axis

Q: vehicle inertial pitch velocity about y_b - axis

R: vehicle inertial yaw velocity about x_b - axis

Azimuth frame;

ψ : azimuth axis relative angle

$\dot{\psi}$: azimuth axis relative rate angle

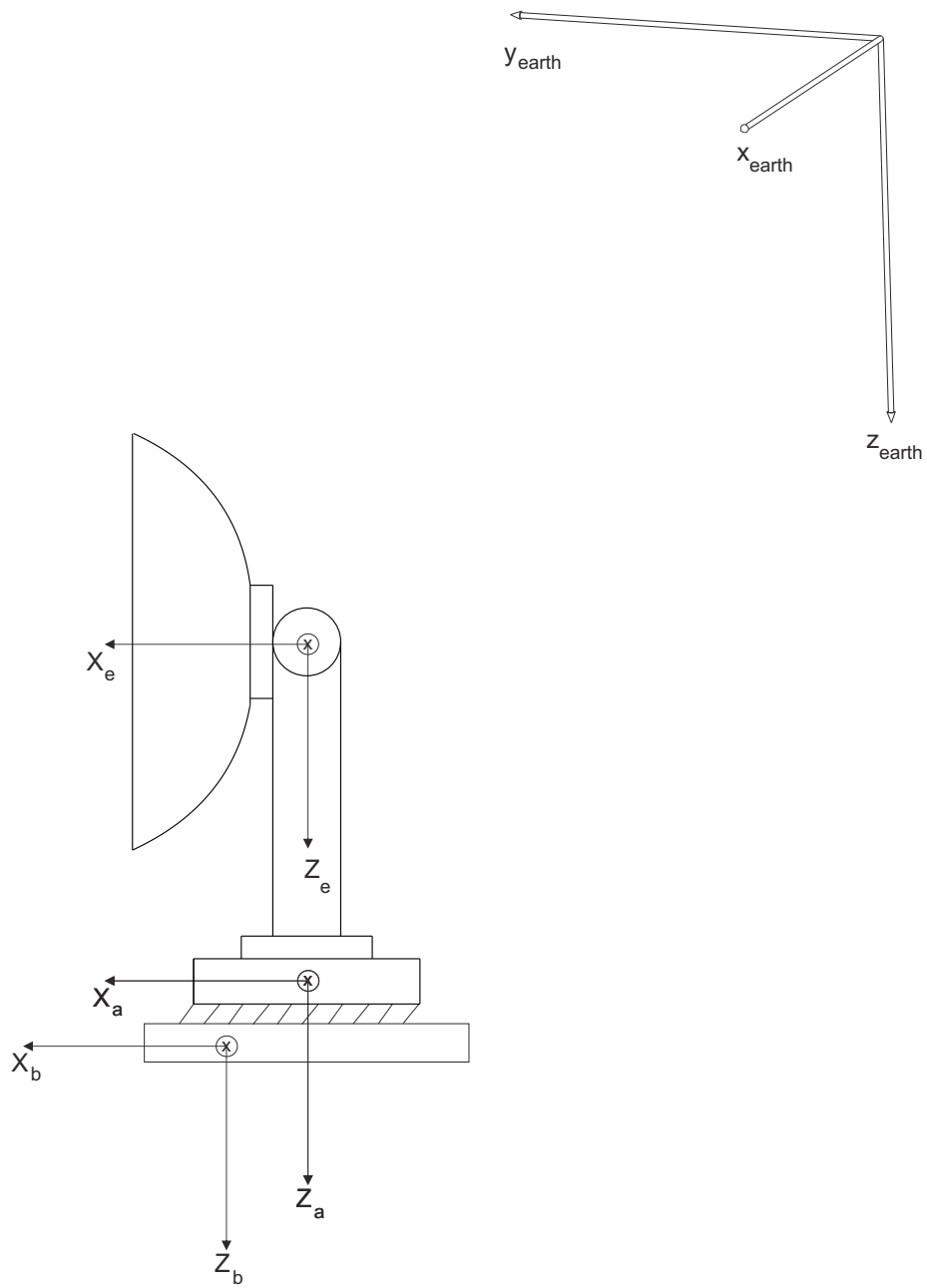


Figure 3.1: Rerefence Frames



Figure 3.2: Antenna Gimbal

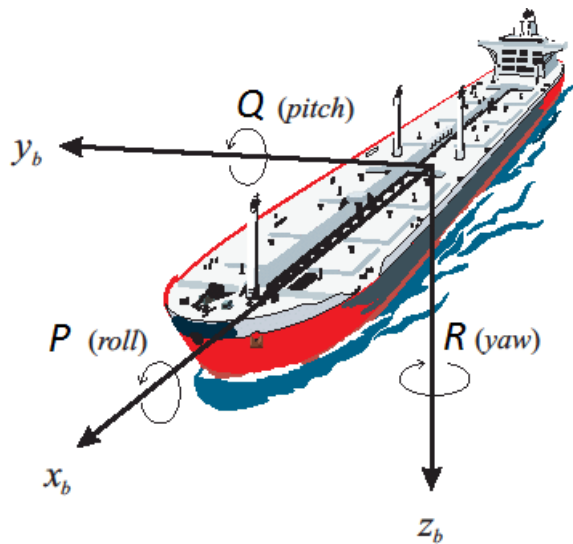


Figure 3.3: Base Body Frame [28].

Elevation frame;

θ : elevation axis relative angle

$\dot{\theta}$: elevation axis relative rate angle

Euler transform matrices can be written as follows;

$$E_x(\varphi) = \begin{bmatrix} 1 & 0 & 0 \\ 0 & \cos(\varphi) & \sin(\varphi) \\ 0 & \sin(\varphi) & \cos(\varphi) \end{bmatrix} \quad (31a)$$

$$E_y(\theta) = \begin{bmatrix} \cos(\theta) & 0 & -\sin(\theta) \\ 0 & 1 & 0 \\ \sin(\theta) & 0 & \cos(\theta) \end{bmatrix} \quad (31b)$$

$$E_z(\psi) = \begin{bmatrix} \cos(\psi) & \sin(\psi) & 0 \\ -\sin(\psi) & \cos(\psi) & 0 \\ 0 & 0 & 1 \end{bmatrix} \quad (31c)$$

Let's start with transforming the host vehicle frame to the gimbal outer frame. There exists relative motion between antenna gimbal and the host vehicle. Gimbal inertial rate vector ω_G can be written in terms of vehicle inertial angular rate vector ω_V and the relative rate vector $\omega_{G/V}$ can be written as follows;

$$\omega_G = E(\omega_V + \omega_{G/V}) \quad (32)$$

This can be written for outer frame as follows:

$$\omega_{Az} = E_z(\psi)(\omega_V + \omega_{Az/V}) \quad (33)$$

For inner gimbal frame:

$$\omega_{El} = E_y(\theta)(\omega_{Az} + \omega_{G/V}) \quad (34)$$

After substituting Equation (33) to Equation (34):

$$\omega_{El} = E_y(\theta)(E_z(\psi)(\omega_V + \omega_{Az/V}) + \omega_{El/V}) \quad (35)$$

Elevation gimbal angular velocities in terms of base frame angular velocity and gimbal angles can be obtained as Equation (36):

$$\begin{bmatrix} \omega_{ex} \\ \omega_{ey} \\ \omega_{ez} \end{bmatrix} = E_y(\theta) \left(E_z(\psi) \left(\begin{bmatrix} P \\ Q \\ R \end{bmatrix} + \begin{bmatrix} 0 \\ 0 \\ \dot{\psi} \end{bmatrix} \right) + \begin{bmatrix} 0 \\ \dot{\theta} \\ 0 \end{bmatrix} \right) \quad (36)$$

Elevation gimbal rates:

$$\omega_{ex} = \cos(\theta)(\cos(\psi)P + \sin(\psi)Q) - \sin(\theta)(R + \dot{\psi}) \quad (37a)$$

$$\omega_{ey} = -P \sin(\psi) + Q \cos(\psi) + \dot{\theta} \quad (37b)$$

$$\omega_{ez} = \sin(\theta)(\cos(\psi)P + \sin(\psi)Q) + \cos(\theta)(R + \dot{\psi}) \quad (37c)$$

Azimuth gimbal rates:

$$\omega_{ax} = P \cos(\psi) + Q \sin(\psi) \quad (38a)$$

$$\omega_{ay} = -P \sin(\psi) + Q \cos(\psi) \quad (38b)$$

$$\omega_{az} = R + \dot{\psi} \quad (38c)$$

The rate gyro is mounted in the inner axis as orthogonal to the LOS axis, as it can be seen in Figure 3.4. Therefore, e-frame represents the LOS frame.

Stabilization of the LOS;

for y-axis stabilization;

$$\omega_{ey} = 0 \quad (39a)$$

$$\dot{\theta} = P \sin(\psi) - Q \cos(\psi) \quad (39b)$$

As a result;

$$\omega_{iy} = 0; \quad (310)$$

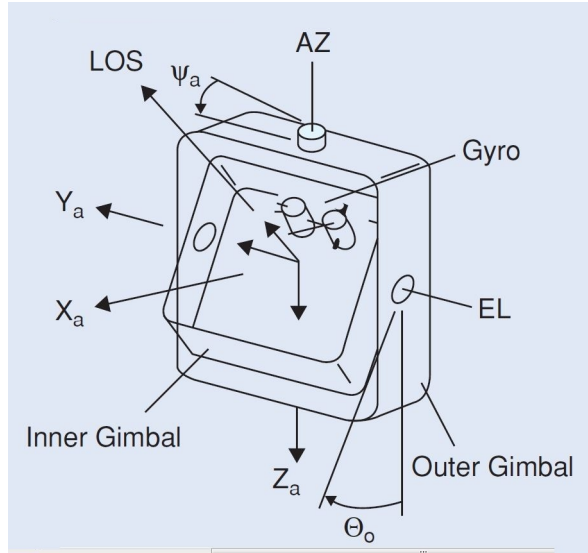


Figure 3.4: Axis of Gyro [4].

that means inner gimbal remains mass stabilized.

For z-axis stabilization;

$$\omega_{ez} = 0 \quad (311a)$$

$$\dot{\psi} = -\tan(\theta)(P \cos(\psi) + Q \sin(\psi)) - R \quad (311b)$$

Using Equation (37c) with Equation (38c)

$$\omega_{ez} = R + \dot{\psi} = -\tan(\theta)(P \cos(\psi) + Q \sin(\psi)) \quad (311c)$$

that means to stabilize the z-axis of the LOS outer gimbal must move. Kinematics couple directly into the outer axis and this can be seen from Figure 3.5. This coupling acts like torque disturbance and this results in stabilization performance lost on the outer axis. If the motor power is enough, it can be overcome. However, the kinematic coupling results in a known phenomenon of gimbal lock or loss of control. It is triggered by the inner gimbal inertial elevation angle, θ . There is no problem when $\theta < 90^\circ$. On the other hand, when $\theta \approx 90^\circ$, the outer gimbal rotation axis and LOS axis are aligned and the outer gimbal loses the control of LOS. The gimbal lock issue is a problem of all two-axis systems. The addition of the third axis can solve the problem. Also, the operation condition of the gimbal system should be considered. ASEL SAN antenna outer gimbal axis operation limit is $-10^\circ < \theta < 85^\circ$.

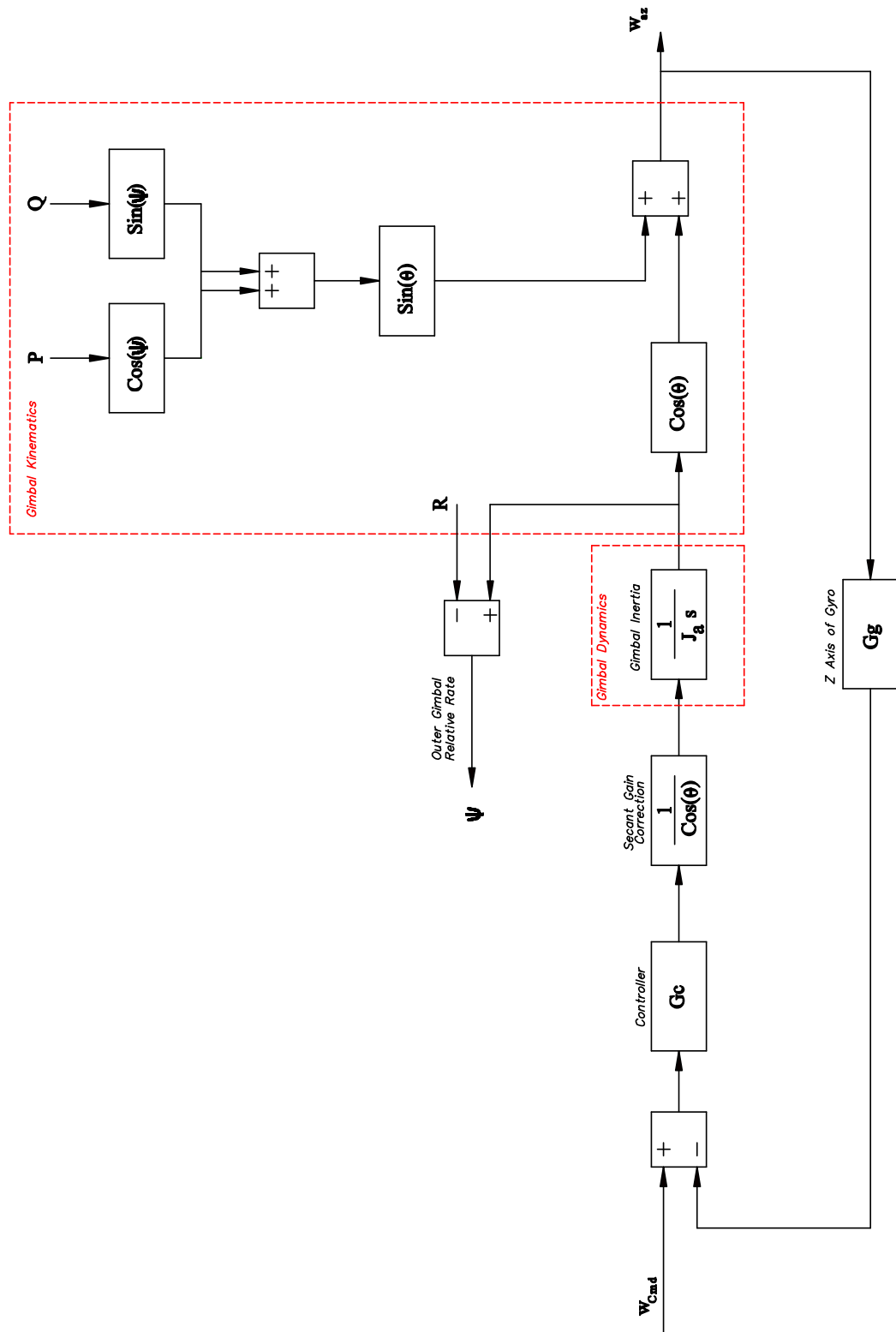


Figure 3.5: Diagram of the Azimuth Axis

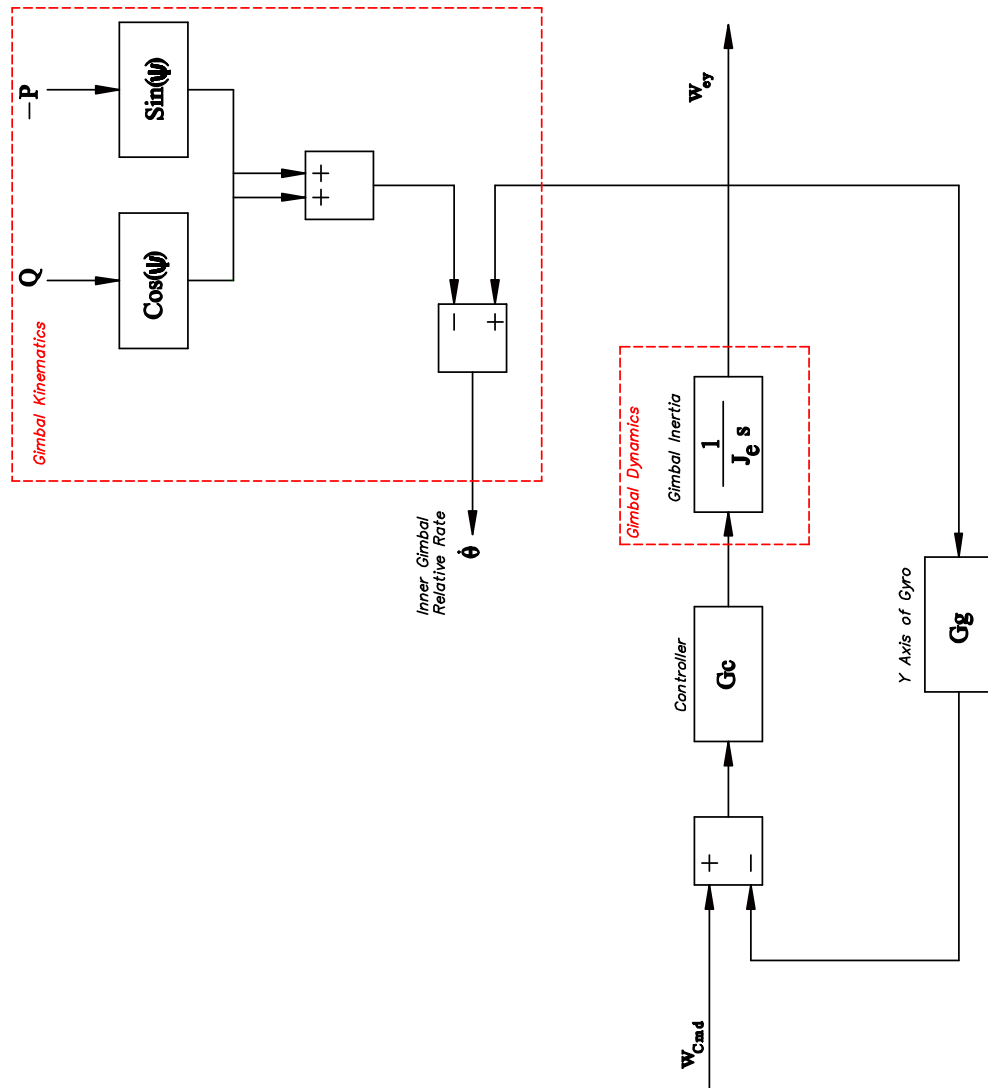


Figure 3.6: Diagram of the Elevation Axis

Therefore, the gimbal lock problem is not a problem for this antenna system and it is not considered during the thesis works. In addition to this, azimuth motor is chosen in consideration of performance criteria to compensate the coupling torque disturbance.

3.2 Dynamic Equations

General form of Euler's equation of motion for three axes nonsymmetrical, nonhomogenous mass system can be written as follows;

$$\sum_x T = \alpha_x J_{xx} + \omega_y \omega_z (J_{zz} - J_{yy}) - (\omega_y^2 - \omega_z^2) J_{yz} - (\omega_x \omega_y + \dot{\omega}_z) J_{xz} + (\omega_x \omega_z - \dot{\omega}_y) J_{xy} \quad (312a)$$

$$\sum_y T = \alpha_y J_{yy} + \omega_x \omega_z (J_{xx} - J_{zz}) - (\omega_z^2 - \omega_x^2) J_{xz} - (\omega_z \omega_y + \dot{\omega}_x) J_{xy} + (\omega_x \omega_y - \dot{\omega}_z) J_{yz} \quad (312b)$$

$$\sum_z T = \alpha_z J_{zz} + \omega_x \omega_y (J_{yy} - J_{xx}) - (\omega_x^2 - \omega_y^2) J_{xy} - (\omega_x \omega_z + \dot{\omega}_y) J_{yz} + (\omega_x \omega_z - \dot{\omega}_x) J_{xz} \quad (312c)$$

Cross products of inertia terms become important in the case of a nonsymmetrical and nonhomogenous mass system as it can be seen Equations (312a) to (312c). These terms act like disturbance torques. ASELN antenna reflector is symmetrical and azimuth axis gimbal is made almost symmetrical. In addition to that, all axes are well balanced to move the whole system center of mass and are aligned with the gimbal rotational axes. As a result, equation of motion can be written as follows;

$$\sum_x T_{Az} = \alpha_{Az} J_{Az} \quad (313a)$$

$$\sum_y T_{El} = \alpha_{El} J_{El} \quad (313b)$$

Torques are composed of motor torques and base motion disturbance torques.

$$\sum T = \sum T_{motor} + \sum T_{disturbance} \quad (314)$$

3.3 State Equations

The general form of a state equation can be written as follows:

$$\dot{x} = Ax + Bu + Gw \quad (315)$$

State, input and disturbance matrixes are defined as follows:

$$x = \begin{bmatrix} \dot{\theta} \\ \dot{\psi} \\ \theta \\ \psi \end{bmatrix} \quad u = \begin{bmatrix} T_{el} \\ T_{az} \end{bmatrix} \quad w = \begin{bmatrix} P \\ Q \\ R \end{bmatrix} \quad (316)$$

$$A = \begin{bmatrix} 0 & 0 & 0 & 0 \\ 0 & 0 & 0 & 0 \\ 1 & 0 & 0 & 0 \\ 0 & 1 & 0 & 0 \end{bmatrix} \quad B = \begin{bmatrix} 1/J_{el} & 0 \\ 0 & 1/J_{az} \\ 0 & 0 \\ 0 & 0 \end{bmatrix} \quad G = \begin{bmatrix} 0 & 0 & 0 \\ 0 & 0 & 0 \\ -\sin(\psi) & \cos(\psi) & 0 \\ 0 & 0 & 1 \end{bmatrix} \quad (317)$$

3.4 Measurement Equations

Measurement equations can be written as follows:

$$y = Cx + Du + Hw \quad (318)$$

$$y = \begin{bmatrix} \omega_{gyro,y} \\ \omega_{gyro,z} \\ \theta \\ \psi \end{bmatrix} \quad u = \begin{bmatrix} T_{el} \\ T_{az} \end{bmatrix} \quad w = \begin{bmatrix} P \\ Q \\ R \end{bmatrix} \quad (319)$$

$$C = \begin{bmatrix} 1 & 0 & 0 & 0 \\ 0 & \cos(\theta) & 0 & 0 \\ 0 & 0 & 1 & 0 \\ 0 & 0 & 0 & 1 \end{bmatrix} \quad D = \begin{bmatrix} 0 & 0 \\ 0 & 0 \\ 0 & 0 \\ 0 & 0 \end{bmatrix} \quad (320)$$

$$H = \begin{bmatrix} -\sin(\psi) & \cos(\psi) & 0 \\ \cos(\psi)\sin(\theta) & \sin(\theta)\sin(\psi) & \cos(\theta) \\ 0 & 0 & 0 \\ 0 & 0 & 0 \end{bmatrix} \quad (321)$$

CHAPTER 4

SYSTEM IDENTIFICATION

An analytical model of the antenna system is obtained in this part. This model will be used in controller design steps and in simulations.

The model can be approximated using the physical laws that are Lagrange's equations of motion, Newton's laws or D'Alembert's principle. Also, test data can be used from system identification techniques or finite-element models. Time and frequency domain representation can be used for obtained models [29].

The theoretical equations of motion approach results in complex and coupled mathematical relations which are hard to handle and even sometimes not possible to solve. Also, this type of complex system has nonlinear characteristics and it can not be possible to represent mathematically.

Gimbal structure can be obtained from finite-element model. However, structural dynamics have rigid behavior and flexible deformation. Also, these systems are consist of different components and connection parts. It is hard to precisely model mechanical and material properties of them. Therefore, the finite-element model is not accurate enough to simulate the real system.

System identification is a technique used to get the mathematical model of a dynamic system using field test data. The system is excited with an input signal and its response is measured. The model is obtained using these input and corresponding response signals. The model accuracy depends on test conditions and test data. If tests are conducted properly, the approximation can be good enough.

4.1 Nonlinear Effect

Real physical systems have both linear and nonlinear behavior. It is complicated to handle and use theories with nonlinear properties. On the other hand, these can be modeled and compensated from system behavior. System identification tests are conducted after the nonlinear effect compensated.

4.1.1 Friction

Friction can be defined as torque or a force that results from the relative motion of the contacting bodies. Gimbal systems use roller bearings at each rotation axis. These causes mainly static, dynamic and viscous type frictions. Static friction which is also called stiction is the force or torque required to start motion [30]. Dynamic or Coulomb friction is the term independent of velocity and always acts to oppose the direction of motion. Friction torque and velocity relation can be seen in Figure 4.1. In addition to that, it is represented in Equation (41).

$$F = F_c \text{sgn}(\omega) \quad (41)$$

Viscous friction exists between solid and lubricant. It depends on the velocity. Precise pointing of the AGS is very important in terms of system performance criteria. The AGS moves at very slow angular rates to track the RF signal. Friction is an important problem for this type of system. Therefore, the antenna can not make a smooth motion during RF tracking and this will result in unwanted LOS pointing error.

4.1.1.1 Azimuth Axis

Constant velocity tests are performed to measure the friction torque. Axis position and torque data are logged. Different velocities are chosen to see the effect of velocity during tests. Roller bearing which is used has high quality and continuous properties at all positions. Therefore, there is no need to test different azimuth positions.

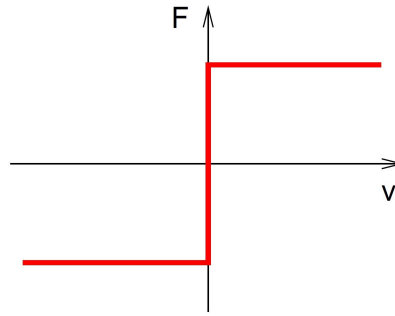


Figure 4.1: Relation of Friction Torque with Velocity

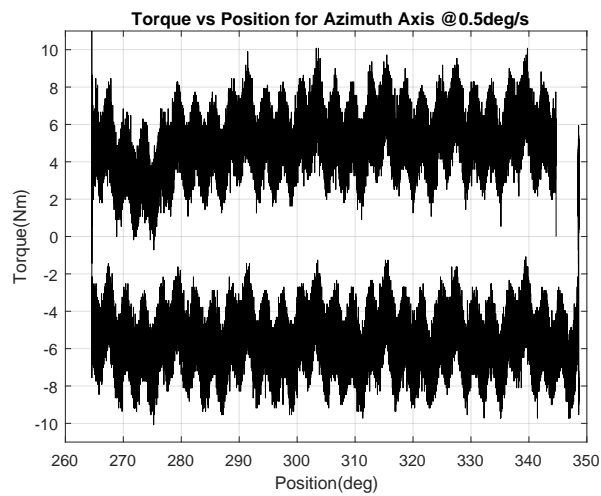


Figure 4.2: Diagram of Torque vs Position for Azimuth Axis, @0.5deg/sec

Test-1

Test parameter is as follows;

Angular velocity=0.5 deg/sec

Graph of the test "Torque vs Position" of Azimuth axis can be seen in Figure 4.2

Test-2

Test parameter is as follows;

Angular velocity=1 deg/sec

Graph of the test "Torque vs Position" of Azimuth axis can be seen in Figure 4.3

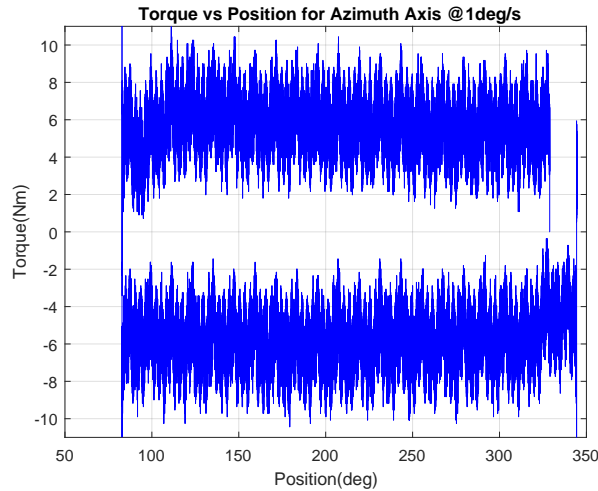


Figure 4.3: Diagram of Torque vs Position for Azimuth Axis, @1deg/sec

As a result of these tests, the following results can be obtained:

- Friction value is almost the same for different velocities.
- Viscous friction is very low and even almost no effect on this motion. Also, gimbal operational rates are very low. Hence, viscous term can be disregarded.
- Coulomb friction model can be used for compensation
- Coulomb friction coefficient=5.76 Nm

4.1.1.2 Elevation Axis

Constant velocity tests are performed to measure the friction torque. Different velocities are chosen to see the effect of velocity during tests. Roller bearing which is used has high quality and continuous properties at all positions. Therefore, there is no need to test different elevation positions.

Test-1

Test parameter is as follows;

Angular velocity=0.5 deg/sec

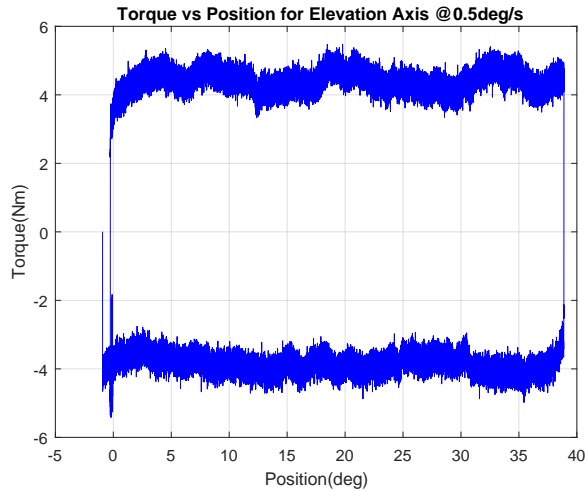


Figure 4.4: Diagram of Torque vs Position of Elevation Axis,, @0.5deg/sec

Graph of the test "Torque vs Position" of elevation axis can be seen in Figure 4.4

Test-2

Test parameter is as follows;

Angular velocity=1 deg/sec

Graph of the test "Torque vs Position" of elevation axis can be seen in Figure 4.5 As a result of these tests, the following results can be obtained:

- Friction value is almost the same for different velocities.
- Viscous friction is very low and even almost no effect on this motion. Also, gimbal operational rates are very low. Hence, viscous term can be disregarded.
- Coulomb friction model can be used for compensation
- Coulomb friction coefficient= 3.85 Nm

4.1.2 Cross Coupling

The inertia of azimuth change with the position of elevation. Therefore, there exist dc gain differences during tests due to inertia change. Also, rate gyro is attached

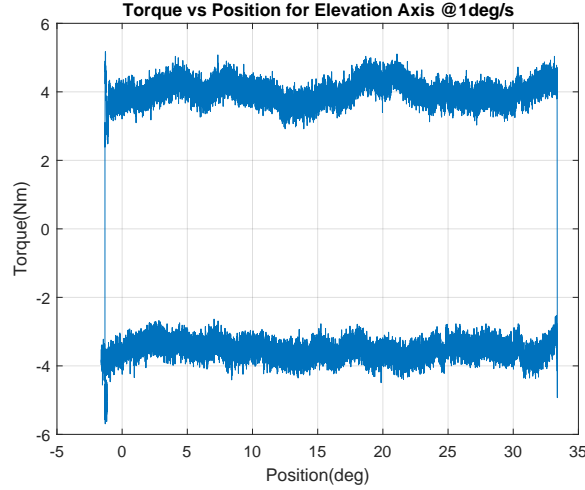


Figure 4.5: Diagram of Torque vs Position of Elevation Axis, @1deg/sec

to the elevation axis and the coupling of the elevation axis results in nonlinear dc gain difference. As a result of these, there is a need for normalization factors. The inertia of the azimuth axis is calculated for different elevation positions using PRO-Engineer 3D CAD software. After calculations, a function which is a summation of the sine function is obtained to fit the inertia data. The summation of sine is used to reduce the complexity of the function. Estimation and CAD calculations are plotted in Figure 4.6. The inertia of the azimuth axis depending on the elevation axis position can be written as follows;

$$J_{Az}(\theta) = 28.08 + 0.355\sin(0.0318\theta + 2.35) \quad \text{kg m}^2 \quad (42)$$

Coupling of the elevation axis can be solved with sec correction factor.

$$\sec(\theta) = \frac{1}{\cos(\theta)} \quad (43)$$

As a result, normalization factor can be written as follows;

$$\text{NormalizationFactor} = J_{Az}(\theta) * \sec(\theta); \quad (44)$$

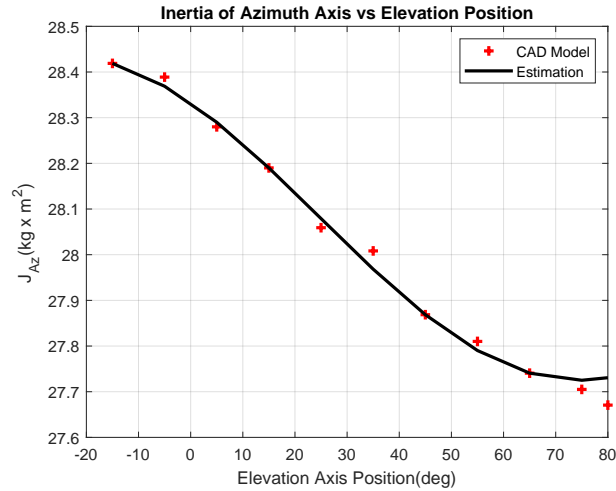


Figure 4.6: Estimation of Azimuth Axis Inertia with Respect to Elevation Position

4.2 Identification Test

The system identification method is used to model the AGS. There are different application types mainly depend on excitation signal; such as periodic, transient and non-transient aperiodic signals. An open-loop swept-sine method is used during tests. The frequency of the sine wave is swept up or down during one measurement period.

A sinusoidal test signal is applied to the system and response is obtained. The response has the same frequency but different amplitude and phase with the input. Test process is introduced in Figure 4.8. Details of identification tests are given in Figure 4.7. A real-time target machine is used to generate an excitation signal and collect measured data. Actuators of each axis are used to excite the AGS. The gyro-feedback sensor of AGS is used to measure response. This input and output are used to get the frequency response of the system.

Azimuth and elevation axes are tested separately to identify each axis characteristics. There exists a very weak coupling between them. However, azimuth axis characteristic changes with the elevation position. Therefore, the position of elevation is accounted for azimuth model. On the other hand, this is not the case for the elevation axis. Its behavior does not depend on position.

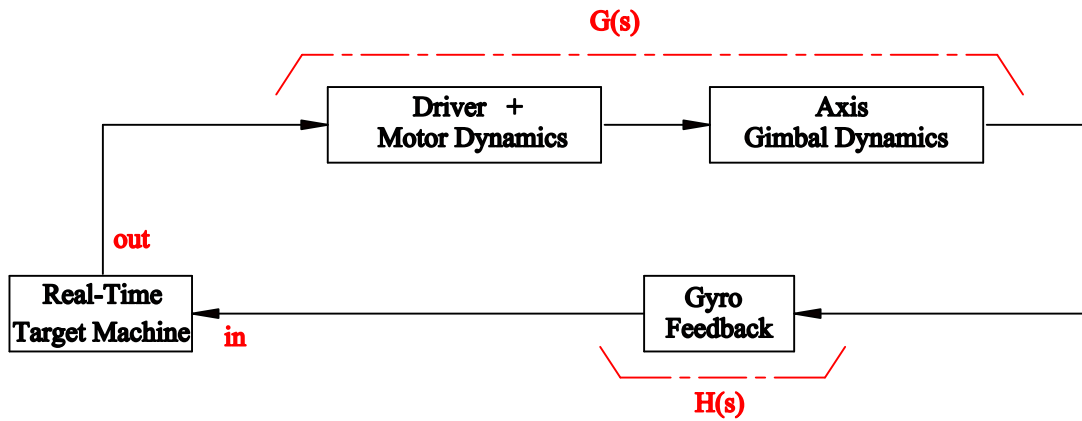


Figure 4.7: Diagram of System Identification Test Model



Figure 4.8: Frequency Response Test Representation

4.2.1 Azimuth Axis

Azimuth axis tests are performed for different elevation positions. The position change is considered in the operation range of 80° to -10° . Test details are given in Table 4.1. All of the tests are conducted at 1ms sample time.

Results

After completing all the previously defined tests, frequency responses are plotted on the same figure. This can be seen in Figure 4.9.

The following results can be obtained from the test results;

- The normalization factor is worked well, it can be seen from the low-frequency region. DC gain of all the test is almost the same.
- Low-frequency region shows almost rigid body behavior.

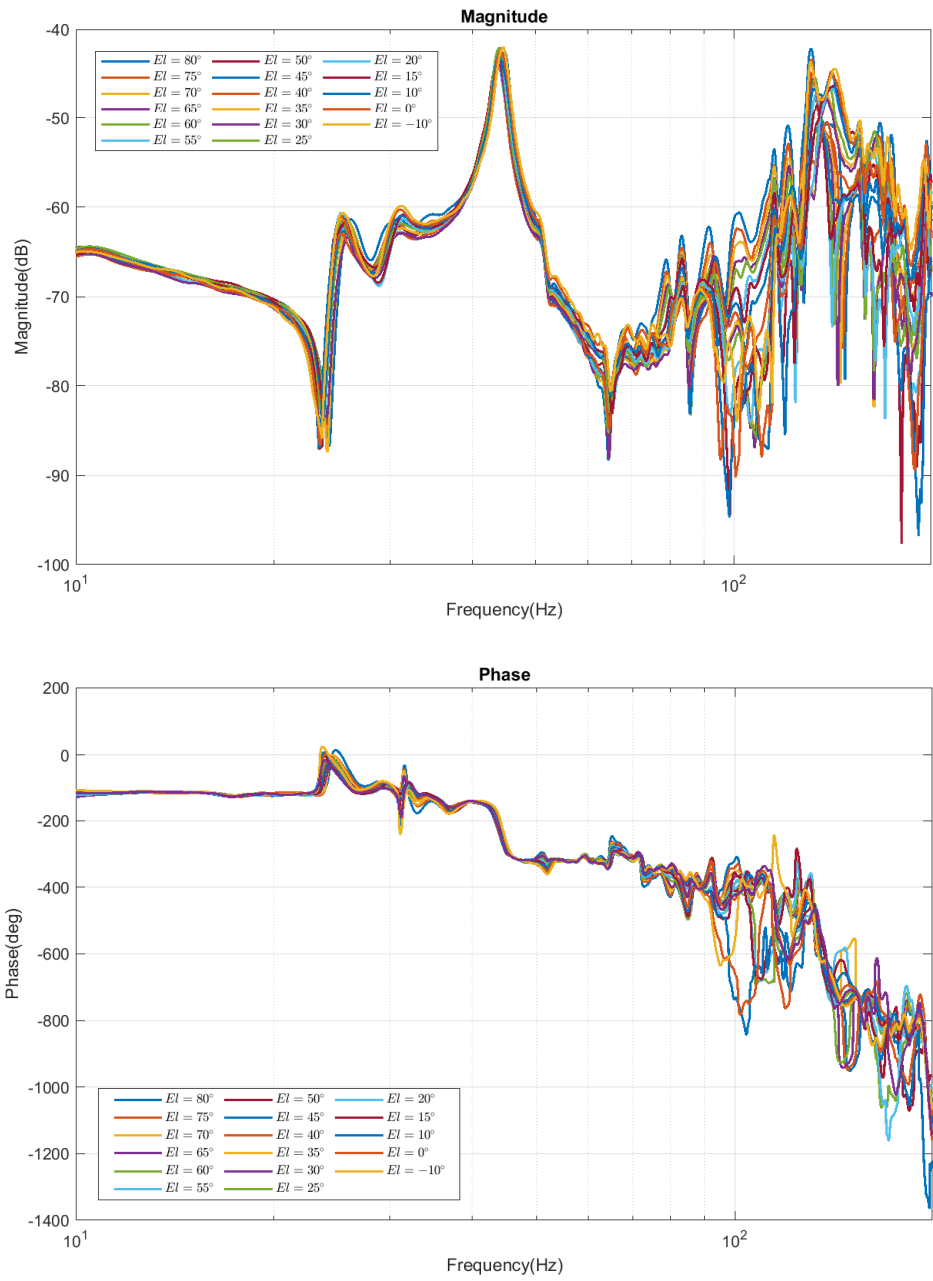


Figure 4.9: Bode Diagram of Azimuth Axis for Different Elevation Position

Table 4.1: Test Parameter Table for Azimuth Axis System Identification

Test no	Elevation Position, θ°	Frequency Range (Hz)	Applied Torque (Nm)
1	80	10-200	70
2	75		
3	70		
4	65		
5	60		
6	55		
7	50		
8	45		
9	40		
10	35		
11	30		
12	25		
13	20		
14	15		
15	10		
16	0		
17	-10		

- System dynamics are almost the same in the mid-frequency region for all tests.
- Elevation position affects only the natural frequencies of the modes and damping coefficients on the high-frequency region.
- These tests are conducted for different applied torques from lower to higher values. All the results give almost similar responses. Therefore, applied torque is enough to excite the system and get system dynamics.
- These tests are performed with the same conditions at different times. Results show almost the same responses in all cases. That means the nonlinear effect can be compensated and system behavior is not changing with time.

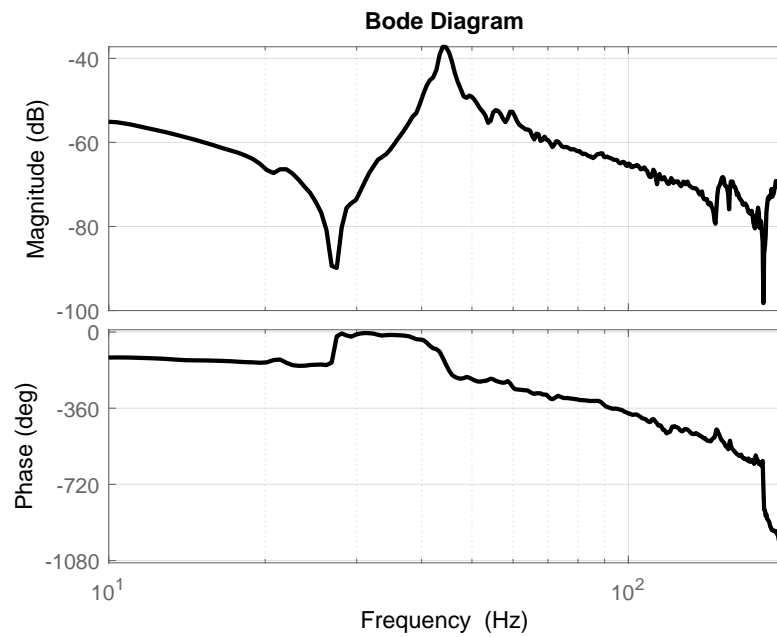


Figure 4.10: Bode Diagram of Elevation Axis

4.2.2 Elevation Axis

The elevation axis is not affected by cross-coupling, position depended on inertia and stiffness change as mentioned previous section. Therefore, the elevation axis frequency response test is not performed for different positions.

Test-1

Swept-sine test parameter is as follows;

Frequency range= 10 – 200 Hz

Applied Torque= 10 Nm

Measurement= 3 axis gyroscope, attached on elevation axis

All the tests are conducted at 1ms sample time.

Bode diagram of this test can be seen in Figure 4.10

The following results can be obtained from the test results;

- Low-frequency region shows almost rigid body behavior.
- These tests are conducted for different applied torques from lower to higher values. All the results give almost similar responses. Therefore, applied torque is enough to excite the system and get system dynamics.
- These tests are performed with the same conditions at different times. Results show almost the same responses. That means system behavior is not changing with time.

4.3 Estimation of Transfer Function from Test Data

The AGS analytical model is estimated using the following test results and assumptions;

- AGS operation region is within the low-bandwidth region . That means the mid-frequency region is more important to represent real working conditions. However, the high-frequency region which is higher than 100Hz less important.
- Although test results are similar for different applied torque values, actuator torques can not be enough to excite the AGS. Therefore, the high-frequency region responses are not good to get accurate responses during tests.
- Change of natural frequencies and damping factors are within a very small region on the operation bandwidth. Therefore, it is assumed that one transfer function is enough to model the AGS dynamically.
- The general form of the approximated transfer function is expressed in the Laplace domain as Equation (45). It consists of inertia, time delay and structural dynamics.
- Estimation is done to get stable and minimum phase transfer function
- Identified model is tried to be accurate enough with min order and important structural modes
- Structural modes are not coupled. The response of the system is a sum of individual mode responses [29]

- Structural resonances can be represented in multiple cascaded bi-quad filters instead of high order canonical form transfer function [31].
- Detailed analyses of the system can be done to get a more complex analytical model in future works. However, it is out of the scope of this study.

$$Tf = e^{-st_{delay}} \frac{1}{Js} G \quad (45)$$

4.3.1 Azimuth Axis

Estimation

Estimation of the transfer function is started with the selection of resonance and anti-resonance frequencies. Then, damping coefficients are assumed at the beginning. The final form of the transfer function is obtained at the end of an iterative process. The transfer function can be represented analytically as Equation (46). Correlation of the transfer function with the psychical system is analyzed with details in Chapter 5.

Frequency response of the estimation is plotted with the test responses in Figure 4.11. The estimated model covers the dominant resonance peaks and the estimation represents an almost close response to the test data. In addition to that, zeroes and poles are checked to be sure whether the transfer function is stable.

$$Tf = e^{(-0.01s)} \frac{1}{27.9s} G \quad (46a)$$

$$G = \frac{3.8533(s^2 + 553.2s + 7.966e04)(s^2 + 1.956s + 2.244e04)}{(s^2 + 7.873s + 2.479e04)(s^2 + 8.067s + 7.737e04)} \dots \frac{(s^2 + 239.4s + 1.825e05)}{(s^2 + 19.74s + 6.766e05)} \quad (46b)$$

4.3.2 Elevation Axis

Estimation

Estimation of the transfer function is started with the selection of resonance and anti-resonance frequencies. Then, damping coefficients are assumed at the beginning.

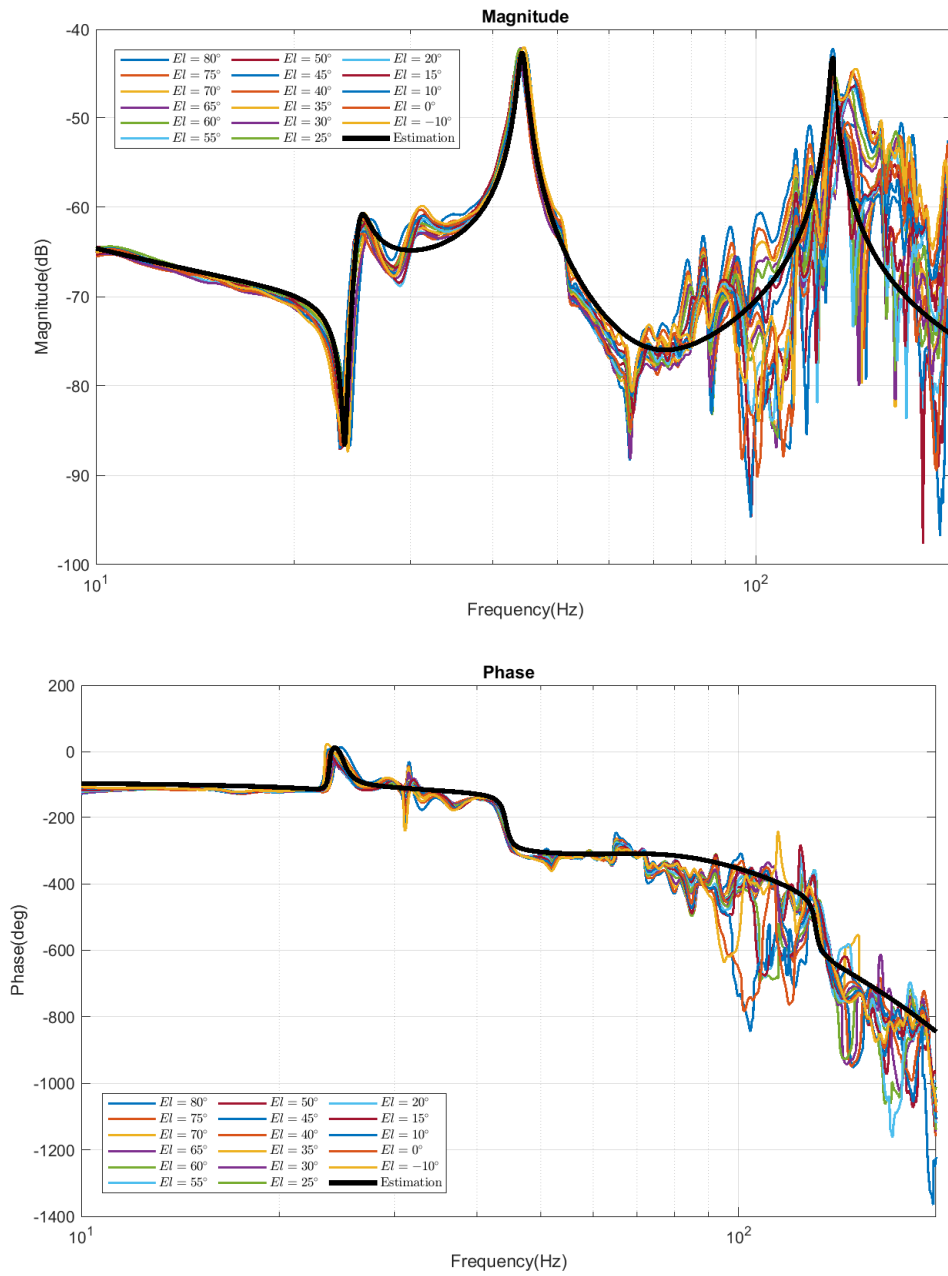


Figure 4.11: Transfer Function Estimate of Azimuth Axis

The final form of the transfer function is obtained at the end of an iterative process. The transfer function can be represented analytically as Equation (47). Correlation of the transfer function with the psychical system is analyzed with details in Chapter 5.

The frequency response of the estimation is plotted with the test responses in Figure 4.12. The estimated model covers the dominant resonance peaks and the estimation represents an almost close response to the test data. In addition to that, zeroes and poles are checked to be sure whether the transfer function is stable.

$$Tf = e^{(-0.008s)} \frac{1}{8.2s} G \quad (47a)$$

$$G = \frac{2.814(s^2 + 3.414s + 2.911e04)(s^2 + 74.38s + 8.647e05)}{(s^2 + 13.57s + 7.672e04)(s^2 + 201.6s + 9.215e05)} \quad (47b)$$

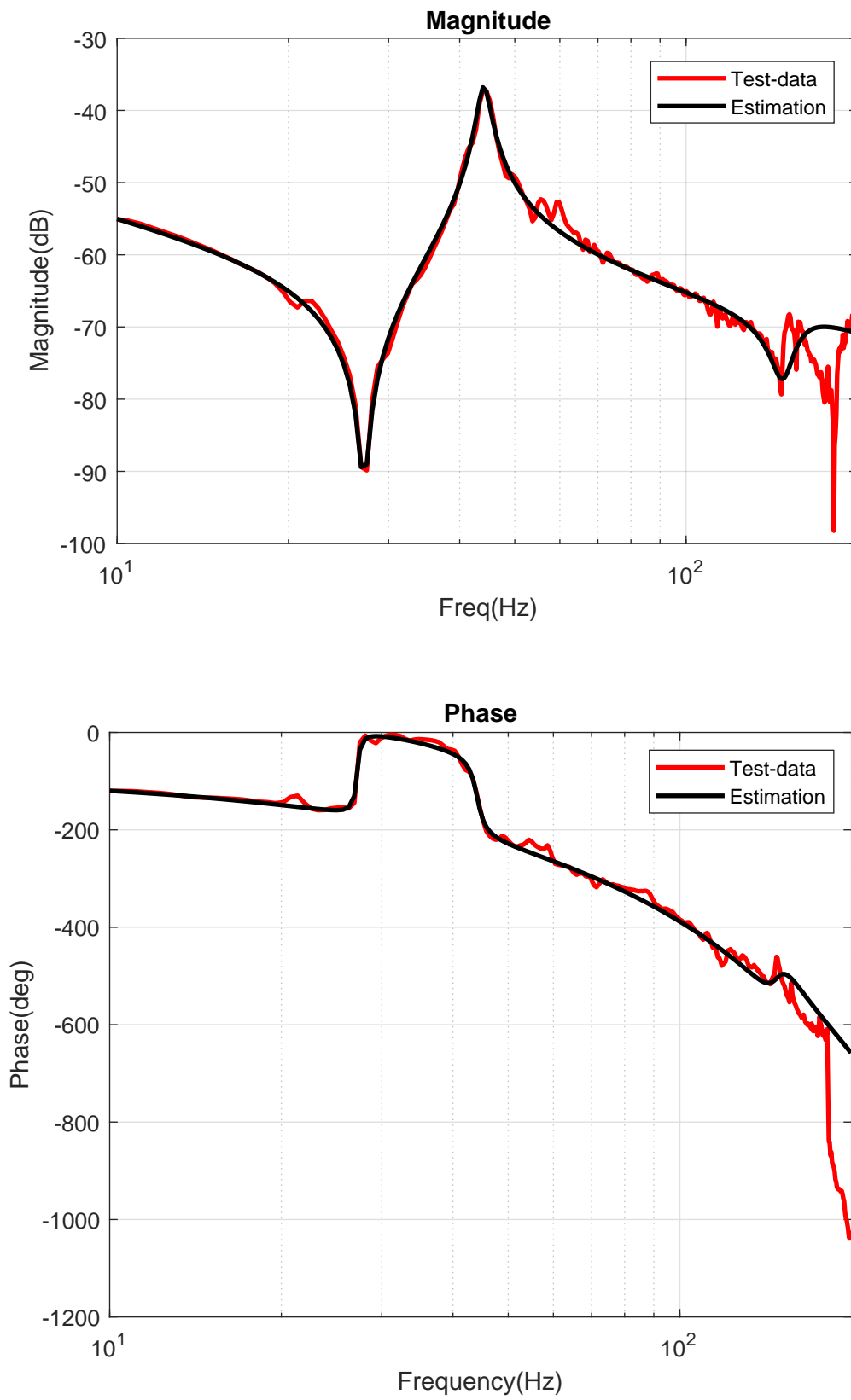


Figure 4.12: Transfer Function Estimate of Elevation Axis

CHAPTER 5

MODAL REPRESENTATION OF TRANSFER FUNCTIONS

Transfer functions of the azimuth and the elevation axes are obtained in the Chapter 4. In this chapter, details of the relation between the AGS's transfer function and structural modes are analyzed. The analytical model of the system was obtained with the system identification technique. The system can be approximated as a lumped-mass model. This approximation consists of spring, viscous damper and inertia elements. Equations of motion can be written using Newton's Second Law. On the other hand, this electro-mechanic system has a complex assembly. This results in the coupling between viscous dampers and springs on the equations. It is complicated to know the mass, spring and damping distribution on the real system. The system has complex structural dynamic behavior, it is hard to decouple and define the order of the system. On the other hand, pole locations of the system characteristic equation can be measured and structural dynamics can be expressed analytically. Identification tests showed that transfer function approximation accurate enough to represent system characteristics.

5.1 Transformation to Modal Space

Modal coordinates are defined through the displacements and velocities of the structural modes [29]. These coordinates are independent of each other so the equation of motion can be decoupled by transforming to model space and this helps to overcome complex mathematical calculations.

Equations of motion of a proportionally, viscously damped multi-degree-of-freedom system that consists of n DOFs as follows in Equation (51).

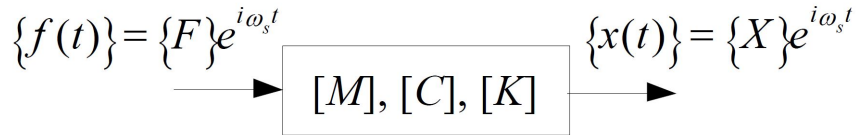


Figure 5.1: Representation of Physical Domain [32].

where:

$[M]$: mass matrix

$[C]$: damping matrix

$[K]$: stiffness matrix

f : applied external force vector

\ddot{x}, \dot{x}, x : acceleration, velocity and displacement vectors

$$[M] \{\ddot{x}\} + [C] \{\dot{x}\} + [K] \{x\} = \{f\} \quad (51)$$

Block diagram representation of this system with input and output form in the physical domain can be seen in Figure 5.1.

The following assumptions are made during transformation analyzes [33].

Linearity

The system behaves linearly so the response of the system is always proportional to excitation. This assumption has the following three implications for the Frequency Response Function (FRF) measurements. Small deflections are assumed during operation hence linearity assumption is applicable.

Superposition

The response of the system is independent of excitation waveform used. For example, broadband signal excitation results in a similar response with swept sine.

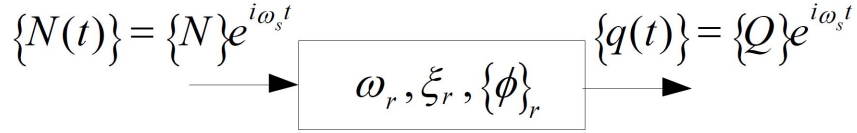


Figure 5.2: Representation of Modal Domain [32].

Homogeneity

There is no relation between the amplitude of the excitation and frequency response.

Reciprocity

It is expressed by Maxwell's Reciprocity Theorem. FRF measurement between any two DOFs does not depend on which one is excited or response obtained.

Physical coordinate "x" can be written in terms of the modal matrix " Φ " and modal coordinates "q" as follows in Equation (52).

$$\{x\} = [\Phi] \{q\} \quad (52)$$

or

$$x_j(t) = \sum_{r=1}^n \phi_{r,j} q_r(t) \quad (53)$$

The modal coordinate representation can be obtained in Equation (54) by substituting Equation (52) to Equation (51).

$$[M] [\Phi] \{\ddot{q}\} + [C] [\Phi] \{\dot{q}\} + [K] [\Phi] \{q\} = \{f\} \quad (54)$$

The final form of the system equation can be obtained as Equation (55) after making substitution and simplification steps in [29].

$$\ddot{q}_r + 2\xi_r \omega_r \dot{q}_r + \omega_r^2 q_r = N_r(t) = \sum_{k=1}^n \phi_{r,k} f_k \quad (55)$$

System is represented by the r-th modal parameters; ξ_r, ω_r and $\{\phi_r\}$. q_r is the modal coordinate and output of the modal domain model. N_r is the modal force and input of the modal domain model.

Assume that; harmonic force is applied on the k-th location:

$$q_r = Q_k \varepsilon^{i\omega_s t} \quad f_k = F_k \varepsilon^{i\omega_s t} \quad (56)$$

Substituting by Equation (56) to Equation (55) and after making manipulations:

$$Q_k = \frac{F_k \phi_{r,k}}{\omega_r^2 + (2\xi_r \omega_r \omega_s) i - \omega_s^2} \quad (57)$$

Block diagram representation of the system can be seen in Figure 5.2

Also, after substituting Equation (53) to Equation (57). Response at node j with respect to the force at node k can be obtained

$$\frac{X_j}{F_k} = \sum_{r=1}^n \frac{\phi_{r,j} \times \phi_{r,k}}{\omega_r^2 + (2\xi_r \omega_r \omega_s) i - \omega_s^2} \quad (58)$$

this can be expressed in s domain as follows in Equation (59).

$$G_{j,k} = \sum_{r=1}^n \frac{\phi_{r,j} \times \phi_{r,k}}{s^2 + 2\xi_r \omega_r s + \omega_r^2} \quad (59)$$

It means that the structural transfer function composes from the summation of independent modal transfer functions, Equation (510). Also, the Bode plot representation of structural transfer function can be seen in Figure 5.3.

$$G = G_{m1} + G_{m2} + G_{m3} + G_{m4} + G_{m5} + \dots + G_{mr} \quad (510)$$

The Transfer function is represented in polynomial form. It is also possible to rewrite this in partial fraction expression form, Equation (513).

$$G(s) = \sum_{r=1}^n \left\{ \frac{R_r}{j\omega - p_r} + \frac{R_r^*}{j\omega - p_r^*} \right\} \quad (511)$$

where:

$p_r = -\sigma_r + j\omega_r$, pole location of the r^{th} mode

ω_r : modal frequency of the r^{th} mode

σ_r : half power point damping of the r^{th} mode

R_r : residues

* : complex conjugate representation

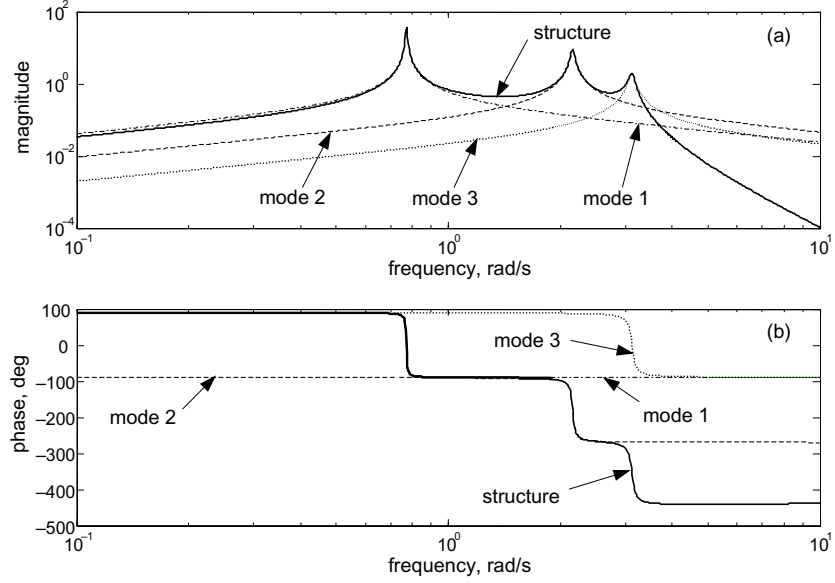


Figure 5.3: Representation of Structural Transfer Function [29].

This representation can be written in s-domain, as a pole-residue form which is the modal-parameter model as Equation (513).

$$G(s) = \sum_{r=1}^n \left\{ \frac{R_r}{s - p_r} + \frac{R_r^*}{s - p_r^*} \right\} \quad (512)$$

Real structures are continuous system and they have an infinite number of poles. However, system identification tests are performed in the real test case within a specified frequency range. Also, the obtained response data is processed in bands of interest. Therefore, the estimation process can be divided into three range as lower out-of-band modes, in-band modes and upper out-of-band modes [34]. As a result, the modal-parameter model is extended to cover all the related structural characteristics in the Equation (513).

$$G(s) = \underbrace{R_L}_{Lower} + \underbrace{\sum \left\{ \frac{R_r}{s - p_r} + \frac{R_r^*}{s - p_r^*} \right\}}_{Modes} + \underbrace{R_U}_{Upper} \quad (513)$$

where:

R_L : Lower residuals

R_U : Upper residuals

5.1.1 Azimuth Axis

The transfer function of the azimuth axis was obtained in Chapter 4. The modal-parameter representation of this transfer function is expressed in Equation (514).

$$G(s) = \sum \left\{ \frac{1289 + 850.2j}{s - (-9.87 + 822.5j)} + \frac{1289 - 850.2j}{s - (-9.87 - 822.5j)} \right\} + \left\{ \frac{188.1 + 122.4j}{s - (-4.033 + 278.1j)} + \frac{188.1 - 122.4j}{s - (-4.033 - 278.1j)} \right\} + \left\{ \frac{-14.53 - 0.7863j}{s - (-3.936 + 157.4j)} + \frac{-14.53 + 0.7863j}{s - (-3.936 - 157.4j)} \right\} + 3.8533 \quad (514)$$

5.1.2 Elevation Axis

The transfer function of the elevation axis was obtained in Chapter 4. The modal-parameter representation of this transfer function is expressed in Equation (515).

$$G(s) = \sum \left\{ \frac{-189 + 68.38j}{s - (-100.8 + 954.7j)} + \frac{-189 - 68.38j}{s - (-100.8 - 954.7j)} \right\} + \left\{ \frac{-4.25 + 225.5j}{s - (-6.785 + 276.9j)} + \frac{-4.25 - 225.5j}{s - (-6.785 - 276.9j)} \right\} + 2.8135 \quad (515)$$

CHAPTER 6

CONTROLLER DESIGN AND SIMULATION

In this section control principle, requirements and the control problem are analyzed. Controllers are designed, developed and simulated for each axis. All the works are done in MATLAB. The nonlinear mathematical model of gimbal axes is linearized around an operating point. Then the transfer function of each axis is estimated in the continuous time domain in Chapter 4.

The control scenario is used to steer and stabilize the LOS of AGS. There exists disturbance due to ship movements because of waves. Also, the translatory motion of the ship can cause disturbances. However, it sails slowly and its position change with respect to distance from the satellite is insignificant. Therefore, disturbances caused by waves are more important than translatory motion. The controller is designed and developed mainly to attenuate these disturbances.

Azimuth and elevation axis of the AGS are uncoupled and have independent movements. Hence, the control systems of each axis are also independent. Therefore, controller design for each axis is considered only for itself.

6.1 Controller Structure

Controllers are chosen depending on performance requirements of the system, disturbance attenuation and design process. There are different controller structure types. Proportional-integral-derivative (PID), proportional-integral (PI), linear quadratic regulator (LQR) and robust controllers are examples of them. In this study, disturbances due to the ship movements are in low frequency. Therefore, optimum controller per-

formance should be enough to overcome this disturbance. Mathematical expression of the controller terms:

Open loop transfer function $T_f(s) = G(s)C(s)$

Closed loop transfer function $T_f(s) = \frac{G(s)C(s)}{1+G(s)C(s)}$

G : plant, estimated transfer function

C : controller

6.1.1 PI Controller

Proportional-and-integral (PI) type controller is used. PI controller is reliable and has a simple structure with the implementation process details. Also, it is engineering cost-effective. General form of its transfer function is expressed in Equation (61). The error term in the feedback loop is integrated and scaled by gain factors. There are different implementation form of this structure.

$$C = k_p + \frac{k_i}{s} \quad (61)$$

k_p : proportional gain

k_i : integral gain

Open and closed-loop system transfer function can be written as Equation (62) and Equation (63). Open loop system transfer function

$$T_f(s) = G(s)\left(\frac{k_p s + k_i}{s}\right) \quad (62)$$

Closed loop system transfer function

$$T_f(s) = \frac{G(s)(k_p s + k_i)}{s + G(s)(k_p s + k_i)} \quad (63)$$

6.1.2 PI Controller Tuning Procedure

There are two gains in PI controller structure as mentioned before. These gains affect system performance characteristics. Open and closed-loop system performance

can be adjusted and optimized by proper selection of these gains. Firstly, the proportional gain is chosen. Let's start with how the change of proportional gain affects the response.

With the increase of k_p :

- Disturbance rejection properties improve
- System bandwidth increase
- Impact of disturbances increases on the system acceleration
- Impact of command increases on the system acceleration

It can be seen that increase of k_p results in better system performance. On the other hand, system acceleration increases because of command and disturbances at high frequencies. That means the system can reach the acceleration limit and its performance becomes worse, possibly the system becomes unstable. As a result, optimum k_p should be chosen.

Secondly, the integral gain is criticized. High k_i value can cause oscillations of system closed-loop. However, disturbance rejection properties are improved with the increase of k_i .

As a result, start the tuning procedure with k_p value. It is increased until the system reaches acceleration limits under expected disturbances and operation commands. The k_p is set to 75% of this value. After that, the k_i value is optimized. It is increased until oscillations or undershoot monitored and then set it to 75% of this value [35].

6.1.3 Filter Design

The performance of the system is directly related to controller tuning. However, there are physical limits of servo drivers and mechanical structures. It can be named mechanical stiffness. The stiffer the system, the more improved the performance. It results in resonance and anti-resonance frequencies. Mechanical resonance is the main limit to the performance of the controller system. This is mainly low for complex

assemblies due to the combination of different stiffness characteristics. Therefore, there are different filters used with the controller structure. The aim of this filter is not to excite flexible modes of the system [36]. In this work, structural notch filters are used. General form of this filter can be written as Equation (64).

$$G_{filter} = \frac{s^2 + 2\zeta_1 w_N s + w_N^2}{s^2 + 2\zeta_2 w_N s + w_N^2} \quad (64)$$

w_N : notch filter frequency (Hz)

ζ_1, ζ_2 : damping ratios

w_N is chosen depending on resonance frequency. ζ_1/ζ_2 damping ratio is used to adjust the depth of the notch filter. These are chosen according to objective measures of performance.

6.2 Tuning of Controllers

The controller structure, tuning procedure and filters are explained with details. In this part, controllers are analyzed with different gain parameters. These are chosen from slow to fast controller responses up to the edge of unstable ones. Details of the parameters are given and step responses are plotted. After that gain and phase margin, crossover frequencies and bandwidth of the system are considered to optimize the controller gains and one set of the parameters is chosen.

6.2.1 Azimuth Axis

PI controller gains are optimized by using the specified performance criteria. The following parameters set by using the project requirements and the general controller design approach for a good response.

Gain Margin > 8 dB

Phase Margin > 45°

Bandwidth > 10 Hz, closed-loop @ -3 dB crossover

Table 6.1: Azimuth Axis Controller

Notch Filters	w_N (Hz)	ζ_1	ζ_2
G_{notch1}	25.3	0.03	0.15
G_{notch2}	44.25	0.015	0.5
G_{notch3}	130.9	0.012	0.85

Controller	k_p	k_i
C_{PI}	1238.6	741.3

Table 6.2: Azimuth Axis Controller Performance Parameter

Controller	Gain Margin (dB)	Phase Margin (deg)	Bandwidth (Hz)
C_{PI}	10.3	65.8	14

There exist structural resonances in the system. Three of the most dominant resonance frequencies are chosen and three notch filters are designed to attenuate structural resonances. Filter parameters are expressed in Table 6.1. The optimum k_p and k_i gains are chosen in accordance with the specified performance parameters. Tuned controller parameters are shown in Table 6.1 and the performance metrics are represented in Table 6.2. Open-loop frequency response of the this controller is represented with Figure 6.1. Also, the closed-loop frequency response is given in Figure 6.2. After all, step response of the closed-loop can be found in Figure 6.3. Controller performance parameters show that performance requirements are satisfied.

6.2.2 Elevation Axis

PI controller gains are optimized by using the specified performance criteria. The following parameters set by using the project requirements and the general controller design approach for a good response.

Gain Margin > 8 dB

Phase Margin > 45°

Bandwidth > 10 Hz, closed-loop @ -3 dB crossover

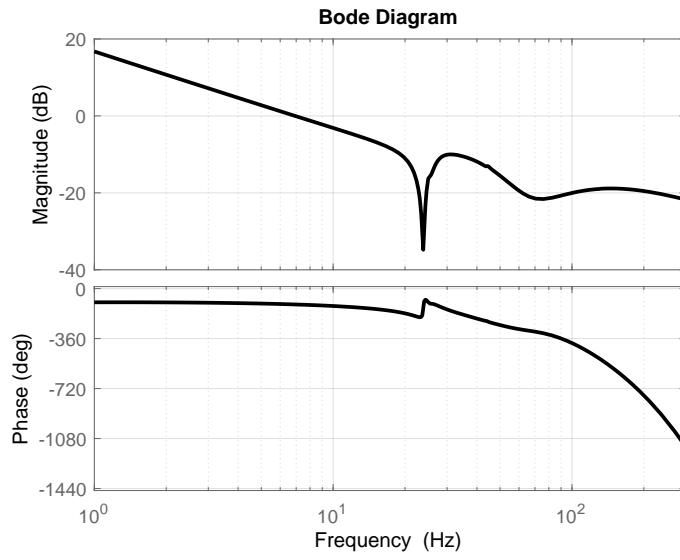


Figure 6.1: Azimuth Axis Open-Loop Bode Diagram

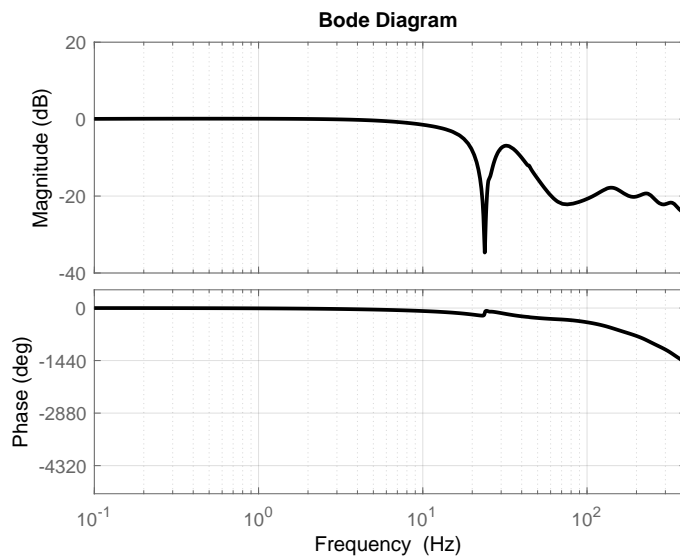


Figure 6.2: Azimuth Axis Closed-Loop Bode Diagram

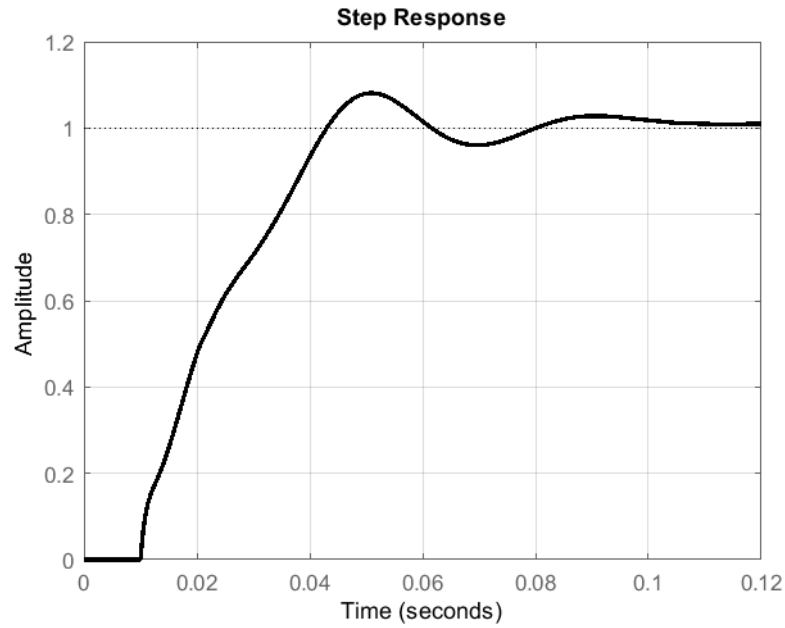


Figure 6.3: Azimuth Axis Step Response

There is one structural resonance in the system. Frequency of the peak resonance is chosen and one notch filter is designed to attenuate structural resonance. Filter parameters are expressed in Table 6.3.

Table 6.3: Elevation Axis Controller

Notch Filters	w_N (Hz)	ζ_1	ζ_2
G_{notch1}	44	0.0431	0.95
Controller	k_p	k_i	
C_{PI}	458.4	243	

The optimum k_p and k_i gains are chosen in accordance with the specified performance parameters. Tuned controller parameters are shown in Table 6.3 and the performance metrics are presented in Table 6.4. Open-loop frequency response of the this controller is represented with Figure 6.4. Also, closed-loop frequency response is given in Figure 6.5. After all, step response of the closed-loop can be found in Figure 6.6. Controller performance parameters show that performance requirements are satisfied

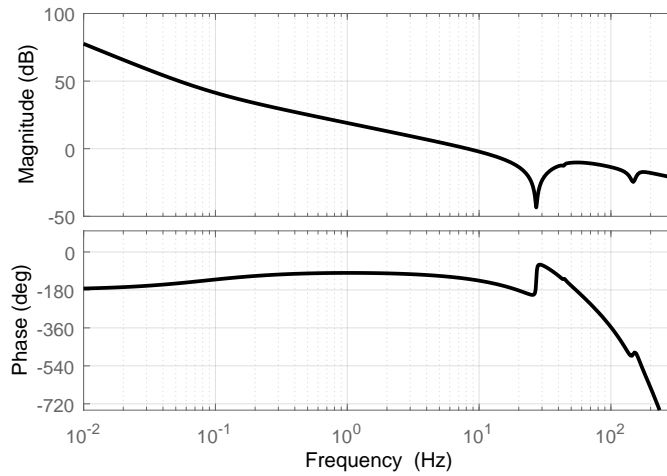


Figure 6.4: Elevation Axis Open-Loop Bode Diagram

and the designed controller is appropriate.

Table 6.4: Elevation Axis Controller Performance Parameter

Controller	Gain Margin (dB)	Phase Margin (deg)	Bandwidth (Hz)
C_{PI}	10.2	52.3	15

6.3 LOS Stabilization Simulation

LOS stabilization simulation is performed. There are specified disturbance waves as the project design requirements. These are used as platform motion inputs.

The following assumptions are specified for simulations conditions:

- Stick-slip friction problem results in degradation on the stabilization performance. However, it is not included in simulations. Kinematic-coupling which was explained in Chapter 3 is considered effective than this friction. Therefore, roll disturbance simulation is only done.

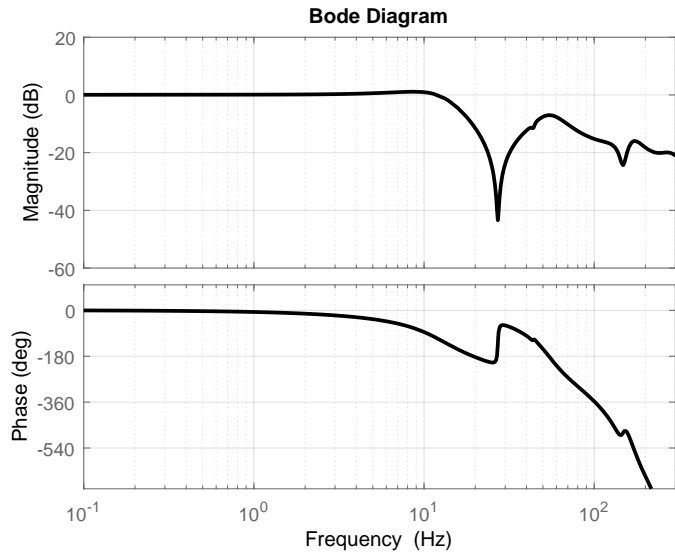


Figure 6.5: Elevation Axis Closed-Loop Bode Diagram

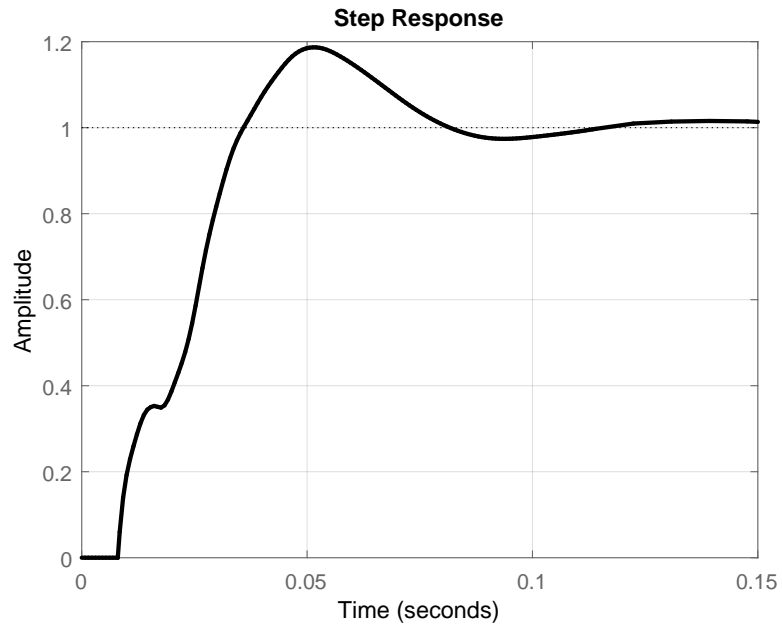


Figure 6.6: Elevation Axis Step Response

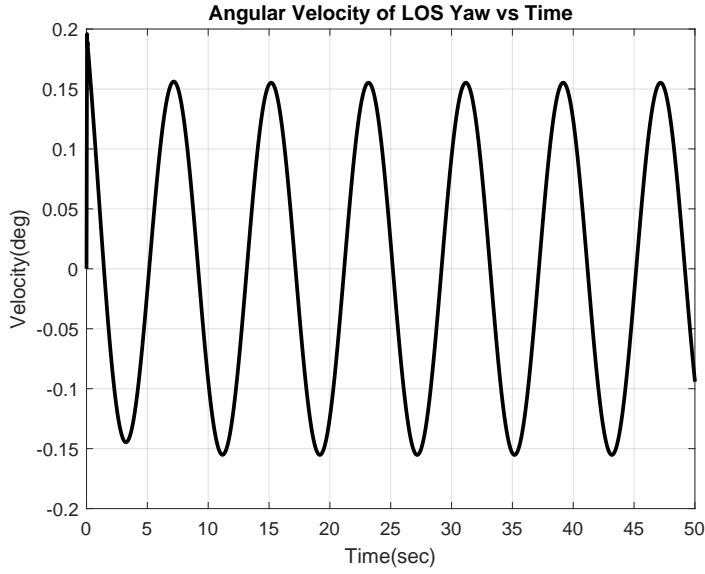


Figure 6.7: LOS Simulation Case-1, Yaw Angular Velocity

- LOS pitch axis is mass stabilized as specified so that simulation results are shown only for the LOS yaw axis
- Elevation axis initial position is chosen as 45° to increase the effect of kinematic coupling
- Azimuth axis initial position is chosen as 0° to not shift roll and pitch axes

Details of the roll disturbance applied to the AGS are given in Table 6.5.

Table 6.5: LOS Stabilization Disturbance Details

Case no	Wave Values		Axis of Disturbance
	Amp.(deg)	Period(sec)	
1	15	8	Roll

Case-1 is simulated with the specified disturbance. The simulation result is given in Figure 6.7. The given disturbance is attenuated.

CHAPTER 7

POINTING SCHEME

System components and operation strategies are mentioned in the previous chapters. In this chapter, operational details are explained. Open and closed-loop pointing methods work together to direct AGS and start communication. There are mainly three initial steps of starting communication through a satellite. Firstly, antenna gimbal performs blind pointing to the expected position of the satellite. Secondly, the acquisition state starts. The modem unit starts to receive procedure and tries to get the beacon signal from satellite. If the beacon signal level is above the predefined threshold, then the tracking algorithm starts and the beacon signal is used to reduce the blind pointing error. Finally, the AGS is tracking and locked to the satellite. Also, link maintenance is done to transmit/receive (Tx/Rx) operation. A detailed flow chart of this working principle can be seen in Figure 7.1. Beacon level is checked always to ensure good Tx/Rx operation. In case of beacon level drops or antenna lost satellite coverage, then process started from the beginning with open-loop pointing.

7.1 Antenna Gain Pattern

High bandwidth communication is important in SATCOM applications. The performance of this type of antenna is related to its gain and this changes with the position of the LOS depending on the deflection from satellite position., directional antennas has a characteristic gain pattern. It changes depending on working frequency range and dimensional size. This can be seen from the following Figure 7.2. In this figure, the gain change of antenna is given with respect to the deflection of the LOS in one axis. Also, the antenna pattern change for two-axes deflection can be shown as

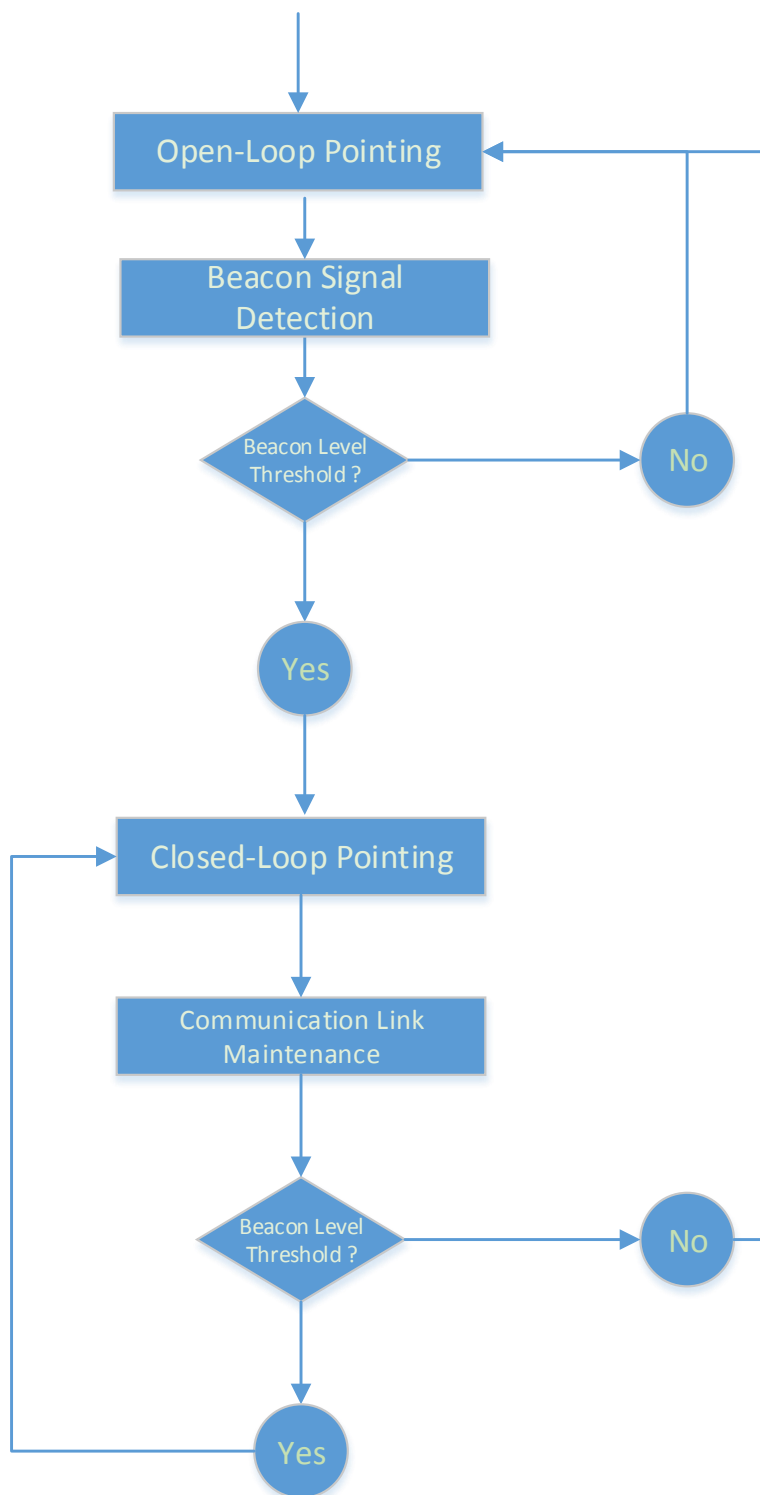


Figure 7.1: Operation Sequence of Antenna System

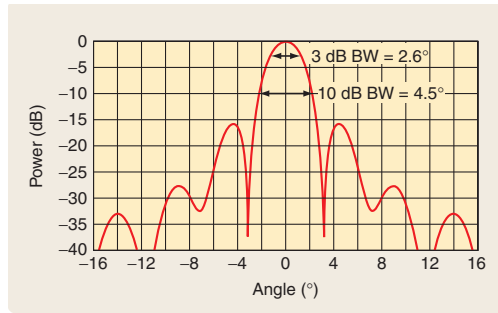


Figure 7.2: Antenna Gain Pattern for 0.5m Aperture Working at 14.5 GHz [1].

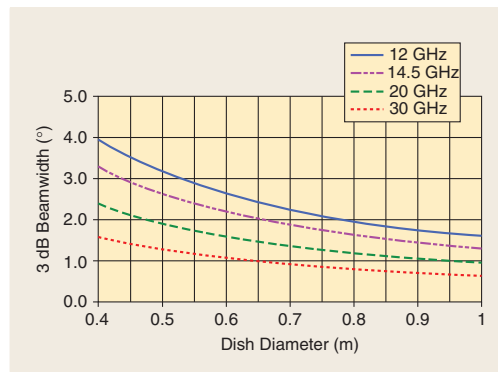


Figure 7.3: HPBW with Respect to Service Frequency and Antenna Size [1].

the following Figure 7.4. The antenna pattern has important characteristics that should be used for good communication. These are antenna's mainlobe, sidelobe and beamwidth. From the pattern graph, it can be seen that antenna reach maximum gain when LOS deflection from the satellite position is zero. The region between the first minimums of the pattern starting from the maximum gain position is the mainlobe. After this minima, gain starts to increase and makes another peak. This peak is called the sidelobe. Finally, 3 dB gain drop position at the pattern curve from maximum value is the beamwidth or Half-Power Beamwidth (HPBW). SATCOM antennas should be used within the HPBW region to provide high performance. Therefore, antenna beamwidth defines the maximum likelihood of pointing error and used to measure pointing performance [1]. HPBW of an antenna depends on aperture size and operating RF. The relation between these two factors can be seen as in Figure 7.3.

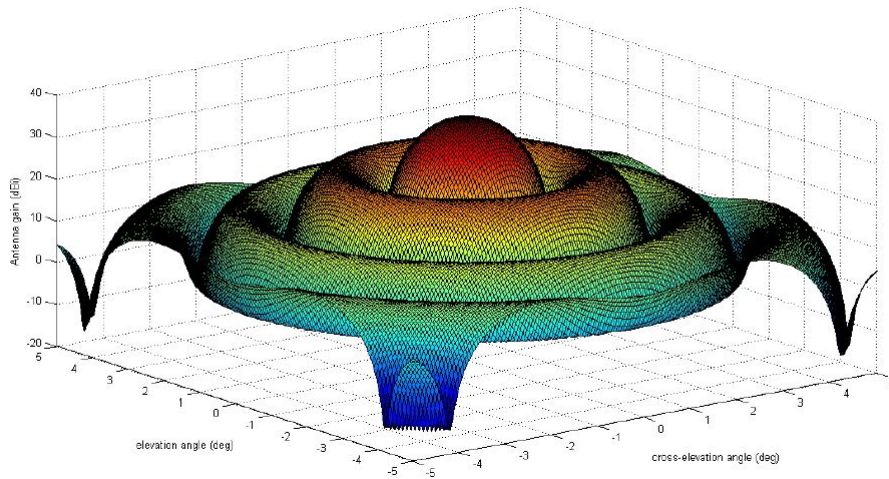


Figure 7.4: Antenna Gain Pattern [10].

7.2 Open-Loop Pointing

Open-loop pointing can be called blind pointing, antenna positioning or satellite acquisition. Antenna's LOS is directed to the expected satellite position. The main aim of this mode is to acquire the beacon signal. Coordinates of a geostationary satellite are fixed and it orbits around the earth. There is a GPS antenna on the AGS and coordinates of the satellite and the AGS is known. Open-loop pointing starts with calculation of pointing vector using coordinates.

Firstly, the pointing vector calculation is done using the kinematic relation between AGS and target satellite (TS) coordinates using Equation (71). However, the shape of the earth is important in this calculation due to the ellipticity of it. There are two steps of calculations.

$$r_{PointVector} = r_{TS} - r_{AGS} \quad (71)$$

Firstly, the geodetic coordinate of the TS and the AGS are transformed to Earth-Centered-Earth-Fixed (ECEF) cartesian coordinates. In the geodetic coordinate frame, location is expressed in terms of geodetic latitude, longitude and height Figure 7.5.

Explanation of the parameters and symbols used in coordinate frames and transformation can be given as:

ϕ, λ, h : Geodetic latitude, longitude, height

X, Y, Z : Earth-Centered-Earth-Fixed Cartesian Coordinates

a : semi-major earth axis(ellipsoid equatorial radius), $a = 6378137$

b : semi-minor earth axis(ellipsoid polar radius)

f : flattening parameter, $f = 1/298.257223563$

e^2 : Square of the ellipsoid eccentricity in closed form, $e^2 = 2f - f^2$

N : Principle radius of curvature in the prime vertical, $N(\lambda) = a/\sqrt{1 - e^2 \sin^2(\phi)}$

The geodetic coordinate of the TS and AGS can be transformed to the ECEF cartesian coordinates using Equation (72). This is a transformation from polar coordinates to cartesian coordinates. Coordinate frames are represented in Figure 7.5.

$$X = (N + h)\cos(\phi)\cos(\lambda) \quad (72a)$$

$$Y = (N + h)\cos(\phi)\sin(\lambda) \quad (72b)$$

$$Z = (N(1 - e^2) + h)\sin\lambda \quad (72c)$$

After obtaining the positions of the AGS and TS in the ECEF coordinates, the pointing vector can be obtained using Equation (73).

$${}^r_{PointVector} = \begin{bmatrix} X \\ Y \\ Z \end{bmatrix}_{ECEF} = \begin{bmatrix} X_{sat} \\ Y_{sat} \\ Z_{sat} \end{bmatrix}_{ECEF} - \begin{bmatrix} X_{ant} \\ Y_{ant} \\ Z_{ant} \end{bmatrix}_{ECEF} \quad (73)$$

Secondly, the pointing vector is transformed from ECEF coordinates to local North-East-Down (NED) coordinates using Equation (74). Transformation is done using Euler's transform matrices Equation (31).

$${}^r_{PointVector, NED} = E_y(\phi)E_z(\lambda){}^r_{PointVector, ECEF} \quad (74)$$

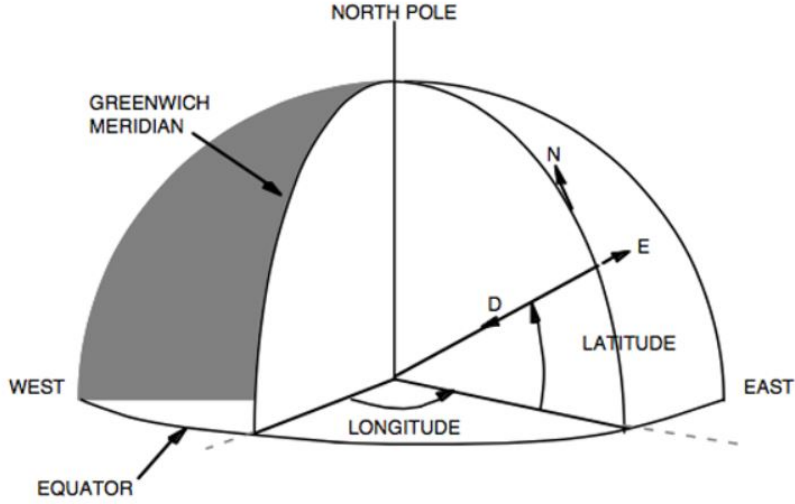


Figure 7.5: Coordinates Frame Representation [37].

This pointing vector can be used for a stationary point on the earth. On the other hand, the AGS is mounted to the ship and there are disturbances due to waves. Therefore, the coordinate frame of the AGS changes with the roll, pitch and yaw disturbances of the ship. Transformation calculation is done as in Equation (75). Roll, pitch and yaw disturbances of the host vehicle are measured by means of IMU sensor.

$$r_{PointVectorHostVehicle,NED} = E_x(roll)E_y(pitch)E_z(yaw)r_{PointVector,NED} \quad (75)$$

$$AzimuthAngleDmnd = atan2(Y_{NED}, X_{NED}) \quad (76)$$

$$ElevationAngleDmnd = atan2(-Z_{NED}, (X_{NED} \cos(AzimuthAngleDmnd) + Y_{NED} \sin(AzimuthAngleDmnd))) \quad (77)$$

As a result, the calculation of the satellite look angle in terms of the azimuth and elevation angles for the AGS mounted on to the host vehicle is introduced in Equation (76) and Equation (77). These angles can be represented in local coordinate as Figure 7.6.

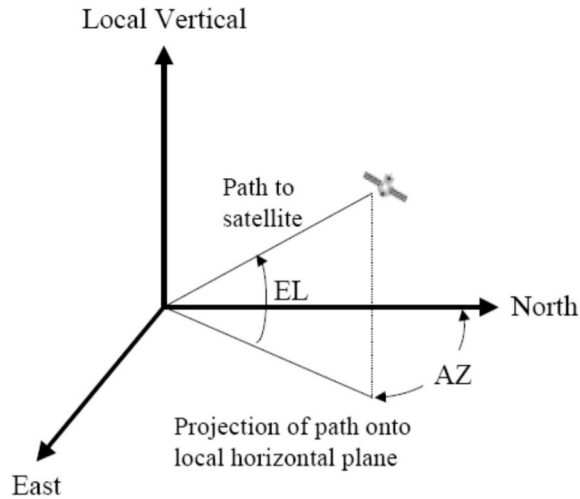


Figure 7.6: Satellite Look Angle Representation.

7.3 Closed-Loop Pointing

In this section, closed-loop pointing methods are explained, developed and simulated. After the open-loop pointing, there exists deviation from the target satellite location due to the reasons explained before. The main aim of this feedback loop is to compensate for and reduce these errors. Actually, this is not an usual feedback-loop. In this loop, the error is not generated by the motion controller. It is generated by tracking or scanning controller. That means, this tracker acts like feedback and also command generator. Special maximization algorithms for SATCOM on-the-move antenna systems are used as mentioned in the literature chapter. They calculate correction angles using the RSS and then feed to each axis's rate loop respectively. The block diagram of closed-loop pointing over rate-loop can be shown in Figure 7.7.

7.3.1 Cost Function

The RSS or beacon signal is used as feedback for this closed-loop controller. The signal pattern and characteristics are mentioned in Section 7.1. Our problem is the maximization of this signal value. Power can be maximized by reducing LOS error which is ε_i .

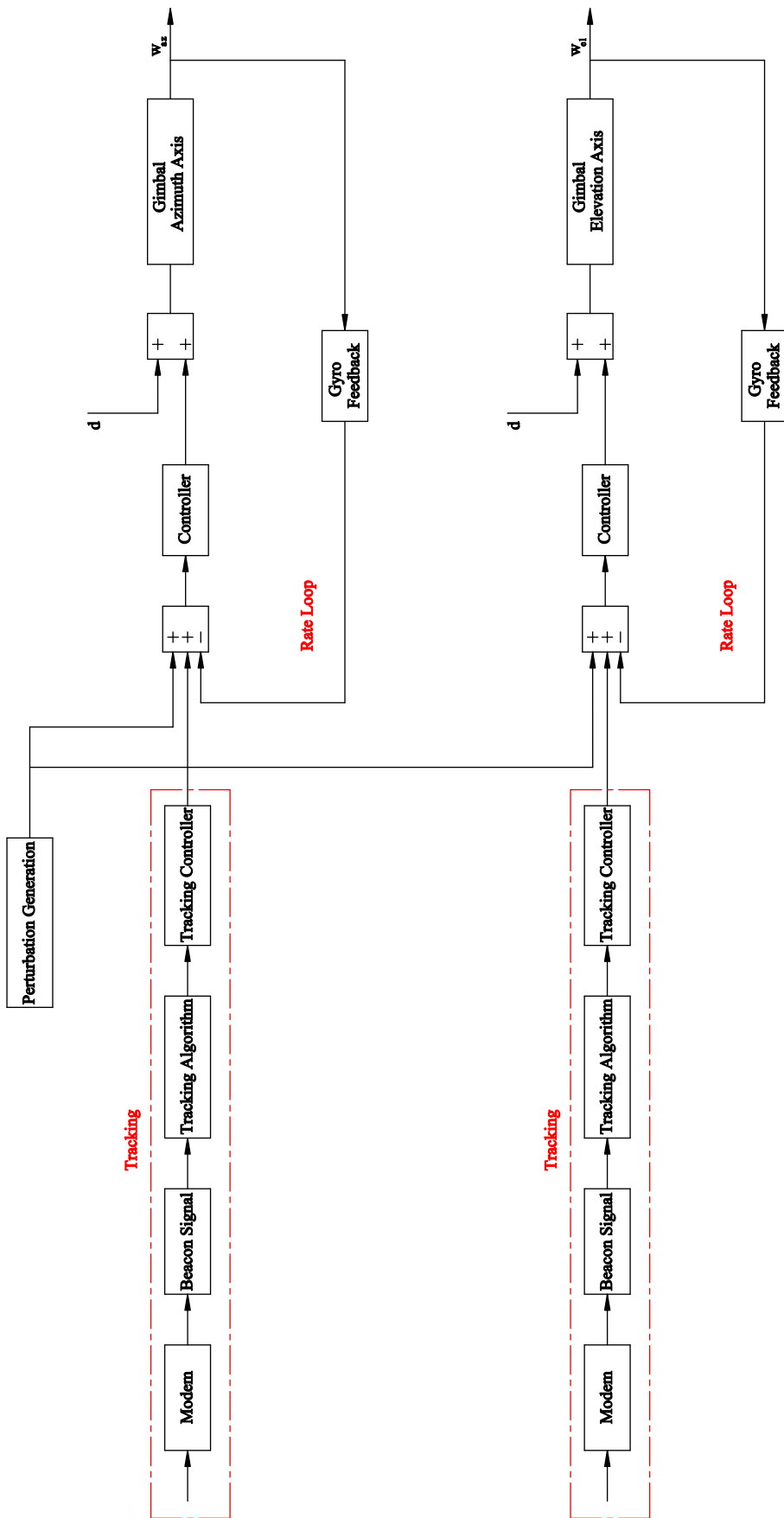


Figure 7.7: AGS Cascaded Tracker-Loop and Rate-Loop Representation

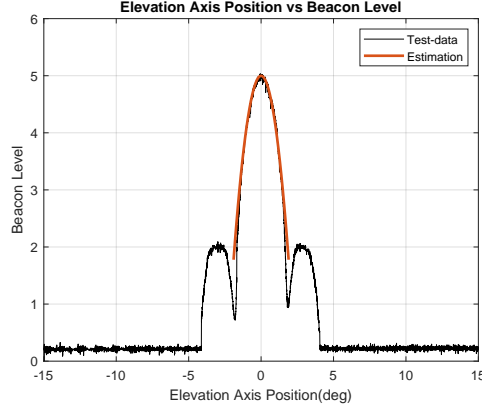


Figure 7.8: Power Change with Respect to Elevation Axis Position

The LOS RMS error can be expressed in terms of azimuth and elevation angle of AGS as the following;

$$\varepsilon_i = \sqrt{\Delta az^2 + \Delta el^2} \quad (78)$$

Δaz : Azimuth axis error from the target satellite

Δel : Elevation axis error from the target satellite

Received beacon signal strength is converted to analog voltage level by the modem (Figure 2.5) which is 0-5 volt range. That means, we need to concern the antenna pattern and voltage level. Also, our interest is the mainlobe region as mentioned in the previous section. Therefore we are focusing on that. Antenna pattern can be obtained from the real system for simulation. The simulation is performed as follows: LOS is mispointed deliberately only in the elevation axis. Then, the elevation axis is moved with a constant velocity. Beacon level and the axis position is logged during this motion. The beacon level change with respect to the elevation axis position is plotted in Figure 7.8. The signal starts with noise level, then sidelobe, finally reaches to mainlobe and then maximum level as position error is decreased. Using this signal pattern, the power equation can be estimated as Equation (79).

$$p = 5 \left(1 - \frac{\varepsilon_i^2}{5.6} \right) + noise \quad (79)$$

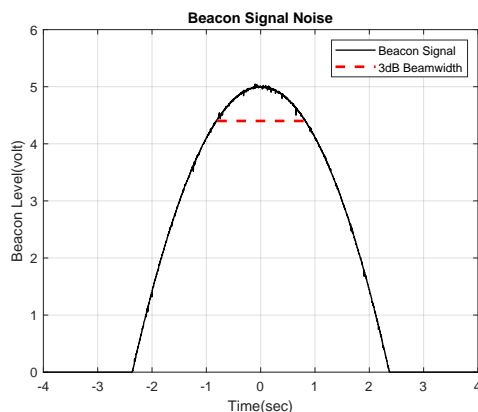


Figure 7.9: Cost Function with Respect to Elevation Axis Position and 3dB Beamwidth

Antenna 3dB beamwidth is shown in Figure 7.9 and also obtained as Equation (710):

$$Beamwidth = 1.6^\circ @ - 3 \text{ dB} \quad (710)$$

The beamwidth defines the maximum LOS error to continue high-bandwidth communication. The communication link is lost above this LOS error because this is the threshold limit. Moreover, the main concern is to hold LOS within the 3dB beamwidth region. The beacon signal has a noise due to received signal noise and analog to digital converter of the modem unit. The beacon signal is logged from real system when LOS is pointed to the satellite directly and with no disturbance on the platform to simulate real case noise. This can be seen in Figure 7.9. Obtained noise is added to power function and it is plotted in Figure 7.9. Moreover, the beacon signal has a sampling frequency of $\frac{1}{40}$ Hz. This is also included to cost function model.

In the following simulations and studies, the RSS generation is done virtually using the estimated power function Equation (79). The LOS RMS error which is Equation (78) used to calculated the RSS.

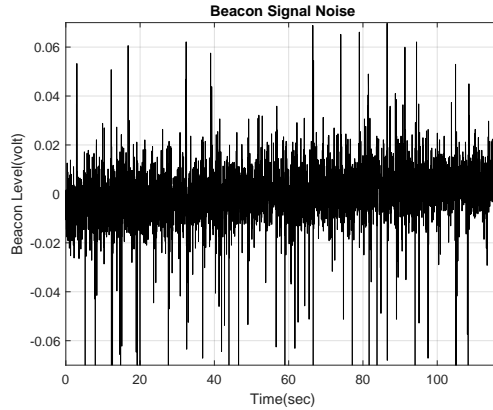


Figure 7.10: Beacon Signal Noise

7.3.2 Tracking Controller

The tracking controller is a P-type controller working over the rate loop for each axis. Detailed block diagram representation of the controller structure is given in Figure 7.11. The tuning of this controller is done by the experience of field tests.

7.3.3 Conical Scanning

In this method, the antenna is rotated in a circular pattern with an offset angle about the antenna's boresight axis. This offset angle is called squint angle or scan radius. This can be represented in Figure 7.12. The RSS is measured during this motion. The algorithm decides to depend upon the RSS to correct the boresight. When the radio source or spacecraft is on the boresight, the RSS is constant over the scanning cycle. If the antenna is off-boresight, there will be sinusoidal variation in RSS. Amplitude variation can be seen in Figure 7.13. Signal level increases as beam approaches to target position and falls off farther out. That means amplitude of variation is proportional with the angular distance of boresight from the target direction and this variation gives the angular compensation. The frequency of the sinusoidal variation is the same as conical scan frequency. On the other hand, the phase of the variation relative to the beam scanning position can change. The phase delay gives the direction information of the target.

The following abbreviations and relations are used in this method:

ω : frequency of the conical scanning motion

R : radius of the conical scanning motion

p : RSS, power Equation (79)

G : parametric gain to adjust the calculation

\bar{x} : Calculated Az-axis compensation, correction-offset

\bar{y} : Calculated El-axis compensation, correction-offset

$x_{PosPerturbation} = R\cos(\omega t)$: Az-axis position perturbation

$y_{PosPerturbation} = R\sin(\omega t)$: El-axis position perturbation

$x_{VelPerturbation} = -R\omega\sin(\omega t)$: Az-axis velocity perturbation

$y_{VelPerturbation} = R\omega\cos(\omega t)$: El-axis velocity perturbation

Circular pattern motion is performed with velocity perturbation waves. Position perturbations are used for compensation calculations.

Compensation calculation is done using Equation (711).

$$\bar{x}(t) = G \int p(t)x_{PosPerturbation}(\tau)d\tau \quad (711a)$$

$$\bar{y}(t) = G \int p(t)y_{PosPerturbation}(\tau)d\tau \quad (711b)$$

After obtaining compensation for each axis, it is used to steer the LOS towards TS.

LOS position of antenna can be obtained instantaneously with Equation (712).

$$x(t) = x_0 + R\cos(\omega t) \quad (712a)$$

$$y(t) = y_0 + R\sin(\omega t) \quad (712b)$$

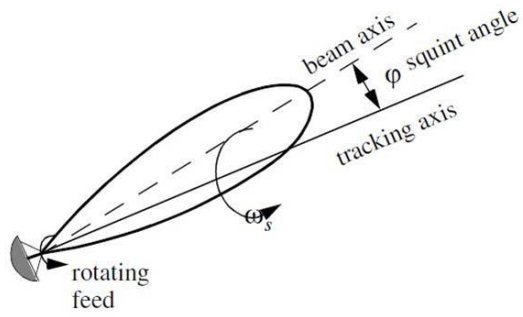


Figure 7.12: Conical Scan Pattern [38].

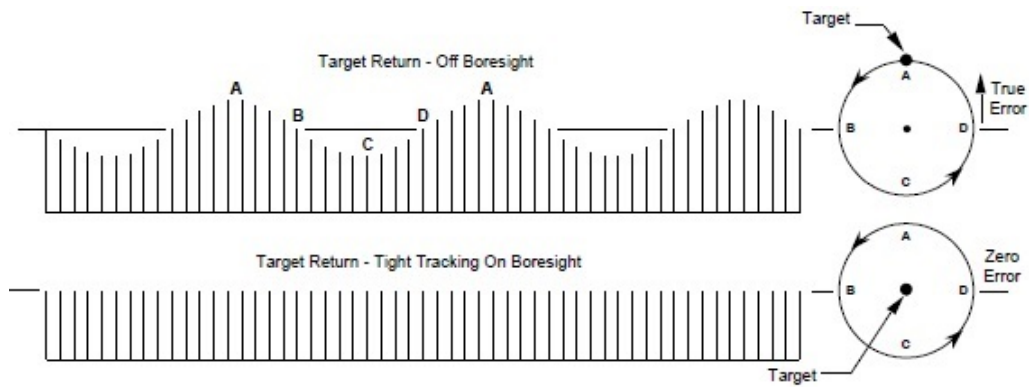


Figure 7.13: Amplitude Variation of the Received Signal [39].

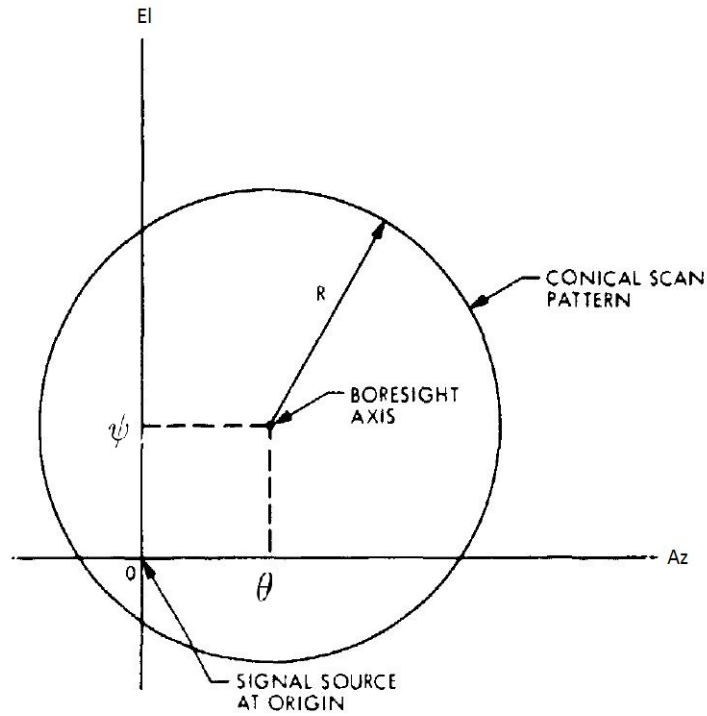


Figure 7.14: LOS Representation with Azimuth and Elevation Axes [11].

7.3.3.1 Effects of Scanning Parameters to Performance

Conical pattern shape is used to perturb the LOS to get signal level during scanning. Therefore, pattern size and period of motion are directly related to tracking performance. Two different comparison simulations are performed to see the effect of conical scanning parameters.

Simulation conditions are as follows:

- Azimuth axis offset from the target satellite location, $x_0 = 0.4$ deg
- Elevation axis offset from the target satellite location, $y_0 = 0.6$ deg
- Traditional conical scanning continuous version is used during simulations

Firstly, LOS is pointed with specified offsets and conical scanning is performed for different scanning radius. Details of the simulation cases are shown in Table 7.1. Simulations are done with different R . Signal levels are plotted in Figure 7.15.

Table 7.1: Simulation Parameter Table for Different R

Case no	R (deg)	ω (rad/s)
1	0.05	$\frac{\pi}{4}$
2	0.07	
3	0.1	
4	0.2	
5	0.3	
6	0.4	

Secondly, the same simulation is performed for different scanning frequencies. Details of the simulation cases are shown in Table 7.2. Simulations are done with different ω value. Simulation results are plotted in Figure 7.16.

Table 7.2: Simulation Parameter Table for Different ω

Case no	R (deg)	ω (rad/s)
1	0.4	$\frac{\pi}{2}$
2		$\frac{\pi}{3}$
3		$\frac{\pi}{4}$
4		$\frac{\pi}{5}$
5		$\frac{\pi}{6}$

As a result of these simulations, the followings are obtained:

- Max RSS increases with the decrease of R
- There exists even small oscillation with the increase of R
- RSS reaches steady-state quickly with the increase of R
- RSS reaches steady-state quickly with the decrease of ω
- RSS oscillation amplitude increase with the decrease of ω
- Max RSS does not effected by ω
- G is chosen as $G = \frac{\omega}{2\pi R^2}$

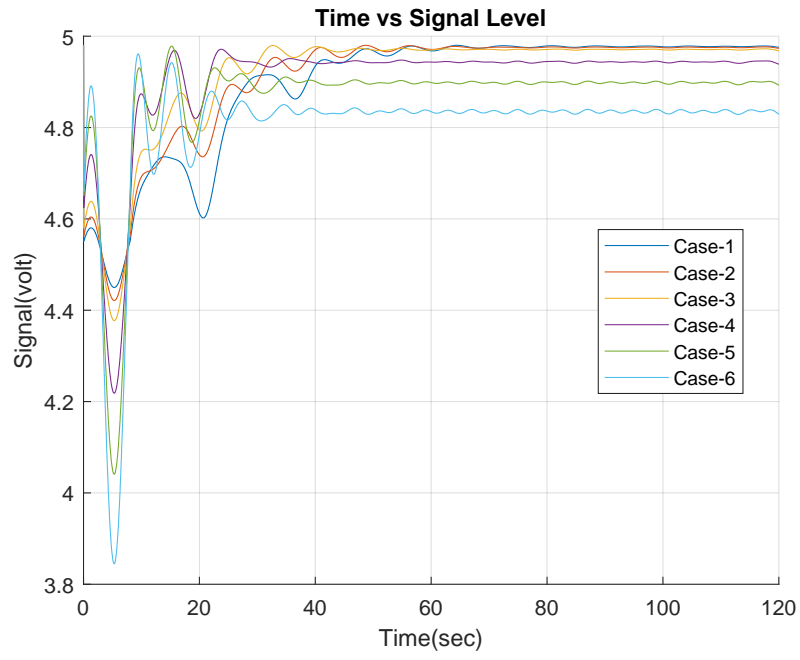


Figure 7.15: Simulation for Different R with $\omega = \frac{\pi}{4}$ (rad/s)

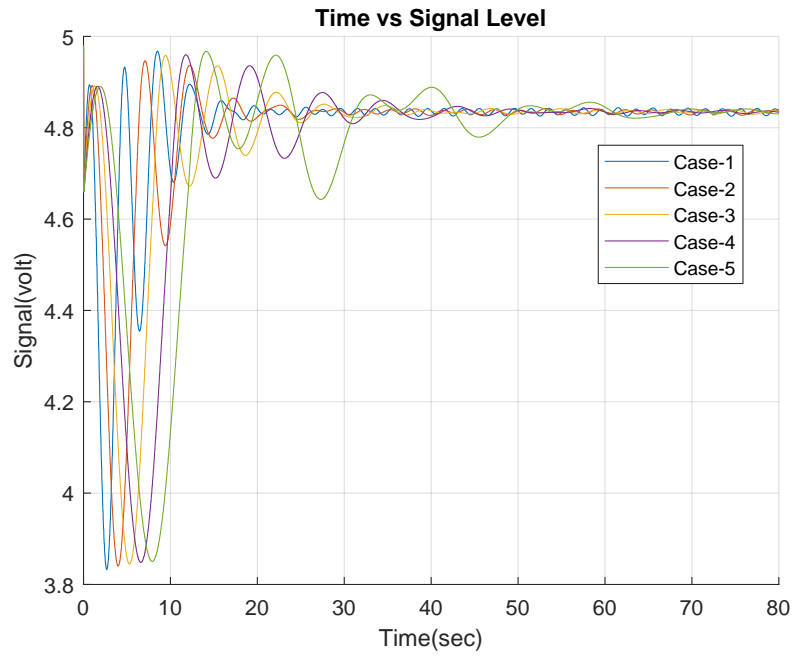


Figure 7.16: Simulation for Different ω with $R = 0.4$ (deg)

Table 7.3: CSAP Method Controller Gains

Controller	Azimuth	Elevation
K_p	11.5	11.5

Finally, the mean value of $R = 0.2$ deg seems appropriate. However, tracking loop tuning is more prone to the LOS error and stable tuning is hard to do with this value. Therefore, $R = 0.4$ deg and $\omega = \frac{\pi}{4}$ rad/s are chosen and they are used in the following sections.

The following assumptions are specified for simulations conditions:

- Elevation axis initial position is chosen as 45° to increase the effect of kinematic coupling
- Azimuth axis initial position is chosen as 0° to not shift the roll and pitch axes
- Sequence step which are given in Figure 7.1 when beacon level is less than threshold closed-loop to open-loop shift are not applied during simulations to check pure closed-loop performance

7.3.3.2 Conical Scanning, After One Period (CSAP)

This is the oldest and general application of the conical scanning technique. In this method, LOS position perturbation is convolved with the RSS over the scanning period. The offset angle is calculated subsequently and feed to the rate loop controller for each axis respectively. Offset calculations are done using the Equation (713).

$$\bar{x}(t) = G \int_0^{\frac{2\pi}{w}} p(t) x_{PosPerturbation}(\tau) d\tau \quad (713a)$$

$$\bar{y}(t) = G \int_0^{\frac{2\pi}{w}} p(t) y_{PosPerturbation}(\tau) d\tau \quad (713b)$$

Tracking controller gains are given in Table 7.3. In the following sections, different types of scenarios are developed and simulated. The main aim of these is to see the performance of the tracker under problematic cases.

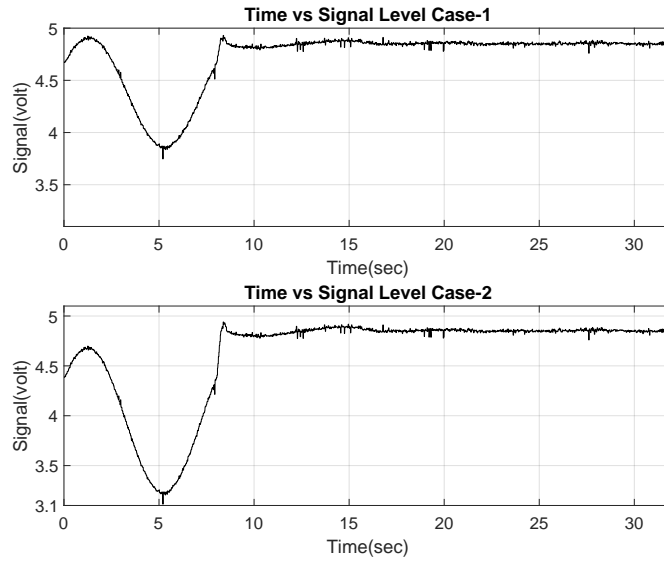


Figure 7.17: CSAP Method Simulation-1, Case-1 and Case-2

Simulations are conducted to simulate real case problems and these problems are overrated in several simulations. Firstly, LOS mispointing case is simulated.

Simulation-1

LOS is mispointed deliberately and scanning is performed for the different offsets. Simulation details are shown in Table 7.4.

Table 7.4: Simulation-1 Cases Table for Different Offsets

Case no	Azimuth offset (deg)	Elevation offset (deg)
1	0.4	0.6
2	0.6	0.8
3	0.8	1.0
4	1.0	1.2

The results of the simulations are presented in Figure 7.17 and Figure 7.18. Also, the parametric performance values are given in Table 7.5. It can be seen from the figure that calculated offsets are different for each case.

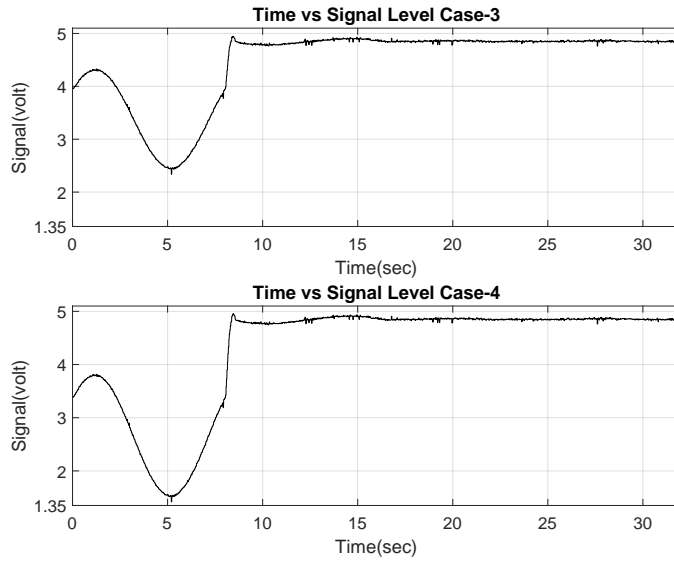


Figure 7.18: CSAP Method Simulation-1, Case-3 and Case-4

Table 7.5: CSAP Method Performance Parameter for Simulation-1

Simulation-1	Signal Level (volt)	Settling to Max RSS (sec)	Num. of Cycles
Case 1	4.85	8	1
Case 2	4.85	8	1
Case 3	4.85	8	1
Case 4	4.85	8	1

However, the RSS reaches the steady-state value after one cycle for all the cases.

Simulation-2

Gyro sensors drift error is simulated. The constant error value is added to the sensor reading. Details of the error are given in Table 7.6. Simulations are performed for two cases to see the effect of the tracking loop to the RSS. Firstly, the tracking loop is enabled and LOS is pointed to the satellite directly. Secondly, the tracking loop is disabled and LOS is pointed to the satellite directly.

Table 7.6: Simulation-2 Cases Table for Gyro Drift

Case no	Gyro Axes		Tracking
	X (deg/s)	Z (deg/s)	Statue
1	0.01	0.01	On
2	0.01	0.01	Off

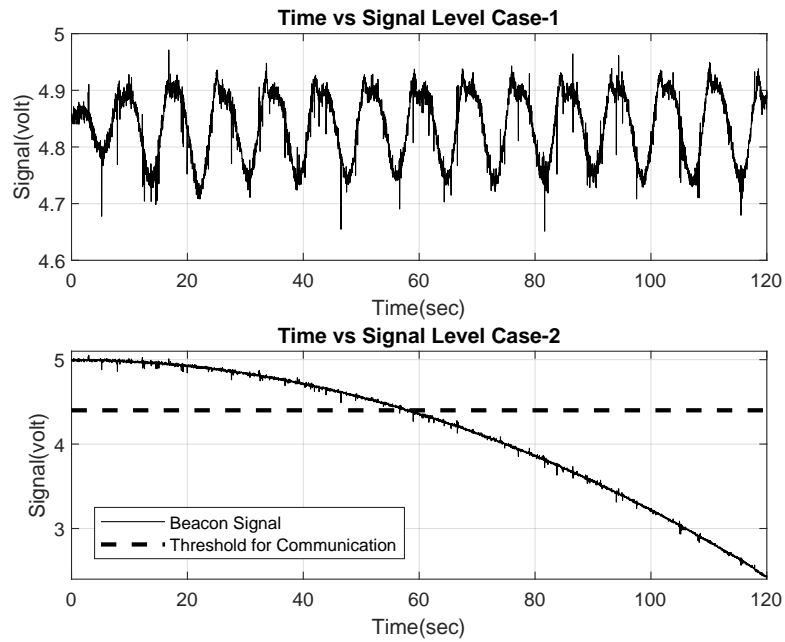


Figure 7.19: CSAP Method Simulation-2, Case-1 and Case-2

The results of the simulations are presented graphically in Figure 7.19. Also, the parametric performance values are given in Table 7.7. The tracking loop can compensate the gyro drift with less than 2% oscillation. This results in very small communication performance drop and it is still enough. On the other hand, it is the opposite of Case-2. LOS moves continuously in one direction even out of the satellite look area and communication is lost after the threshold level which is defined as 3 dB beamwidth. Therefore, the tracking loop is very effective to provide uninterpreted communication with the sensor drift error.

Table 7.7: CSAP Method Performance Parameter for Simulation-2

Simulation-2	Signal Level, Mean (volt)	Oscillation Rate (%)	Tracking
Case 1	4.83	1.81%	On
Case 2	Communication lost	-	Off

Simulation-3

Geosynchronous satellites drift is very small. These are mentioned in Chapter 1. However, this drift value is overrated to see the effect. The simulation details are given in Table 7.8.

Table 7.8: Simulation-3 Cases Table for Target Drift

Case no	Target Location Drift		Tracking
	Azimuth (deg/s)	Elevation (deg/s)	Statue
1	$\frac{2}{120}$	$\frac{2}{120}$	On
2	$\frac{2}{120}$	$\frac{2}{120}$	Off

Table 7.9: CSAP Method Performance Parameter for Simulation-3

Simulation-3	Signal Level, Mean (volt)	Oscillation Rate (%)	Tracking
Case 1	4.80	3.12%	On
Case 2	Communication lost	-	Off

The results of the simulations are presented graphically in Figure 7.20. Also, the parametric performance values are given in Table 7.9. The tracking loop can compensate gyro drift with less than 4% oscillation. This results in very small communication performance drop and it is still enough. On the other hand, this is the opposite of Case-2. LOS moves continuously in one direction even out of the satellite look area and communication is lost after the threshold level which is defined as 3 dB beamwidth.

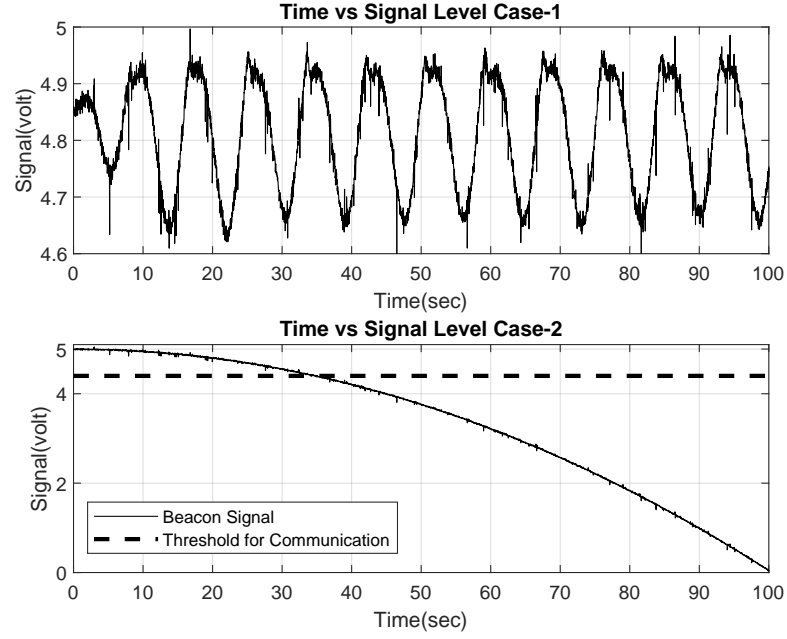


Figure 7.20: CSAP Method Simulation-3, Case-1 and Case-2

7.3.3.3 Conical Scanning, Continuously (CSC)

Conical scanning (CSC) method uses the LOS the position perturbation waves and the RSS in the same way with the previous method. On the other hand, the offset angle calculation is different. In this method, the offset angles are calculated and fed to the rate loop continuously instead at the end of every scanning period.

Offset calculations are done using the Equation (714).

$$\bar{x}(t) = G \int_{t-\frac{2\pi}{w}}^t p(t) x_{PosPerturbation}(\tau) d\tau \quad (714a)$$

$$\bar{y}(t) = G \int_{t-\frac{2\pi}{w}}^t p(t) y_{PosPerturbation}(\tau) d\tau \quad (714b)$$

Tracking controller gains are given in Table 7.10.

Simulations which are explained in previous section are performed.

Table 7.10: CSC Method Controller Gains

Controller	Azimuth	Elevation
K_p	0.9	0.9

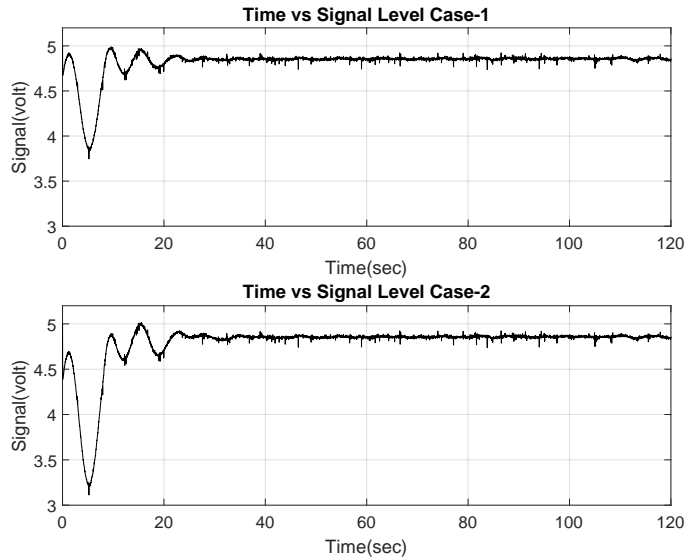


Figure 7.21: CSC Method Simulation-1, Case-1 and Case-2

Simulation-1

LOS is mispointed deliberately and scanning is performed for different offsets. The simulation details are shown in Table 7.4.

The results of the simulations are presented graphically in Figure 7.21 and Figure 7.22. Also, the parametric performance values are given in Table 7.5.

Settling time of the RSS and the number of cycles increases with the offset directly. However, the steady-state RSS value is the same for all cases.

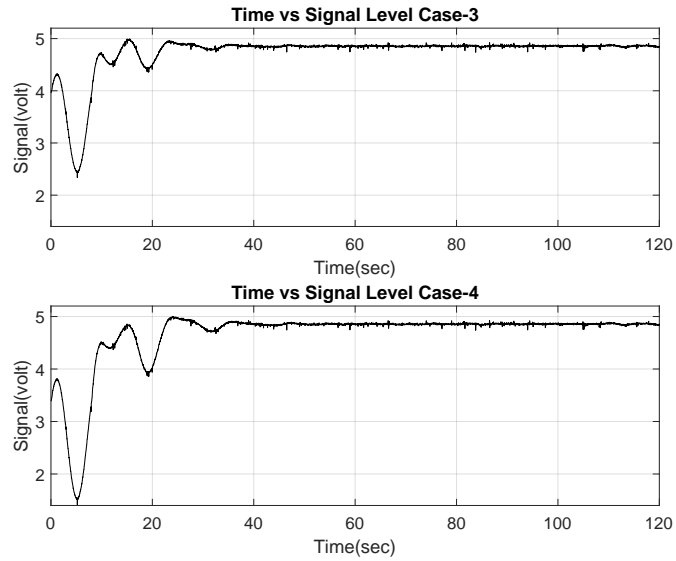


Figure 7.22: CSC Method Simulation-1, Case-3 and Case-4

Table 7.11: CSC Method Performance Parameter for Simulation-1

Simulation-1	Signal Level (volt)	Settling to Max RSS (sec)	Num. of Cycles
Case 1	4.85	24	3
Case 2	4.85	24	3
Case 3	4.85	32	4
Case 4	4.85	32	4

Simulation-2

Gyro sensors drift error is simulated. Details of the error are given in Table 7.6.

The results of the simulations are presented graphically in Figure 7.23. Also, the parametric performance values are given in Table 7.12. The tracking loop can compensate the gyro drift with less than 2% oscillation. This results in very small communication performance drop and it is still enough. On the other hand, this is the opposite of Case-2. LOS moves continuously in one direction even out of the satellite look area and communication is lost after the threshold level which is defined as 3 dB beamwidth. Therefore, the tracking loop is very effective for the sensor drift error.

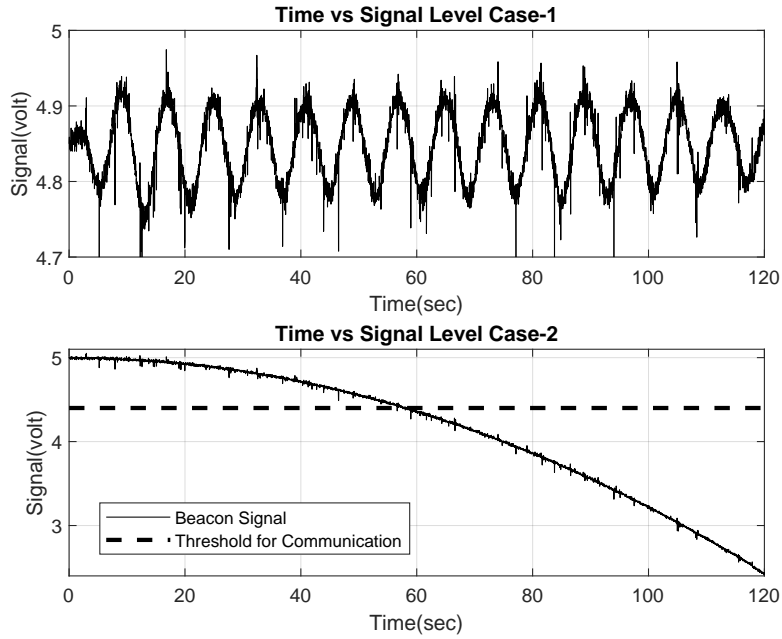


Figure 7.23: CSC Method Simulation-2, Case-1 and Case-2

Table 7.12: CSC Method Performance Parameter for Simulation-2

Simulation-2	Signal Level, Mean (volt)	Oscillation Rate (%)	Tracking
Case 1	4.85	1.55%	On
Case 2	Communication lost	-	Off

Simulation-3

Target satellite drift is simulated. Simulation details are given in Table 7.8.

The results of the simulations are presented graphically in Figure 7.24. Also, the parametric performance values are given in Table 7.13. The tracking loop can compensate the target drift with less than 4% oscillation. This results in very small communication performance drop and it is still enough. On the other hand, this is the opposite of Case-2. LOS moves continuously in one direction even out of the satellite look area and communication is lost after the threshold level which is defined as 3 dB beamwidth.

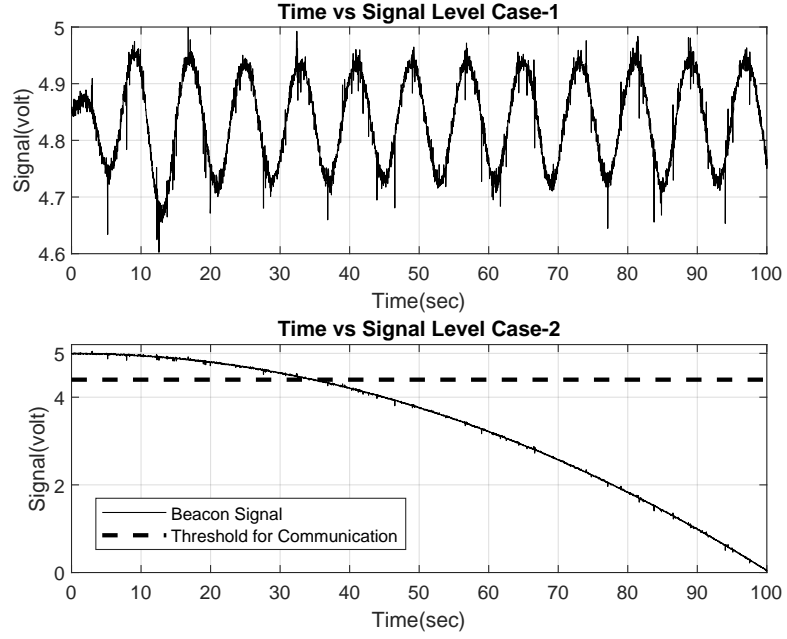


Figure 7.24: CSC Method Simulation-3, Case-1 and Case-2

Table 7.13: CSC Method Performance Parameter for Simulation-3

Simulation-3	Signal Level, Mean (volt)	Oscillation Rate (%)	Tracking
Case 1	4.83	2.1%	On
Case 2	Not stable	-	Off

7.3.3.4 Predicted Gradient Conical Scanning (PGCS)

In this method, the position perturbation is changed with the velocity and derivative of the RSS is used. The velocity perturbation is convolved with the derivative of the RSS and offset angles are calculated and then feed to the rate loop continuously for each axis respectively. Offset calculations are done using the Equation (715). Tracking controller gains are given in Table 7.14.

$$\bar{x}(t) = G \int_{t-\frac{2\pi}{w}}^t \frac{d}{d\tau}[p(t)] \frac{d}{d\tau}[x_{PosPerturbation}(\tau)] d\tau \quad (715a)$$

$$\bar{y}(t) = G \int_{t-\frac{2\pi}{w}}^t \frac{d}{d\tau}[p(t)] \frac{d}{d\tau}[y_{PosPerturbation}(\tau)] d\tau \quad (715b)$$

Table 7.14: PGCS Method Controller Gains

Controller	Azimuth	Elevation
K_p	3	3

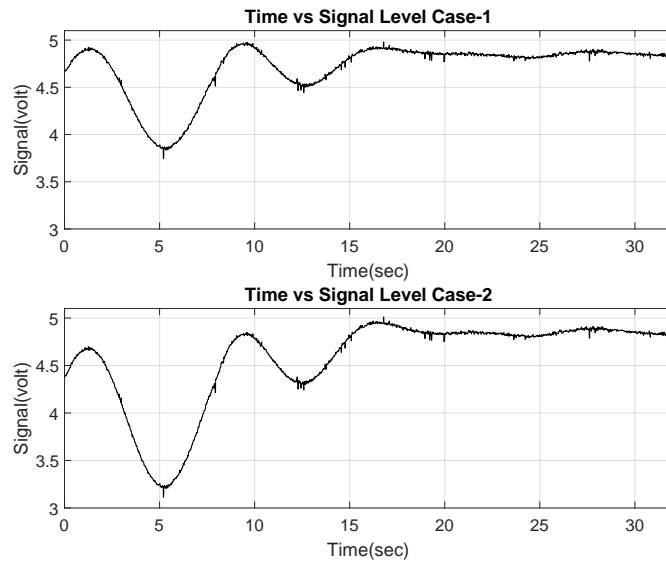


Figure 7.25: PGCS Method Simulation-1, Case-1 and Case-2

Simulation-1

LOS is mispointed deliberately and scanning is performed for different offsets. Simulation details are shown in Table 7.4.

The results of the simulations are presented graphically in Figure 7.25 and Figure 7.26. Also, the parametric performance values are given in Table 7.15. The RSS reaches steady-state value after two cycles for all cases. Response is fast but there exist oscillations before settling.

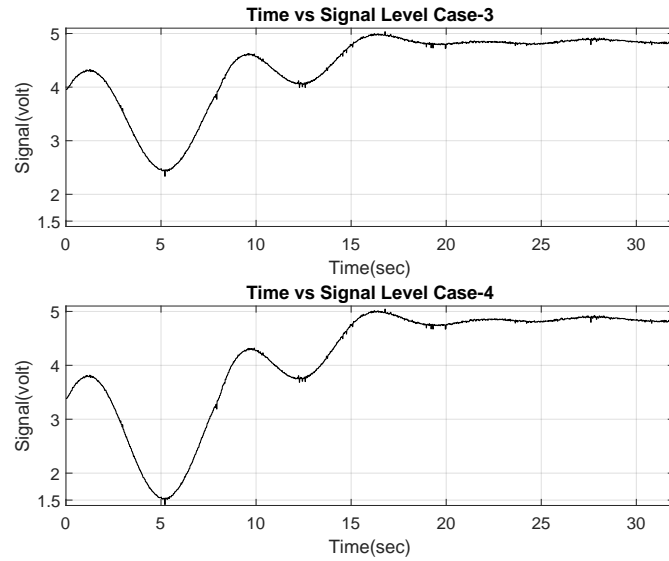


Figure 7.26: PGCS Method Simulation-1, Case-3 and Case-4

Table 7.15: PGCS Method Performance Parameter for Simulation-1

Simulation-1	Signal Level (volt)	Settling to Max RSS (sec)	Num. of Cycles
Case 1	4.85	16	2
Case 2	4.85	16	2
Case 3	4.85	16	2
Case 4	4.85	16	2

Simulation-2

Gyro sensors drift error is simulated. Details of the error are given in Table 7.6

The results of the simulations are presented graphically in Figure 7.27. Also, the parametric performance values are given in Table 7.16. The tracking loop can compensate for the gyro drift with less than 2% oscillation. This results in very small communication performance drop and it is still enough. On the other hand, this is the opposite of Case-2. LOS moves continuously in one direction even out of the satellite and communication is lost after the threshold level which is defined as 3 dB beamwidth. Therefore, the tracking loop is very effective for the sensor drift error.

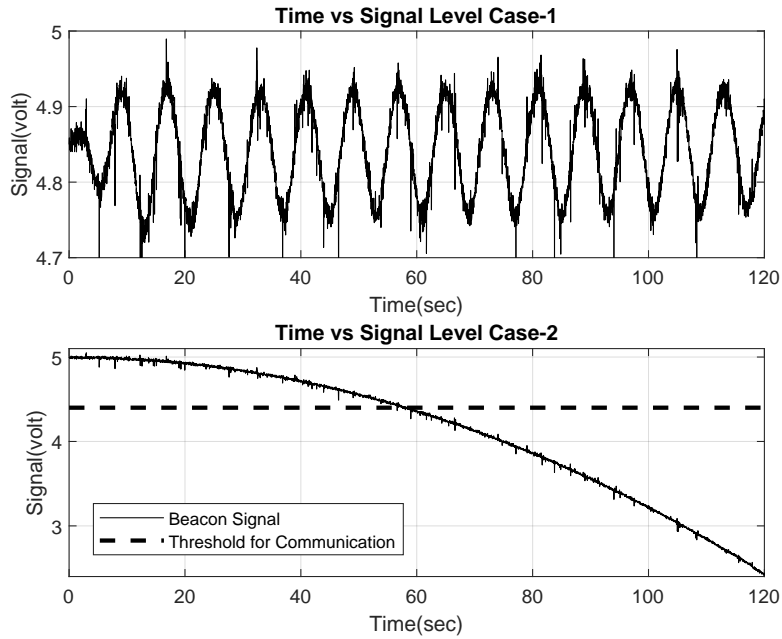


Figure 7.27: PGCS Method Simulation-2, Case-1 and Case-2

Table 7.16: PGCS Method Performance Parameter for Simulation-2

Simulation-2	Signal Level, Mean (volt)	Oscillation Rate (%)	Tracking
Case 1	4.83	1.86%	On
Case 2	Communication lost	-	Off

Simulation-3

Target satellite drift is simulated. The simulation details are given in Table 7.8.

The results of the simulations are presented graphically in Figure 7.28. Also, the parametric performance values are given in Table 7.17. The tracking loop can compensate for the gyro drift with less than 3% oscillation. This results in very small communication performance drop and it is still enough. On the other hand, this is opposite of Case-2. LOS moves continuously in one direction even out of the satellite look area and communication is lost after the threshold level which is defined as 3 dB beamwidth.

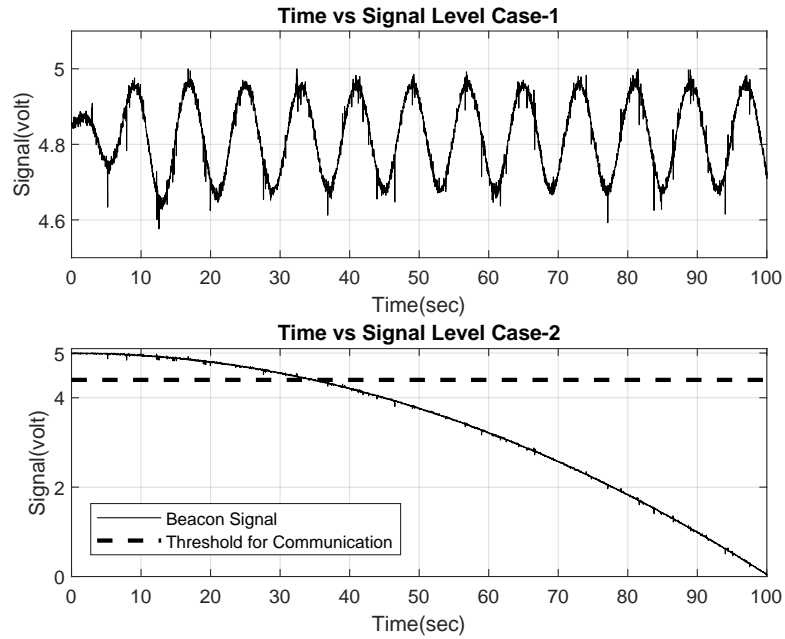


Figure 7.28: PGCS Method Simulation-3, Case-1 and Case-2

Table 7.17: PGCS Method Performance Parameter for Simulation-3

Simulation-3	Signal Level, Mean (volt)	Oscillation Rate (%)	Tracking
Case 1	4.82	2.8%	On
Case 2	Communication lost	-	Off

7.3.3.5 Comparison of Conical Scanning Techniques

Simulations and analyzes are done for three different conical scanning techniques. Firstly, CSAP and CSC methods are compared. The CSAP method performs well for mispointing simulation cases. It can calculate the pointing error at the end of just one scanning period. The compensation is calculated with the measurements at the current scanning time. However, the CSC method reaches the steady-state more than one scanning period. This method gets measurement while moving and this results in a slight compensation error. On the other hand, the opposite of this result is obtained for gyro and target-drift simulations. The CSAP method results in 1.81% and 3.12% oscillation for gyro and target-drift simulations respectively.

The CSC method results in 1.55% and 2.1% oscillation for the same simulations. Hence, the CSC method has less oscillation than the CSAP method. The CSC method can more effectively handle constant drift rates. It uses the previous measurements and this provides an estimation of the next LOS position. However, the CSAP method waits until the scanning period so its position data are convolved with wrong measurement samples. Secondly, the PGCS method is settled in the maximum RSS faster than the CSC method but not as fast as the CSAP method. The PGCS method has 1.86% and 2.8% oscillation for the gyro and target-drift simulations. This shows that it has better performance than the CSAP but not as good as the CSC method. Derivation of the measurement signal gives less reliable samples of the RSS. As a result of the simulations and comparisons, the CSC method has the best performance.

7.3.4 Step Tracking

Step tracking operates by moving the antenna within angle step by step to search for the position, which maximizes the RSS. Perturbation motion waves are expressed in Equation (716).

$$x_{perturbation} = \Delta x \quad (716a)$$

$$y_{perturbation} = \Delta y \quad (716b)$$

LOS position of antenna can be obtained instantaneously with Equation (717).

$$x_{i+1} = x_i + \Delta x \quad (717a)$$

$$y_{i+1} = y_i + \Delta y \quad (717b)$$

Step tracking operation sequences are given in Figure 7.29 with details. The algorithm uses these steps for command generation to rate loop. Simulations are performed to see the effect of the step sizes.

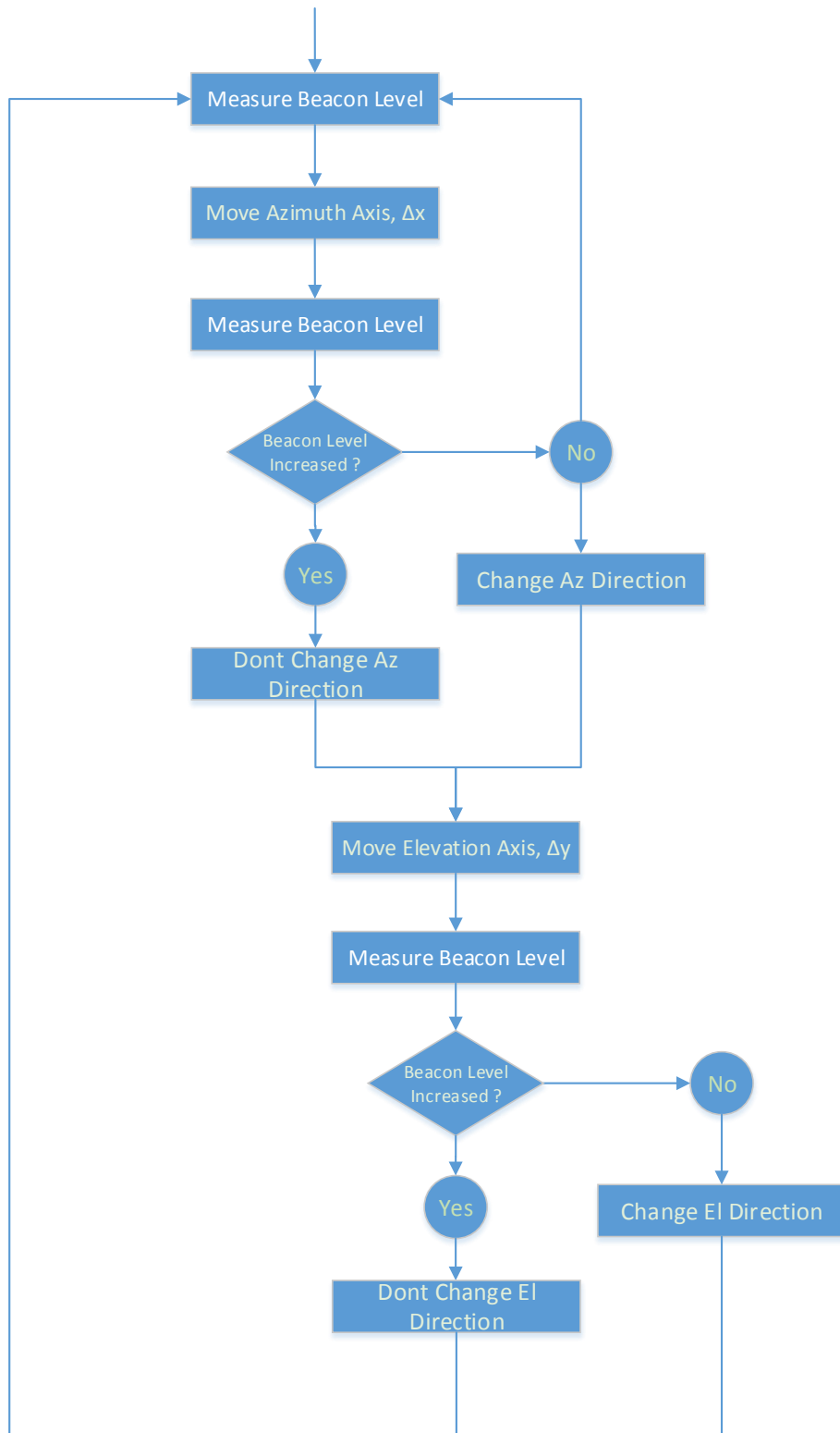


Figure 7.29: Operation Sequence of Step Tracking

Simulation conditions are as follows:

- Azimuth axis offset from the target satellite location, $x_0 = 0.4$ deg
- Elevation axis offset from the target satellite location, $y_0 = 0.6$ deg
- Constant step size tracking is used during the simulations

Table 7.18: Step Size Table

Case no	Δx	Δy
1	0.05	0.05
2	0.07	0.07
3	0.1	0.1
4	0.2	0.2
5	0.3	0.3
6	0.4	0.4

Table 7.19: Performance Parameters of Simulation for Different Step Sizes

Simulation-1	Signal Level (volt)	Settling to Max RSS (sec)	Num. of Steps
Case 1	4.99	4.3	22
Case 2	4.99	3.07	16
Case 3	4.99	2.27	10
Case 4	4.99	0.85	4
Case 5	4.9	0.45	3
Case 6	4.8	0.25	1

The results of these simulations the following can be obtained:

- Max RSS increases with the decrease of step size
- There exists even small oscillation with the increase of step size
- RSS reaches steady-state case quickly with the increase of step size

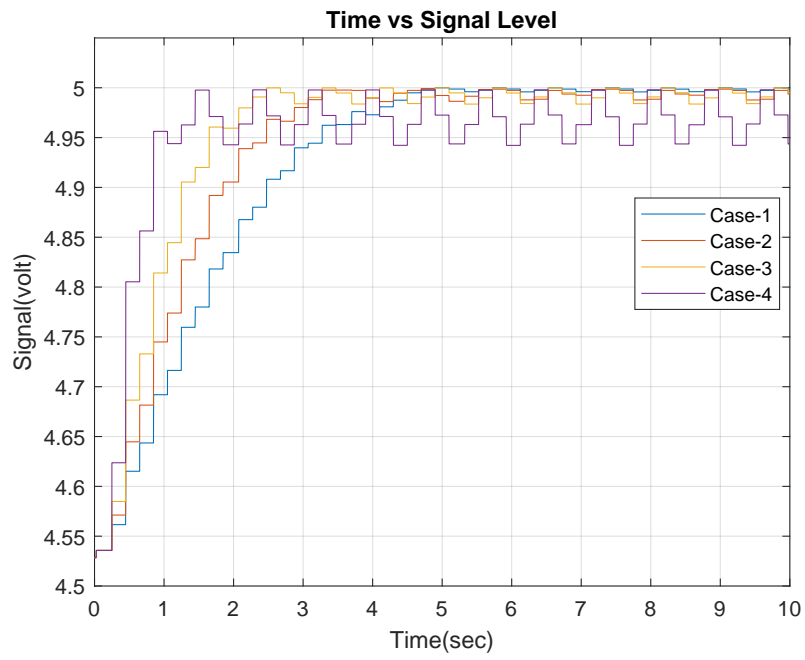


Figure 7.30: Simulation for Different Step Sizes, Case-1,Case-2,Case-3,Case-4

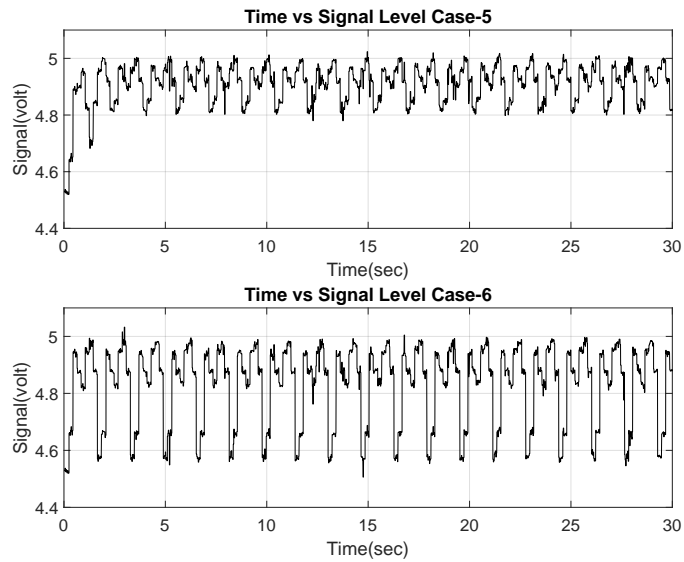


Figure 7.31: Simulation for Different Step Sizes, Case-5 and Case-6

Table 7.20: CSST Method Controller Gains

Controller	Azimuth	Elevation
K_p	5	5

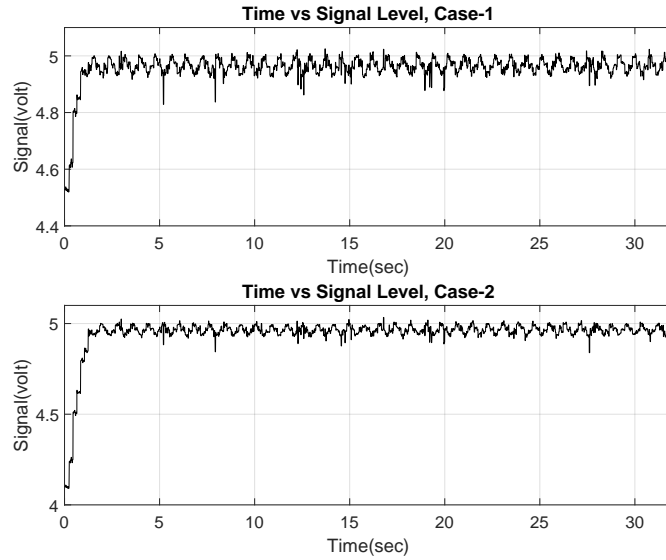


Figure 7.32: CSST Method Simulation-1, Case-1 and Case-2

- RSS oscillation amplitude increases with the increase of step size

Finally, the step size is chosen as $\Delta x = \Delta y = 0.2$ deg and it is used in the following sections.

7.3.4.1 Constant Step Size Tracking (CSST)

Simulation-1

LOS is mispointed deliberately and tracking is performed for different offsets. Simulation details are shown in Table 7.4.

Tracking controller gains are given in Table 7.20. The results of the simulations are presented graphically in Figure 7.32 and Figure 7.33.

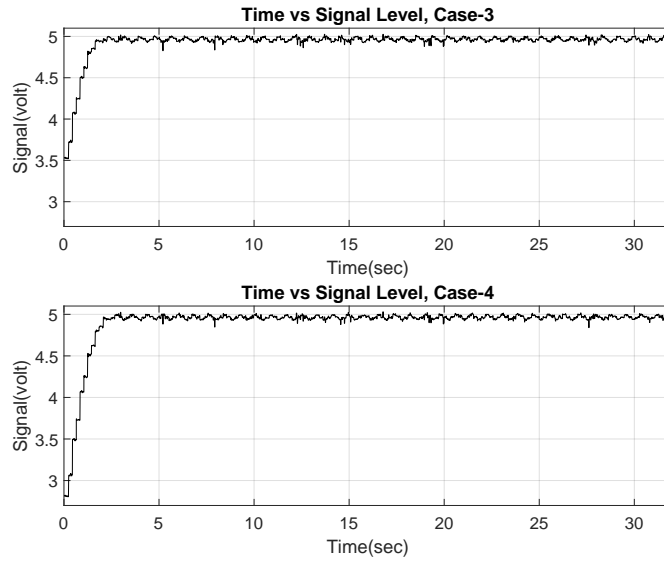


Figure 7.33: CSST Method Simulation-1, Case-3 and Case-4

Table 7.21: CSST Method Performance Parameter for Simulation-1

Simulation-1	Signal Level (volt)	Settling to Max RSS (sec)	Num. of Cycles
Case 1	4.97	0.85	4
Case 2	4.97	1.25	6
Case 3	4.97	1.65	8
Case 4	4.97	2.07	10

Also, the parametric performance values are given in Table 7.5. The number of steps increases with the mispointing angle increase. However, the RSS reaches the steady-state value for all cases.

Simulation-2

Gyro sensors random drift error is simulated. Details of the error are given in Table 7.6

The result of the simulations are presented graphically in Figure 7.34. Also, the parametric performance values are given in Table 7.22. Tracking loop can compensate

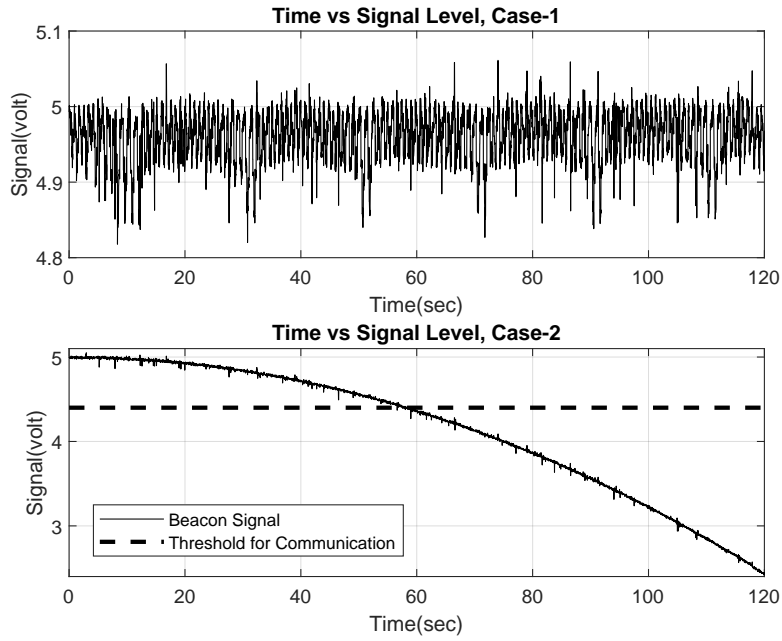


Figure 7.34: CSST Method Simulation-2, Case-1 and Case-2

Table 7.22: CSST Method Performance Parameter for Simulation-2

Simulation-2	Signal Level, Mean (volt)	Oscillation Rate (%)	Tracking
Case 1	4.92	1.52%	On
Case 2	Communication lost	-	Off

the gyro drift with less than 2% oscillation. This results in very small communication performance lost and it will be still enough. On the other hand, this is opposite for the Case-2. LOS moves continuously in one direction even out of the satellite look area and communication is lost after threshold level which is defined as 3 dB beamwidth. Therefore, tracking loop is very effective for the sensor drift error.

Simulation-3

Target drift is simulated. The simulation details are given in Table 7.8.

Result of the simulations are presented graphically in Figure 7.35.

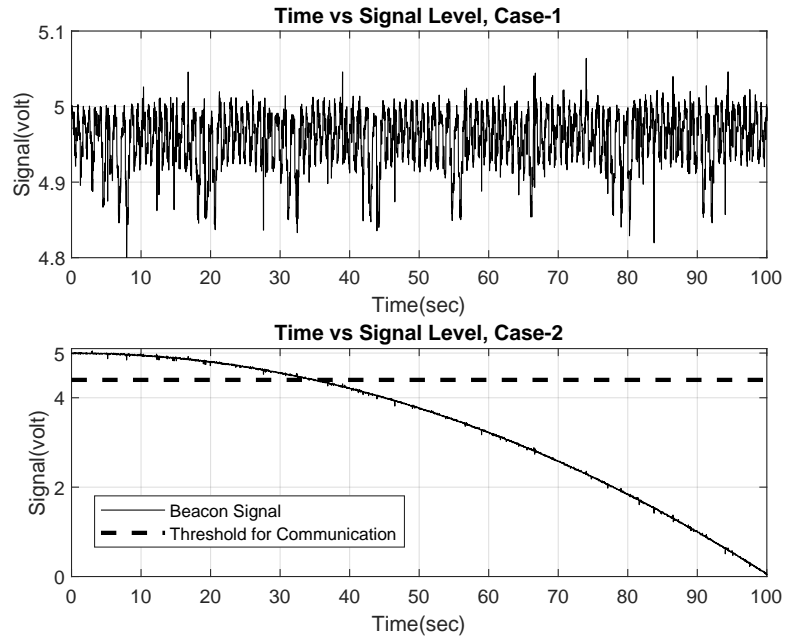


Figure 7.35: CSST Method Simulation-3, Case-1 and Case-2

Table 7.23: CSST Method Performance Parameter for Simulation-3

Simulation-3	Signal Level, Mean (volt)	Oscillation Rate (%)	Tracking
Case 1	4.92	1.52%	On
Case 2	Communication lost	-	Off

Also, the parametric performance values are given in Table 7.23. Tracking loop can compensate the gyro drift with less than 4% oscillation. This results in very small communication performance lost and it will be still enough. On the other hand, this is opposite for the Case-2. LOS moves continuously in one direction even out of satellite look area and communication is lost after threshold level which is defined as 3 dB beamwidth.

7.3.4.2 Variable Step Size Tracking (VSST)

Constant step size tracking algorithms have important problems. Step size effects tracking speed and error compensation as mentioned. Bigger step size enables high tracking speed but lower accuracy. On the other hand, smaller step size results in slow tracking speed but higher accuracy. Actually, there is no optimum step size to satisfy both performance and accuracy. These problems can be overcome by variable step size. Step size is defined in Equation (718).

$$\Delta x = \kappa[\Delta p(t)]^\gamma \quad (718a)$$

$$\Delta y = \kappa[\Delta p(t)]^\gamma \quad (718b)$$

where:

κ : Constant

$\Delta p(t)$: Deviation from maximum power

γ : Constant

Two different comparison simulations are performed to see the effect of variable step size parameters. Firstly, the κ values are changed for the same γ . Details of the parameters are given in Table 7.24. Simulation result is given in Figure 7.36. Secondly, the γ values are changed for the same κ . Details of the parameters are given in Table 7.25. Simulation result is given in Figure 7.37.

Table 7.24: Step Tracking Parameter Table for Different κ

Case no	κ	γ
1	0.2	0.4
2	0.5	
3	0.7	
4	0.9	

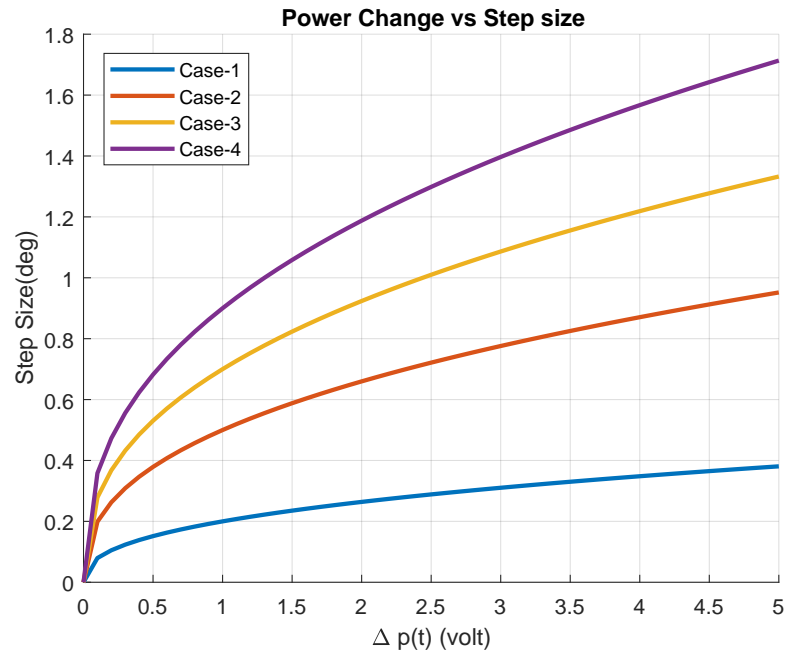


Figure 7.36: Power Change for Same γ and Different κ

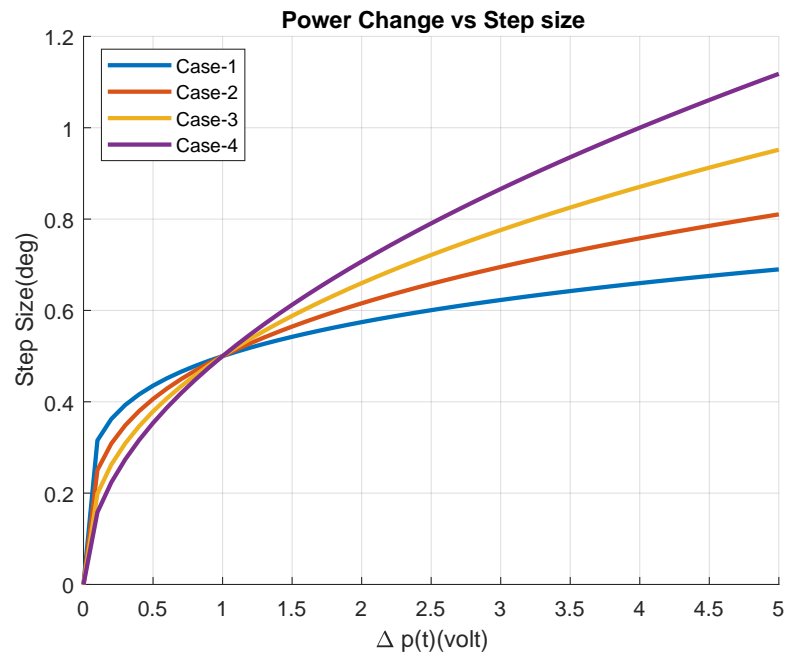


Figure 7.37: Power Change for Same κ and Different γ

Table 7.25: Step Tracking Parameter Table for Different γ

Case no	γ	κ
1	0.2	0.5
2	0.3	
3	0.4	
4	0.5	

Table 7.26: VSST Method Controller Gains

Controller	Azimuth	Elevation
K_p	3.5	3.5

The following results are obtain from the parameter simulations:

- The γ affects the size of the step and adjustment range
- The κ affects the speed of reaching max signal level

Finally, $\kappa = 0.5$ and $\gamma = 0.4$ is chosen and these are used in the following simulations.

Simulation-1

LOS is mispointed deliberately and step tracking compensation is performed for different offsets. The simulation details are shown in Table 7.4. Tracking controller gains are given in Table 7.26.

The results of the simulations are presented graphically both in Figure 7.38 and Figure 7.39. Also, the parametric performance values are given in Table 7.27.

The number of steps increases with the mispointing angle increase. However, the RSS reaches the steady-state value for all cases.

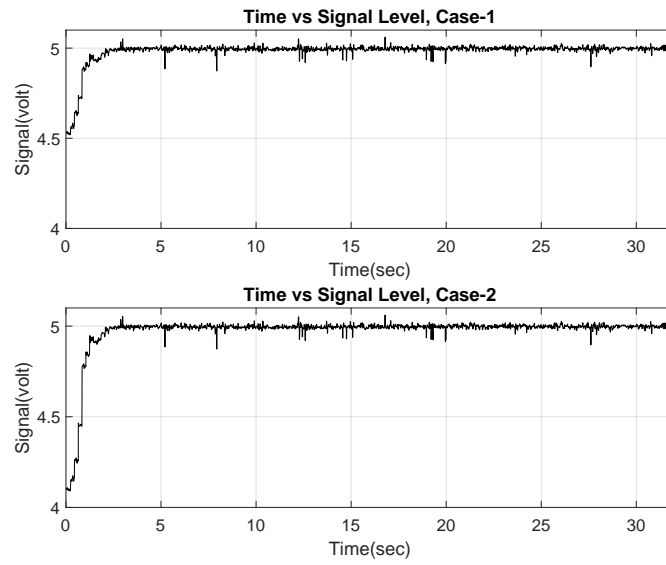


Figure 7.38: VSST Method Simulation-1, Case-1 and Case-2

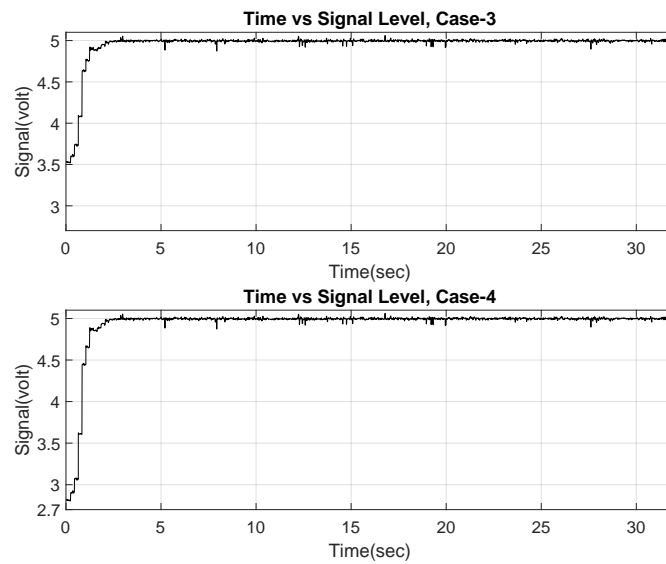


Figure 7.39: VSST Method Simulation-1, Case-3 and Case-4

Table 7.27: VSST Method Performance Parameter for Simulation-1

Simulation 1	Signal Level (volt)	Settling to Max RSS (sec)	Num. of Cycles
Case 1	4.97	2.07	16
Case 2	4.97	2.1	17
Case 3	4.97	2.07	16
Case 4	4.97	2.2	19

Simulation-2

Gyro sensor random drift error is simulated. Details of the error are given in Table 7.6.

The results of the simulations can be found in Figure 7.40. Simulations show that

Table 7.28: VSST Method Performance Parameter for Simulation-2

Simulation 2	Signal Level, Mean (volt)	Oscillation Rate (%)	Tracking
Case 1	4.99	0.01%	On
Case 2	Communication lost	-	Off

the tracking loop can compensate for the gyro drift and maximize the RSS. On the other hand, there exists small oscillation even tracking. However, this RSS is still good enough for good communication performance. On the other hand, this is the opposite of Case-2. LOS moves continuously in one direction even out of the satellite look area and communication is lost after the threshold level which is defined as 3 dB beamwidth.

Simulation-3

Target drift is simulated. The simulation details are given in Figure 7.41.

The results of the simulations are presented graphically in Table 7.29. Simulations show that the tracking loop compensates the target drift and maximize the RSS. On the other hand, this is the opposite of Case-2. LOS moves continuously in one direction even out of the satellite look area and communication is lost after the threshold.

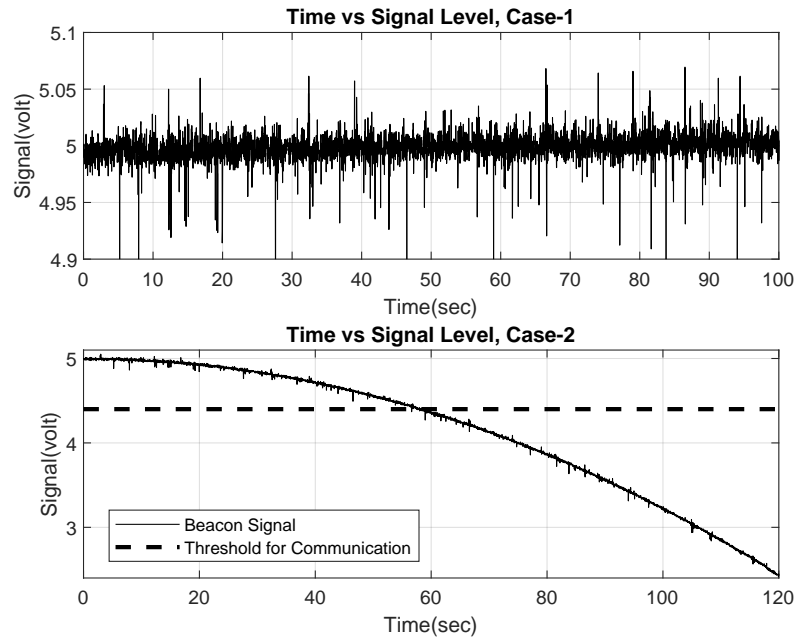


Figure 7.40: VSST Method Simulation-2, Case-1 and Case-2

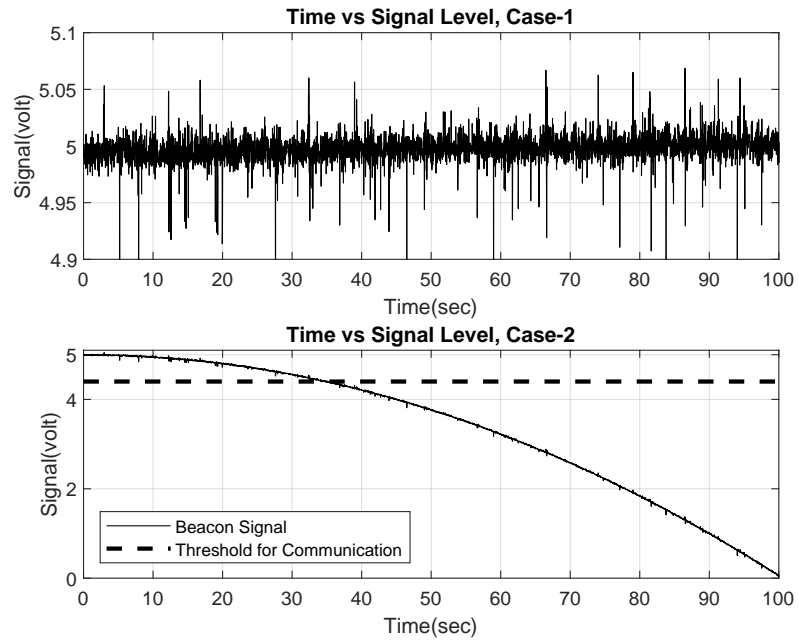


Figure 7.41: VSST Method Simulation-3, Case-1 and Case-2

Table 7.29: VSST Method Simulation-3, Case-1 and Case-2

Simulation-3	Signal Level, Mean (volt)	Oscillation Rate (%)	Tracking
Case 1	4.99	0.02%	On
Case 2	Communication lost	-	Off

7.3.4.3 Comparison of Step Tracking Techniques

Simulations and analyzes are done for two different step tracking techniques. Although the VSST method has a higher convergence slope than the CSST, it cannot reach steady-state at that speed. Therefore, the CSST method needs less step size and time than the VSST method. On the other hand, the VSST method can provide 0.01% and 0.02% oscillation for gyro and target-drift simulations. The CSST method can provide 1.52% for both simulations. The VSST methods can compensate drift error with high performance with the help of variable step size. As a result, the VSST method is better than the CSST method for two of the three simulation cases.

CHAPTER 8

SUMMARY, CONCLUSIONS AND FUTURE WORK

8.1 Summary and Conclusions

In this thesis, excessive increase for high bandwidth downlink and the growth of the satellite communication market is stated. SATCOM on-the-move antenna communication performance improvements are targetted. It is shown that LOS pointing accuracy is directly effected the communication performance of a high-bandwidth directional antenna system. Different reasons for poor pointing accuracy are explained. Some of them are related to control performance, some of them are due to electronic and mechanical parts.

A novel controller system is developed, designed and simulated to overcome these issues. This controller structure is mainly composed of LOS inertial stabilization and also open and closed-loop pointing techniques. It is stated that each of them has an important role in satellite communication and the pointing accuracy of the LOS. However, it is shown that closed-loop pointing works like a compensator to cover all the mispointing errors. And the performance of a SATCOM on-the-move antenna system critically depends on the closed-pointing methods.

System identification tests are performed to obtain the analytical model of the antenna gimbal system. It is experienced that the elevation axis position changes the characteristics of azimuth-axis. Therefore, azimuth-axis tests are done for different elevation-axis positions. In addition to that, the inertia change of the azimuth axis is also modeled using 3D-CAD software. The amount of work is dedicated for the sake of obtaining a realistic model to make a correlation with the field tests and easy implementation of this workout to the real system. The estimated model is validated

by field tests. The estimations cover all the important modes with a minimum order and are accurate enough to represent system dynamics. Moreover, the kinematic coupling effect is also included in the gimbal system model as a disturbance.

The feedback controller is designed to attenuate ship motions and perform tracking controller commands with a high response rate. Principles of control theory are given and the design aim is to have robust performance and tracking error which asymptotically decays towards zero are verified by simulations. In addition to that, disturbance rejection performance is confirmed by disturbance simulation.

After the analytical model is developed and the LOS controller is designed, two-stage pointing modes are presented. Open-loop pointing vector calculation steps are given in a detailed manner to direct the antenna LOS from a known GPS location to the target satellite location.

Closed-loop pointing or tracker controller structure is given schematically. Tracking algorithms or estimators are specified mainly as conical scanning and step tracking. Three different conical scanning and two-step tracking methods are constructed, implemented and analyzed. Implementation details and tracker parameter selection simulations are presented. Three critical real case problems are chosen and simulation scenarios related to these are created. Every method is simulated respectively. Behavior and performance results of the tracking methods are given both graphically and analytically with details. The results of the simulations are showed that the tracking algorithm plays a very crucial role. It is also observed that this algorithm protects communication link from failure and increases the signal strength. It is also shown that in the case of gyro or target-drift errors communication link cannot be established for a long period and lost. LOS stabilization is not enough for high-bandwidth uninterrupted communication.

Conical scanning (CSC) method has the best performance characteristics than other conical scanning techniques. It helps the communication link to continue with less than maximum 3% oscillation for drift simulations. Also, the communication performance in the case of mispointing is increased as quickly as possible.

The variable step size tracking method has the best performance characteristics than other step tracking techniques. It helps the communication link to continue with less than maximum 0.03% oscillation for drift simulations. Also, the communication performance in the case of mispointing is increased as quickly as possible.

Conical scanning and step tracking algorithms performances can be compared as follow. Step tracking reaches steady-state RSS more quickly than conical tracking in mispointing simulations. Conical scanning needs scanning time but step tracking does not. It is seen that conical scanning makes a continuous motion but step tracking makes a discrete one. Precise step size motion cannot be possible due to friction and overshoot. Therefore, correct measurement is hard with the step tracking method. Step tracking uses only two measurements at each time and it gives a less reliable compensation step. However, conical scanning samples all the data during the scanning period and it is less affected by incorrect measurement, noise or incorrect LOS positioning than step tracking. The discrete motion of the step tracking results in wear on mechanical driver components due to small step size, friction and overshoot. Hence, step tracking shortens the lifetime of the gimbal system. Therefore, it can be obtained that conical scanning is more robust, reliable and less harmful than step tracking.

8.2 Future Work

One important future work is to develop smart and prediction based algorithms. All the closed-loop methods rely on previous data. Therefore, it is less reliable for highly noisy random signals and an instant interrupt in signal cases.

Another future work is the implementation and simulations of other tracking methods that are given in the literature works.

A more generic antenna gimbal system analytical modeling method can be developed to model for different applications and implement tracking algorithms before working on the real systems.

REFERENCES

- [1] J. Debruin, “Control systems for mobile satcom antennas,” *IEEE Control Systems Magazine*, vol. 28, no. 1, pp. 86–101, 2008.
- [2] Y. Jinbo, Z. Fengang, C. Fu, and Z. Hao, “Technical of satellite communication on-the-move (sotm),” *DEStech Transactions on Computer Science and Engineering*, no. aiea, 2017.
- [3] Q. Luo and S. Gao, “Smart antennas for satellite communications on the move,” in *2017 International Workshop on Antenna Technology: Small Antennas, Innovative Structures, and Applications (iWAT)*, pp. 260–263, IEEE, 2017.
- [4] J. Hilker, “Inertially stabilized platform technology concepts and principles,” *IEEE control systems magazine*, vol. 28, no. 1, pp. 26–46, 2008.
- [5] W. Gawronski and E. M. Craparo, “Antenna scanning techniques for estimation of spacecraft position,” *IEEE Antennas and Propagation Magazine*, vol. 44, no. 6, pp. 38–45, 2002.
- [6] *Inclined Orbit Operation of Geostationary Satellites*, [accessed October 10, 2019]. <http://www.satsig.net/satellite/inclined-orbit-operation.htm>.
- [7] M. K. Masten, “Inertially stabilized platforms for optical imaging systems,” *IEEE Control Systems Magazine*, vol. 28, no. 1, pp. 47–64, 2008.
- [8] B. Ekstrand, “Equations of motion for a two-axes gimbal system,” *IEEE Transactions on Aerospace and Electronic Systems*, vol. 37, no. 3, pp. 1083–1091, 2001.
- [9] A. T. Andersen, M. H. Sørensen, R. Izadi-Zamanabadi, and R. Wisniewski, “Stabilizing a f77 antenna system for maritime use: An internal model approach,” Master’s thesis, Aalborg University, 2005.

- [10] E. A. Marsh, *Inertially stabilized platforms for SATCOM on-the-move applications: A hybrid open/closed-loop antenna pointing strategy*. PhD thesis, Massachusetts Institute of Technology, 2008.
- [11] J. Ohlson and M. Reid, “Conical-scan tracking with the 64-m-diameter antenna at goldstone,” 1976.
- [12] J. Ohlson and K. Abichandani, “Conscan implementation for antenna control assembly,” 1982.
- [13] D. Eldred, “An improved conscan algorithm based on a kalman filter,” 1994.
- [14] G. M. Brooker, “Conical-scan antennas for w-band radar systems,” in *2003 Proceedings of the International Conference on Radar (IEEE Cat. No. 03EX695)*, pp. 406–411, IEEE, 2003.
- [15] R. F. Karol, “Peak-seeking controller for real-time mobile satellite tracking,” Master’s thesis, California Institute of Technology, 2012.
- [16] A. L. Souza, G. A. Borges, J. Y. Ishihara, H. C. Ferreira, R. A. Borges, A. M. Kulabukhov, V. A. Larin, and V. V. Belikov, “Antenna pointing error estimation using conical scan technique and kalman filter,” in *IEEE International Conference on Control and Automation*, 2013.
- [17] M. Richaria, “An improved step-track algorithm for tracking geosynchronous satellites,” *International journal of satellite communications*, vol. 4, no. 3, pp. 147–156, 1986.
- [18] J. I. Laine, “2d model-based step-track procedure,” *IEEE Transactions on Aerospace and Electronic Systems*, vol. 36, no. 4, pp. 1386–1391, 2000.
- [19] A. Pirhadi, M. Hosseini, and M. Hakak, “A novel implementation of geo satellite step track subsystem,” 2005.
- [20] K. Han, W. Guo, and X. Gao, “A step tracking on the sotm,” in *2010 3rd International Conference on Computer Science and Information Technology*, vol. 5, pp. 214–216, IEEE, 2010.
- [21] W. Jia, L. Hao, and K. Du, “Step tracking algorithm based on finite difference stochastic approximation for satcom on-the-move,” in *2011 International*

- Conference on Electric Information and Control Engineering*, pp. 2632–2635, IEEE, 2011.
- [22] C. Chen and Y. Wang, “Research of the variable step size algorithm of antenna tracking satellite for satcom on-the-move,” in *2013 5th International Conference on Intelligent Human-Machine Systems and Cybernetics*, vol. 2, pp. 490–493, IEEE, 2013.
- [23] K. Abichandani and J. Ohison, “Boresighting techniques for the antenna control assembly (aca),” *Irhe Telecommunications and Data Acquisition IProgress Report 42-64*, vol. 3, p. 116, 1981.
- [24] G. Hawkins, D. Edwards, and J. McGeehan, “Tracking systems for satellite communications,” in *IEE Proceedings F (Communications, Radar and Signal Processing)*, vol. 135, pp. 393–407, IET, 1988.
- [25] S. N. V. Mercy Soumya and A. N. Reddy, “Design considerations of radomes: A review,” *International Journal of Mechanical Engineering and Technology (IJMET)*, vol. 8, no. 3, pp. 42–48, 2017.
- [26] *Proper Radome Sizing*, [accessed September 1, 2019]. <https://compositeradomes.com/radomes/proper-radome-sizing>.
- [27] A. K. Maini and V. Agrawal, *Satellite technology: principles and applications*. John Wiley & Sons, 2011.
- [28] K. Williams, T. Honeyands, R. Holmes, R. Orense, A. Roberts, M. Pender, D. McCallum, and T. Krull, “Maritime bulk cargo transportable moisture limit requirements for iron ore shipments,” 2015.
- [29] W. Gawronski, *Advanced structural dynamics and active control of structures*. Springer Science & Business Media, 2004.
- [30] J. T. Gravdahl, “Friction problems in servomechanisms: Modeling and compensation techniques,” 1998.
- [31] D. Mutlu, “Platform motion disturbances decoupling by means of inertial sensors for a motion stabilized gimbal,” Master’s thesis, Middle East Technical University, 2015.

- [32] B.-T. Wang, “Determination of mode shapes from the operational deflection shape,” in *The 8th International Congress on Sound and Vibration*, pp. 1941–1948, 2001.
- [33] M. Richardson and B. Schwarz, “Modal parameter estimation from operating data,” *Sound and vibration*, vol. 37, no. 1, pp. 28–39, 2003.
- [34] W. A. Fladung, A. W. Phillips, and R. J. Allemang, “Application of a generalized residual model to frequency domain modal parameter estimation,” *Journal of sound and vibration*, vol. 262, no. 3, pp. 677–705, 2003.
- [35] W. Gawronski, *Modeling and control of antennas and telescopes*. Springer Science & Business Media, 2008.
- [36] G. Ellis and R. D. Lorenz, “Resonant load control methods for industrial servo drives,” in *Conference Record of the 2000 IEEE Industry Applications Conference. Thirty-Fifth IAS Annual Meeting and World Conference on Industrial Applications of Electrical Energy (Cat. No. 00CH37129)*, vol. 3, pp. 1438–1445, IEEE, 2000.
- [37] S. H. Stovall, “Basic inertial navigation,” *Naval Air Warfare Center Weapons Division*, 1997.
- [38] G. M. Brooker, “Conical-scan antennas for w-band radar systems,” in *2003 Proceedings of the International Conference on Radar (IEEE Cat. No. 03EX695)*, pp. 406–411, IEEE, 2003.
- [39] *Electronic Countermeasure*, [accessed October 10, 2019]. <https://basicsaboutaerodynamicsandavionics.wordpress.com/2016/03/29/electronic-countermeasure-ecm/>.